Synthesis and Characterisation of ZnS and CdS Nanostructures

A THESIS

Submitted to the

FACULTY OF SCIENCE

THAPAR UNIVERSITY, PATIALA

for the degree of

Doctor of Philosophy

2010

ZINKI JINDAL

SCHOOL OF PHYSICS AND MATERIALS SCIENCE

THAPAR UNIVERSITY

PATIALA-147 004

INDIA

dedicated to my beloved parents

Acknowledgements

I would like to express my sincere appreciation to my supervisor, **Prof. N. K. Verma**, for being the pillar of support and encouragement throughout my research work. His experience, strength, tenderness and willfulness, has taught me the lessons of life, which are of immense help to me to take decisions in my every endeavor.

I gratefully acknowledge the financial support of Defence Research and Development Organization **(DRDO)**, University Grants Commision **(UGC)** and Council of Scinetific and Industrial Research **(CSIR)**, Government of India, throughout my work.

I am thankful to my PhD committee members, **Dr. Susheel Mittal**, Dean, Research and Sponsored Projects and **Dr. Kulvir Singh**, Assistant Professor, School of Physics and Materials Science (SPMS), for their constructive comments and regularly ensuring the progress of my research work.

I am profoundly obliged to **Dr. O. P. Pandey**, Professor and Head, SPMS, for his whole-hearted support and motivation helping successful completion of this research work. I am thankful to all the **faculty** and **staff** members of SPMS for their support.

I am thankful to my senior labmates, **Dr. Sunil Kumar**, **Dr. (Mrs.) Raminder Kaur** and **Mr. Karamjit Singh** for their help and support throughout my research work, especially in the early days when even the words 'Research/PhD' were

new to me. Also, I wish to render lots of thanks and good wishes to my juniors **Mr. Sanjeev Kumar**, **Mr. Sunil Thakur**, **Ms. Manveen Kaur, Ms. Vaishali, Ms. Anuja** and **Mrs. Shweta Kakkar**, for coming to my assistance even at odd hours. I also acknowledge the co-operation and encouragement extended to me by my fellow Research scholars at Thapar University, especially **Ms. Meenakshi Malik, Ms. Shashi Bhanwar, Mrs. Shefali Kanwar**, **Ms. Kamalpreet Kaur, Dr. (Mrs.) Anu Arora**, **Ms. Jasmeet Kaur**, **Ms. Neeraj Sharma**, **Mr. Vishal Chaudhary** and **Mr. Ravi Shukla**.

I am highly grateful to **Prof. M. L. Singla**, Head, Materials Science Division and Biotechnology Division, Council of Scienctific and Industrial Organization (CSIO), Chandigarh, for making available the characterization facility.

Uncountable words of thanks, love, and regards for **Dr.(Mrs.)Rama Verma**, who supported me just like my mother.

I thank **Dr. Apurba Dev** of University of Bremen, Germany, for his support in every moment of difficulty, as well as his constructive comments.

I offer my deepest gratitude to my parents, **Smt. Neelam Jindal** and **Sh. M. G. Jindal**, my sister, **Ms. Rimmi**, and my brother, **Mr. Karanveer Jindal**, for their love, encouragement and motivation, and for their confidence in me.

I am thankful to my grandfather **Late Shri Om Prakash Jindal**, for his un

failing love and blessings, without whose dreams, I won't have started this work.

The chain of gratitude would be definitely incomplete without thanking my **Guruji** and the **Almighty**, the prime movers, for inspiring and guiding me (the humble being) to complete this task successfully.

Patiala

April, 2010

Jindal 6/4/2010

(Zinki Jindal)

THAPAR UNIVERSITY

CERTIFICATE

Certified that the thesis **"Synthesis and Characterisation of ZnS and CdS Nanostructures"**, which is being submitted by Ms. Zinki Jindal, in fulfillment of the requirements for the award of the degree of Doctor of Philosophy in the SCHOOL OF PHYSICS & MATERIALS SCIENCE, Thapar University, Patiala, is an authentic record of the candidate's own independent and original research work carried out by her, under my supervision and guidance. The matter embodied in this thesis has not been submitted in part or full to any other University or Institute for the award of any degree.

Date 6/4/10

(Supervisor)

Prof. N. K. Verma

School of Physics & Materials Science

Thapar University, Patiala – 147 004

(PUNJAB) INDIA

List of Publications

I. International Journals:

1. 'Electrochemical template-assisted fabrication of CdS micro/nanostructures', **Zinki Jindal** and N. K. Verma, Physica E, 41(10), October 2009, 1752-1756.

2. 'Morphologically controlled CdS microstructures using dc electrochemical template synthesis', **Zinki Jindal** and N. K. Verma, Journal of Optoelectronics and Advanced Materials, 10(12), December 2008, 3283-3287.

3. 'Photoluminescent properties of ZnS:Mn nanoparticles with in-built surfactant', **Zinki Jindal** and N. K. Verma, J of Materials Science(Springer), 43(19), October 2008, 6539-6545.

4. 'Effect of UV radiation on photoluminescent properties Cu-doped Zn nanoparticles', Zinki Jindal and N. K. Verma, Optoelectronics and Advanced Materials - Rapid Communications, 2(3), March 2008, 166-169

II. In Proceedings of National and International Conferences:

1. 'Europium doped CdS nanorods', N. K. Verma and **Zinki Jindal**, Proceedings of the International Conference on 1st NanoToday Conference, held at

Biopolis, Singapore on August 3-5, 2009, P2-19.

2. 'CdxMn1-xS nanorods: synthesis and characterization', **Zinki Jindal** and N. K. Verma, Proceedings of the National Seminar on Ferroelectrics and Dielectrics -15, held at Thapar University, Patiala, on November 6-8, 2008, p106.

3. 'CdS microwires/tubules in polycarbonate membranes using electrochemical template synthesis', **Zinki Jindal** and N. K. Verma, Proceedings of the 11th Punjab Science Congress, held at Thapar University, Patiala, on February 7-9, 2008, p151.

4. 'Optical properties of UV illuminated ZnS:Cu nanoparticles', **Zinki Jindal** and N. K. Verma, Proceedings of the Indo-Australian Symposium on Multifunctional Nanomaterials, Nanostructures and Applications (MNNA 2007) held at University of Delhi, Delhi, December 19 -21, 2007.

5. 'Synthesis and photoluminescence of ZnS:Mn nanoparticles', **Zinki Jindal** and N. K. Verma, Proceedings of the National Conference on Emerging Trends in Engineering Materials, held at Thapar Institute of Engineering and Technology, Patiala, February 1-3, 2007.

6. 'Luminescence of Mn doped ZnS nanoparticles', **Zinki Jindal**, Karamjit Singh and N. K. Verma, Proceedings of the National Conference on Multifunctional Nanomaterials, Nanostructures and Applications, held at University of Delhi, 22-23 December 2006.

7. 'Electrochemical template synthesis of CdS microwires and their morphological characterization', **Zinki Jindal** and N. K. Verma, Proceedings of the Inter-

national Conference on Lasers and Nanomaterials , held at Saha Institute of Nuclear Physics, Kolkata, on November 30- December 2, 2006, pPN-77.

8. 'Fabrication of electrochemical template synthesis cell for II-VI Chalcogenide semiconductors nanostructures', **Zinki Jindal**, Karamjit Singh and N. K. Verma, Proceedings of the National Conference on Recent Advances in Materials Science, held at Kurukshetra University, Kurukshetra on September 27-29, 2006, p29-33.

III. Papers in pipeline:

1. 'Two-step solvothermal synthesis of CdS/ZnS nanoslabs', **Zinki Jindal** and N. K. Verma

2. 'Effect of heat treatment and Tb doping on CdS nanorods', **Zinki Jindal**, Anuja Saxena and N K Verma

3. 'Structural and optical changes in CdS nanorods with Eu^{3+} doping', **Zinki Jindal**, Sunil Thakur and N. K. Verma

4. 'Effect of heat treatment on ZnS:Eu nanoparticles: synthesis and characterization', **Zinki Jindal**, Vaishali Singhi and N. K. Verma

5. 'Synthesis and characterization of CdS/SiO_2 core/shell nanoparticles doped with silver', **Manveen Kaur**, Zinki Jindal and N. K. Verma

6. 'Enhanced luminescence of UV irradiated Zn(1-x)NixS nanoparticles', **Zinki Jindal** and N. K. Verma

Contents

List of Figures

List of Tables

Abstract

ZnS and CdS materials are known for their wide applications as luminescent materials. Control of dimensions resulting in different nanoforms, like: particles, rods, wires, etc. are of great interest with regard to specific applications of such materials in next generation electronic and photonic devices with low power consumption.These II-VI compound semiconductors have been studied for a variety of applications such as optical coatings, photoconductors, optic modulators, electro-optic modulators, flat panel displays, electroluminescent devices, sensors, and lasers. These have also been applied in photocatalyst, infrared windows, pigments and non-linear optical devices.

Syntheses of ZnS and CdS nanostructures (particles, rods, wires, tubules, flowers, cactus-like structures, tetrapods, etc.) through electrochemical template synthesis, solvothermal route and chemical precipitation technique have been presented in this work. The structural, morphological, compositional and optical properties of the synthesized nanoforms have been investigated. The techniques used for the characterization of the samples, include: X-ray diffraction (XRD), Scanning Electron Microscopy (SEM), Transmission Electron Microscopy (TEM), Electron Diffraction X-ray Analysis (EDAX), Fourier Transform Infrared Spectroscopy (FTIR), UV-Visible

Absorption Spectroscopy, Time-Resolved and Energy-Resolved Photoluminescence (PL) measurements.

Transition metal atoms, like: Mn, Cu, Co, Ni, and rare earth materials, like: Tb and Eu have been doped in ZnS nanoparticles. Mn, Eu and Tb metal ions have been doped into CdS nanoforms. The effect of these dopants on the structure, morphology and optical behavior has been studied in the present work. Moreover, ZnS:Cu and ZnS:Ni nanoparticles have been irradiated by prolonged UV radiation. And ZnS:Co, ZnS:Eu and CdS:Tb nanoforms have been annealed in nitrogen gas atmosphere, and the effects have been studied.

In short, this work presents detailed study of ZnS and CdS nanoforms - doped and undoped - synthesized through different bottom-up techniques, as well as their properties. This study is likely to be of use in the field of optoelectronics, biological sensors, etc.

Chapter 1

Introduction

Thinking of nanotechnology to be a new scientific domain, shall not be over shadowed by the fact that, the study on nanometer scale can be traced back to centuries. This is the age of nano-mania, where anything tagged as nano, is considered to be exciting and worthwhile, and has captured the imagination of people worldwide. Much of excitement in this area of research has arisen from recognition of the fact that new phenomena and unprecedented integration density are possible with nanometer scale (1-100 nm) structures. Correspondingly, these ideas have driven scientists to develop methods for making nanostructures.

1.1 Nanotechnology and Nanomaterials

Nanotechnology is design, fabrication and application of nanostructures or nanomaterials, and the fundamental understanding of the relationships between physical properties or phenomena and material dimensions [1]. In order to explore novel phys-

ical properties and phenomena and realize potential applications of nanostructures and nanomaterials, the ability to fabricate and process nanomaterials and nanostructures is the first corner stone in nanotechnology. Synthesis of nanomaterials can be carried out through top-down approach as well as through bottom-up approach. Top-down approach involves reductionism. It often uses the traditional workshop or micro fabrication methods where externally-controlled tools are used to cut, mill and shape materials into the desired shape and order, for example, lithography and ball milling. These techniques are costly, complex, and have limitations to the nanoscale that can be achieved. However, bottom-up approach utilizes the concepts of molecular self-assembly and/or molecular recognition. Such bottom-up approaches are able to produce devices in parallel and much cheaper than top-down methods, with low cost, simple apparatus, high yield and efficient reproducibity. Nanoparticles having size $\sim$ 2 nm can also be synthesized using bottom-up approach. The techniques involved, include: chemical precipitation, sol-gel, solvo/hydrothermal, chemical vapor deposition, template synthesis, etc.

Research works in last two decades have explored some outstanding results and properties of nanomaterials. Obviously, nanomaterials cover a huge area of today's science for its wide-spread applicability in almost all areas. It would require a lengthy space and scope to discuss the features of nanomaterials in terms of their applicability and scope to design future world. However, some interesting properties may be pointed out to evoke curiosity and enthusiasm among the readers about this new era of science. For example, nanomaterials are larger than individual atoms and molecules, but are smaller than bulk solid; hence they obey neither absolute

quantum chemistry nor laws of classical physics, and have properties that are different from those expected. Physics is different on nanometer scale [2]. Properties not seen on a macroscopic scale are now becoming important on nanoscale, such as - quantum mechanics, optics, magnetism, surface reactivity and thermodynamics.

Nanostructures can be characterized, on the basis of the number of dimensions confined to the nanoscale (1-100 nm) [3], as follows:

1. 2-D nanostructures are confined in one direction, e.g., interfaces, membranes, thin films, Multi-layers, etc.

2. 1-D nanostructures are confined in two spatial directions, e.g., nanowires, nanotubes, DNA, etc.

3. 0-D nanostructures are confined in all three spatial directions, e.g., nanoparticles, quantum dots, etc.

Among various nanomaterials, semiconducting sulphide materials such as ZnS and CdS have drawn significant attention for their superior optical and electrical properties, which find promising applications in various photonic and electronic industries. For example, these two materials are well known to have two crystalline structures, cubic (zinc blende) and hexagonal (wurtzite). At room temperature, CdS has highly stable hexagonal phase, and ZnS has cubic phase. Due to the difference in the crystalline structures, the effective masses of electron and hole in their electronic bands change considerably. Therefore, the crystalline structures of these materials play a dominant role in determining their photochemical, photocatalytic,

and photophysical properties.

1.2 Scope of the Thesis

The present thesis deals with the syntheses and characterization of ZnS and CdS nanostructures, using bottom-up approach. The research on nanotechnology and nanomaterials is evolving and expanding very rapidly. There are a number of bottom-up techniques being used for the synthesis of the nanomaterials. However, in this work, we have used three techniques: chemical precipitation, electrochemical template synthesis and solvothermal techniques, to synthesize ZnS and CdS nanostructures including particles, wires, rods, tubules, and various other morphologies like, cauliflower, flower, cactus, etc.

But before starting with the synthesis of the nanostructures, the detailed insight of the properties of the materials should be known. Therefore, in *Chapter 2*, we have presented an overview of the properties of ZnS and CdS materials.

Apart from synthesis, characterization of the materials is equally important. In this work, the synthesized nanomaterials have been characterized through X-ray diffraction (XRD) studies, Scanning electron microscopy (SEM), Transmission electron microscopy (TEM), Energy dispersive analysis of X-rays (EDAX), Fourier transform infra-red spectroscopy (FTIR), UV-visible absorption spectroscopy, Room temperature photoluminescence (PL) and Time-resolved photolumi-

nescence (TRPL) studies. The basic principle, working and data analysis methods have been explained briefly in *Chapter 3*.

Chapter 4 deals with the synthesis and characterization of undoped and doped ZnS nanoparticles using the chemical precipitation technique at room temperature, using aqueous media. The effect of doping, using transition and rare earth metal impurities (Mn, Co, Cu, Ni, Eu and Tb), has been studied. Additionally, this chapter includes the effect of annealing and prolonged UV-irradiation on the nanoparticles.

In the area involving the controlled synthesis of nanostructures using templates, the various methods, include: electrochemical deposition, electroless deposition, chemical polymerization, sol-gel deposition, and chemical vapour deposition. In *Chapter 5*, the synthesis of CdS nanoforms using electrochemical template synthesis has been discussed. Polycarbonate membranes having pore size varying between 800 - 80 nm have been used as the templates. And, an elaborate study leading to the optimization of the reaction parameters has been discussed in this chapter.

Solvothermally synthesized CdS nanoforms, discs, rods, wires, tetrapods, lamellas, cauliflower morphology and CdS/ZnS nanoslabs, have been discussed in *Chapter 6* of this thesis. The effect of dopants, like Mn, Eu and Tb has been studied along with the annealing effect. Both types of products in the powder /free ensemble form and as vertically standing crop on the Cd substrate have been obtained.

Owing to the importance of the luminescent properties of ZnS and CdS mate-

rials, the photoluminescence properties of the nanoforms synthesized in this entire work have been discussed separately in *Chapter 7*. We have tried to study the effect of the dopants on the PL properties of the matrix materials elaborately. These properties can be directly used for the device fabrication.

Conclusions from the complete work described in this thesis are presented in *Chapter 8*.

Chapter 2

ZnS and CdS Materials

ZnS and CdS are II-VI compound semiconductors, which contain the elements of group II and group VI, bonded together. These materials are important optoelectronic, luminescent and lasing materials because of the large range of electronic energy band gaps, which they exhibit. Zn and Cd metal elements can combine with sulphur to form stable crystalline semiconductor phases, which exhibit a variety of unique optical and electrical properties. These metal sulphide semiconductors possess a variety of crystalline phases, depending largely on the atomic radii ratios and electro-negativity differences of the constituent atoms of the semiconductors. In the past two decades, nanomaterials have been studied not only because of their fundamental interests, but also due to their potential in technological applications. Unlike their bulk counterparts, nanostructured materials exhibit very interesting size-dependent electrical, optical, magnetic, mechanical, and chemical properties.

Table 2.1 shows some of the numerical values related to the properties of ZnS and CdS materials.

2.1 Crystal Structure

In general, group II elements have two electrons in the s^2 outermost shell of the atom, while the group VI elements have six electrons due to s^2p^4 configuration. Group II elements are further divided into IIA (Be, Mg, Ca, etc.) and IIB (Zn, Cd, Hg) groups. Due to the large difference between electron affinity and electronegativity between groups IIA and VI, the outermost electrons of group IIA atoms are fully donated to those of group VI atoms, during the bond formation. Then they form octahedral configuration like in the case of NaCl. However, due to high ionization potential, group IIB cannot fully donate their electrons to group VI atoms during bond formation. Therefore, in this case covalent bonds are formed with tetrahedral based zincblende and wurtzite crystal structures [4]

2.1.1 Wurtzite Crystal Structure

Wurtzite structure is one of the most common crystal structures of semiconductors. Semiconductors, those crystallize in wurtzite structure, include nitrides (GaN, AlN, BN), II-VI semiconductors (ZnO, ZnS, ZnSe, CdS, CdSe, ZnTe, CdTe), SiC, InAs, etc. The wurtzite hexagonal crystal structure has been named after the French Chemist C. A. Wurtz, in 1861. The unit cell parameters of wurtzite are, $a = b = 3.81\text{Å}, c = 6.23\text{Å}$. The wurtzite structure is non-centrosymmetric (i.e., lacks inversion symmetry). Due to this, wurtzite crystals can (and generally do) have properties such as piezoelectricity and pyroelectricity, which centrosymmetric crystals lack.

This structure consists of two interpenetrating hcp lattices, where for one hcp the basis is formed by Zn/Cd at 0 and S at $a_1/3 + a_2/3 + a_3/2$, while in the second hcp S is residing at 0 and Zn at $a_1/3 + a_2/3 - a_3/2$. The separation between the two hcp lattices is the bond length between Zn/Cd and S. The wurtzite crystal structure is shown in figure 2.1.

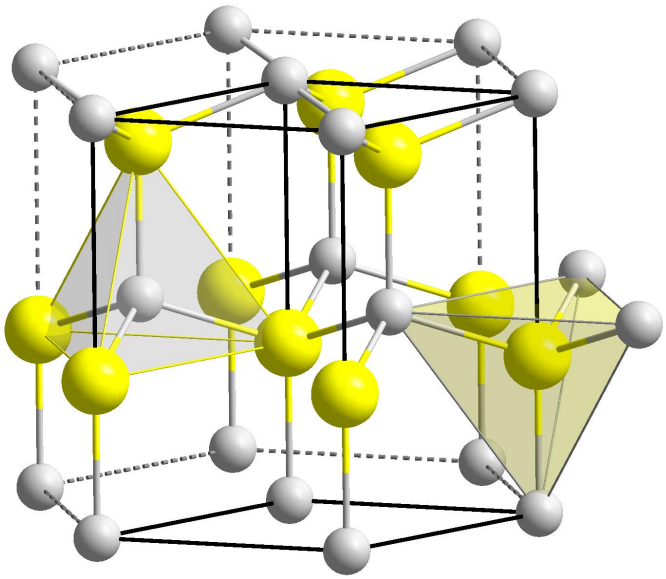

Figure 2.1: Wurtzite crystal structure where yellow balls represent S atoms and grey balls represent Zn/Cd atoms

2.1.2 Zinc Blende Crystal Structure

The zinc blende structure, as shown in figure 2.2, has been named after the mineral zincblende (sphalerite), the cubic phase of ZnS. It corresponds to the diamond

structure with two different atoms forming the basis. For example, each atom of Zn/Cd has four nearest neighbors of S atom and vice a versa. Zinc blende can be best thought of as a face-centered cubic array of anions, and cations are occupying one half of the tetrahedral holes. Each ion is 4-coordinate and has local tetrahedral geometry. Unlike wurtzite, zinc blende is its own antitype – the anion and cation positions in the cell can be interchanged. In fact, replacement of both the Zn and S with C gives the diamond structure [5].

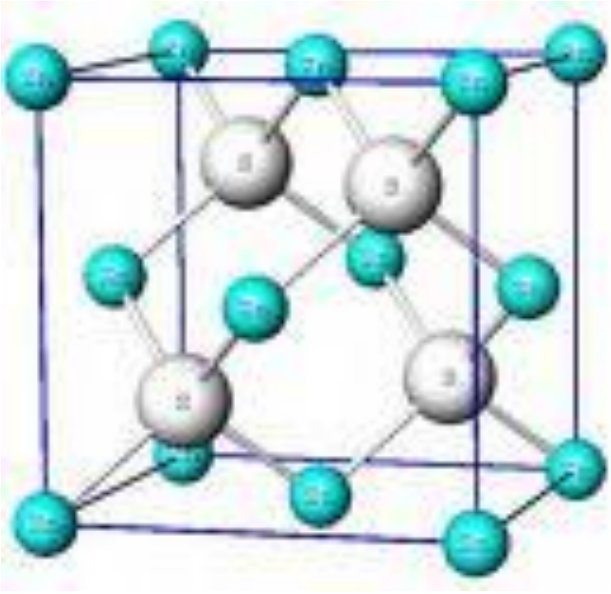

Figure 2.2: Zinc blende crystal structure, where blue balls represent Zn/Cd atoms and grey balls represent S atoms

2.1.3 Crystal Structure of ZnS and CdS

Both zinc sulphide and cadmium sulphide crystallize in two forms - wurtzite and zinc blende (sphalerite). Both sphalerite and wurtzite are intrinsic, wide-bandgap semiconductors.

In case of ZnS, the cubic form has a bandgap of 3.54 eV at 300 K whereas the hexagonal form has a band gap of 3.91 eV. The transition from the sphalerite form to the wurtzite form occurs at around 1020 ^{o}C. The ionic radius of the zinc(II) ion is 0.74 angstrom and that of the sulfide ion is 1.70 angstrom. The ratio of radii for the cation and anion is thus $r_{+}/r_{-} = 0.74/1.70 = 0.44$; With this ratio, one might expect the zinc(II) ions to occupy octahedral holes. However, the value of 0.44 is slightly larger than $\mathrm{r}_{hole}/\mathrm{r} = 0.414$ for an octahedral hole. In this case, the zinc(II) ions occupy tetrahedral holes. If the sulfide ions originally adopt a hexagonal closest-packed structure, the ZnS crystal is wurtzite. If the sulfide ions originally adopt a cubic closest-packed structure, the ZnS crystal is zinc blende.

However, cadmium sulfide is a yellow colored, direct band gap semiconductor (gap 2.42 eV) [6]. CdS has been extensively used in photo-conducting cells, being effective in UV and blue parts of the spectrum [7]. Like ZnS, it has two crystal forms - the more stable hexagonal wurtzite structure (found in the mineral Greenockite) and the cubic zinc blende structure (found in the mineral Hawleyite). In both of these forms the cadmium and sulfur atoms are four coordinate [8].

2.2 Native defects in ZnS and CdS

ZnS and CdS contain either intrinsic, associated with Zn/Cd or S vacancies/interstitials, or extrinsic point defects, due to impurity or dopants. The defects in semiconducting materials are known to cause changes in the optical and electrical properties. The doubly ionized Zn vacancy is the most well characterized point defect in ZnS, and is reported to create a defect level $\sim$ 1.0 - 1.1 eV above the ZnS valance band edge [9]. However, a singly ionized Zn vacancy is reported to create a defect level in the range 0.2 - 0.6 eV above the valence band.

2.3 Luminescence in ZnS and CdS [10]

ZnS phosphors form one of the most important groups widely used in many applications such as cathode-ray tubes, vacuum florescent displays and electroluminescent panels. Luminescent centres in ZnS can be classified by spatial distribution of the degree of localization of an electron wavefunction, which makes luminescence transition. The delocalized types are excitons and donor-acceptor pairs and localized types are transition metal or rare earth ions.

Undoped colloidal CdS particles emit self-activated green and red luminescence, attributed to direct electron-hole recombination and sulphur vacancies (Vs), respectively. The luminescence spectra of CdS depend on the impurity and stoichiometric composition, temperature of the sample, intensity of exciting light, and the aggregate state of the compound. This luminescence arising due to the electron-hole

radiative recombination at the defect levels, can be explained by Schon-Klasens model, Lambe-Klick model and Williams model. According to Williams model, the luminescence is supposed to result from the electron transitions between donor and acceptor levels. The radiative energy is given by subtracting the ionization energies of the isolated donors and acceptors from the band gap value, and then adding the energy shift in these levels due to Coulombic interaction. The emission due to transition metal dopants are referred to intra-centre transitions, occurring between the levels of $3d^n$ configurations. The excitation of the semiconductors with energy higher than the bandgap value results in the formation of free electron-hole pairs, which is explained using the hydrogen-like system. The binding energy of CdS is 29 meV and the radius of exciton ground state is 3.2 nm. The free exciton luminescence is observed in the resonance with the exciton absorption line as well as lower energies under simultaneous excitation of optical phonons.

Table 2.1: Data for various parameters related to ZnS and CdS materials [11]

Property	**ZnS**	**CdS**
Zinc Blende Lattice Parameter a_o at 300K	0.541 nm	0.582 nm
Zinc Blende Nearest-Neighbour Dist. at 300K	0.234 nm	0.252 nm
Zinc Blende Density at 300K	4.11 g cm^{-3}	4.87 g cm^{-3}
Wurzite Density at 300K	3.98 g cm^{-3}	4.82 g cm^{-3}
Phase Stable at 300K	zinc blende, wurtzite	wurtzite
Melting Point	1850 ^{o}C (wurtzite, 150 atm.)	1750 ^{o}C (wurtzite, 100 atm.)
Refractive Index		
zinc-blende structure:	2.356	2.506
wurzite structure:	2.378	2.529

Chapter 3

Characterization Techniques

Characterization of materials regarding determination of elemental composition, estimation of trace impurities, structural analysis, morphological analysis, identification of crystalline phases and information on crystal defects play an important role for the quality control and development of advanced materials and their use in precision devices. 0-D and 1-D nanostructures have been characterized by their structural, compositional, morphological and optical properties. The techniques used include X-ray diffraction (XRD), Scanning electron microscopy (SEM), Transmission electron microscopy (TEM), Energy dispersive analysis of X-rays (EDAX), Fourier transform infra-red spectroscopy (FTIR), UV-visible absorption spectroscopy, Room temperature photoluminescence (PL), and Time-resolved photoluminescence (TRPL) studies.

3.1 Structural characterization by XRD

X-ray diffraction (XRD) is a powerful non-destructive technique for characterizing crystalline materials. It provides information on structures, phases, preferred crystal orientations (texture) and other structural parameters such as average grain size, crystallinity, strain, and crystal defects.

In 1919 A. W. Hull gave a paper entitled, "A New Method of Chemical Analysis". Here he pointed out that **"....every crystalline substance gives a pattern; the same substance always gives the same pattern; and in a mixture of substances, each substance produces its pattern independently of the others."** X-ray diffraction peaks are produced by constructive interference of a monochromatic beam scattered from each set of lattice planes at specific angles. The peak intensities are measured by the atomic decoration within the lattice planes. Consequently, the X-ray diffraction pattern is the fingerprint of periodic atomic arrangements in a given material.

The mechanism of XRD is simple. On exposing the crystalline sample to a monochromatic X-ray beam, the constructive diffraction (or interference) pattern, from parallel planes of atoms with inter-planar spacing, d, is observed. This happens for the angle of incident, θ, satisfying the Bragg's law , as shown in figure 3.1.

According to the Bragg‘s law:

$$2d\ sin\theta = n\ \lambda \tag{3.1}$$

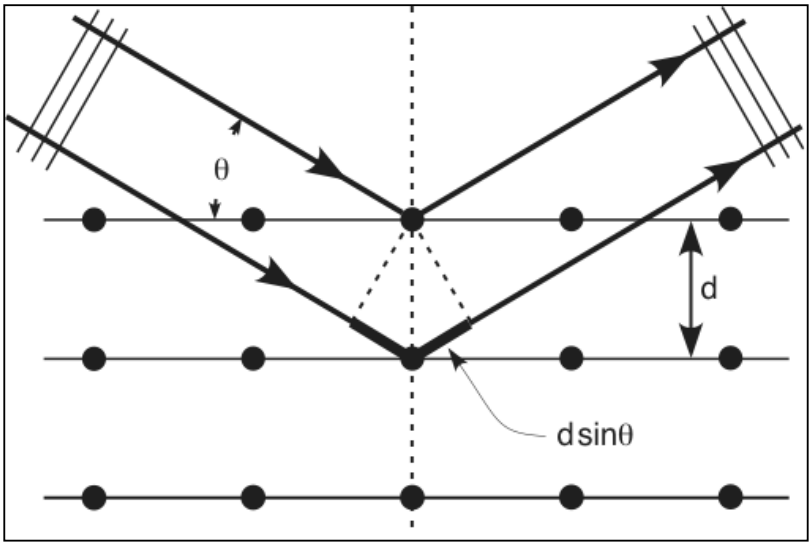

Figure 3.1: Schematic diagram of Bragg diffraction from a set of parallel planes

Where n is integer that indicates the order of the reflection, θ is Bragg angle, and λ is the wavelength of the X-ray beam. By measuring the Bragg angle, θ, the interplanar distance, d, can be obtained if the wavelength of the X-ray beam is known.

The common experimental methods of XRD include X-ray diffractometer, Laue method, rotating-crystal method, moving-film method, and powder method. There are three kinds of measurement strategies for detecting the intensity of diffracted X-ray beam in diffractometer method [12]:

1. Fixed crystal and fixed detector

2. Moving crystal and fixed detector, in which the crystal is rotated slowly

through its reflecting range about the detector axis (ω scan), while the detector is stationary at the appropriate 2θ angle.

3. Moving crystal and moving detector, in which the crystal and detector are suitably coupled for each reflection, and both rotate through the diffractometer axis ($\omega, 2\theta$ s `

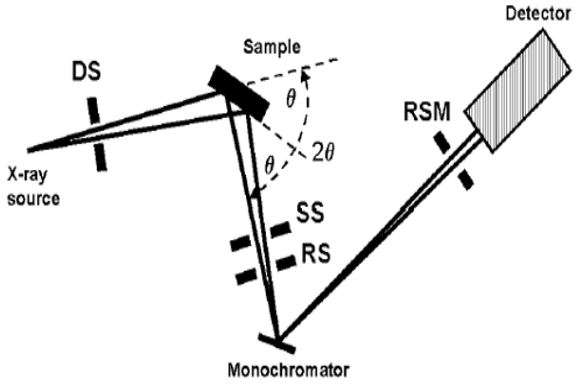

Figure 3.2: Schematic diagram of X-ray 2θ scan

Figure 3.3: Pictorial view of the X-ray diffractometer

The ray diagram and the pictorial view of the X-ray diffractometer are shown in figures 3.2 and 3.3 respectively. The intensity of the diffracted X-rays is measured as a function of the diffraction angle 2θ. This diffraction pattern is used to identify the specimen's crystalline phases. XRD is non-destructive and does not require elaborate sample preparation and as a result it is widely used method for sample characterization. As expected, diffraction patterns of the nanoparticles are considerably broadened compared to the bulk due to the finite size effect. The crystal

size of the nanoparticles can be obtained from the broadened XRD pattern. The broadening of the X-ray diffraction peaks can be quantitatively expressed in terms of the Scherrer‘s formula [13],

$$L = 0.9\ \lambda / B\ cos\ \theta \tag{3.2}$$

where, B is the full width at half maximum (FWHM) of the peak, L is the coherence length (used as crystallite diameter for non spherical clusters), λ is the wavelength of the X-ray radiation and θ, the angle of reflection.

In addition, the lines may be broadened as a result of lattice strain in the region of crystal diffraction. Strain gives rise to a variation of the interplanar spacing and hence diffraction occurs over a range, $\Delta\theta$. As reported by Smallman and Bishop [14], the broadening due to strain B_s, can be given as:

$$B_s = \eta\ tan\ \theta \tag{3.3}$$

where η is the strain distribution. Ignoring the crystal constant, 0.9, the broadening due to ‘particle-size‘, given by Scherrer formula, can be taken as:

$$B_p = \lambda / t\ cos\ \theta \tag{3.4}$$

where, t, is the effective particle size. Now, using equations 3.3 and 3.4, the experimentally measured broadening, B, can be used to plot a graph between $B\ cos\ \theta / \lambda$

and $sin\ \theta/\lambda$, according to the following equation:

$$\frac{B\ cos\ \theta}{\lambda} = \frac{\eta\ sin\ \theta}{\lambda} + \frac{1}{t} \tag{3.5}$$

The intercept gives the measure of effective particle size, t, and the slope gives the measure of strain distribution η.

XRD data has also been used to quantify the preferred crystallographic orientation by texture analysis. The texture coefficients (TCs) of preferred orientation were determined by Harris formula [15]:

$$TC(h_i k_i l_i) = [I(h_i k_i l_i)/I_0(h_i k_i l_i)][\frac{1}{n}\sum I(h_i k_i l_i)/I_0(h_i k_i l_i)]^{-1} \tag{3.6}$$

Where $TC(h_i k_i l_i)$ is the texture coefficient,$I(h_i k_i l_i)$ is the observed intensity and $I_0(h_i k_i l_i)$ is the standard intensity of the $(h_i k_i l_i)$ plane, and n is the reflection number. The value of texture coefficient indicates the maximum preferred orientation of the nanorods [16] along the corresponding diffraction plane.

3.2 Scanning Electron Microscopy (SEM)

SEM is one of the most widely used techniques for the morphological characterization of nanomaterials. It can resolve morphologic details of nanostructures of sizes greater than 5 nm, and possesses a depth of focus of more than 500 times higher than that of an optical microscope at equivalent magnification, yielding a characteristic three-dimensional appearance useful for understanding the surface structure of a sample.

In a typical SEM, an electron beam, with a very fine spot size of 5-10 nm and having energy ranging from a few hundred eV to 50 keV, is thermionically emitted by the electron gun. It is rastered over the surface of the specimen by deflection coils, as shown in figure 3.4. As the electrons strike and penetrate the surface of the specimen, a number of interactions occur that result in the emission of electrons and photons from the sample, and SEM image is produced by collecting the emitted electrons on a cathode ray tube (CRT). The image observed on this screen is similar to the optical image and the specimen is usually titled towards the collector at a low angle ($< 30^o$) to the horizontal, for general viewing [14]. Also an electron in the SEM collides and ejects a core electron from the atom in the sample. The excited atom will decay to its ground state by emitting a characteristic X-ray photon, which has been used for chemical characterization. The specimen preparation is done by rigidly mounting the sample on the specimen holder, called a specimen stub. For conventional imaging in the SEM, the specimen must be electrically conductive, at least at the surface, and electrically grounded to prevent the accumulation of electrostatic charge at the surface. The non-conductive samples are sputter coated with an ultra thin layer of electrically-conducting materials like gold, gold-palladium and platinum.

The biggest advantage of the SEM is that one can investigate the morphology of the sample without disturbing the original nature of the products. It may be mentioned here that there is a possibility of high-energy electron beam destroying the integrity of the nanomaterials in certain cases. Thus, surface morphology and

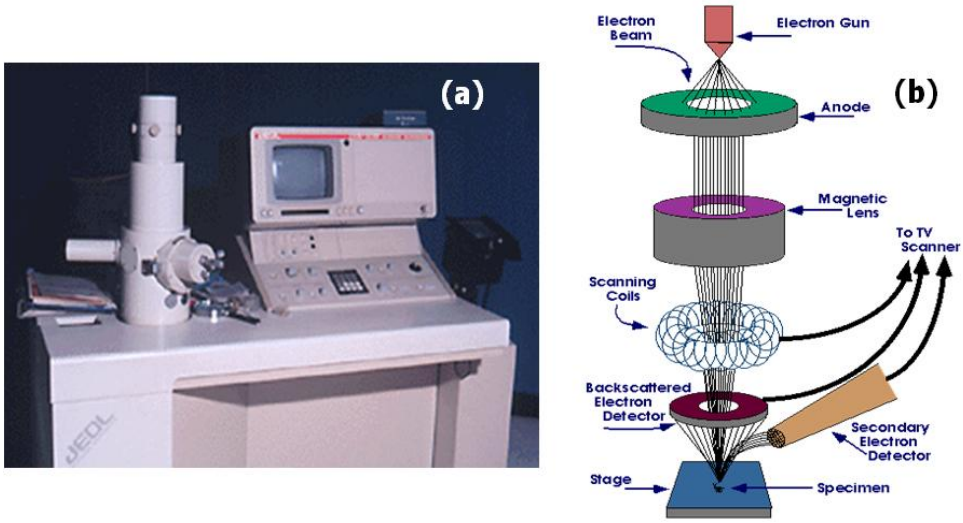

Figure 3.4: (a) Pictorial and (b) schematic view of an SEM machine

dimensions of the nanomaterials beyond a few nanometers could be estimated accurately using the SEM images.

3.3 Transmission Electron Microscopy (TEM)

Transmission electron microscopy (TEM) is an important tool to study the morphology and crystal structure of the samples having ultra thin dimensions (less than 200 nm) such that the high energy electrons (100 keV to 1 MeV) can pass through them [17]. It is important to a materials scientist because of its high resolution (0.1 nm in latest TEMs), owing to the small de Broglie wavelength of the electrons, apart from its ability to provide both image and diffraction information from a single sample.

Like all matter, electrons have both wave and particle properties and their wave-

like properties mean that a beam of electrons can be made to behave like a beam of electromagnetic radiation. The wavelength of electrons, λ, is found to be given by equating the de Broglie equation to the kinetic energy of an electron:

$$\lambda = h/(2mqV)^{1/2} \tag{3.7}$$

Here, h, is the Planck's constant, m, is the rest mass of electron and q, the electron charge.

For 100 kV accelerating voltage, the wavelength can be as small as 0.0039 nm. The higher the operating voltage, V, of a TEM instrument, the greater is its lateral spatial resolution. However, the resolution of TEM is limited by the equipment defects.

Accelerated electrons (a few hundred keV), when focused on a material, produce many interactions, as shown in figure 3.5. Electrons can traverse the sample without any interaction (unscattered electrons) or can be scattered, elastically or inelastically, on their way (scattered electrons). Elastic scattering involves no energy loss and gives rise to diffraction patterns. However, inelastic scattering, caused by the interaction between the primary electrons and the sample electrons, leads to spatial variation in the intensity of the transmitted electrons [18].

An electron microscope consists of an electron gun and an assembly of lenses all enclosed in an evacuated column. These lenses are of magnetic type, i.e. current-carrying coils which are completely surrounded by a soft iron shroud except for a

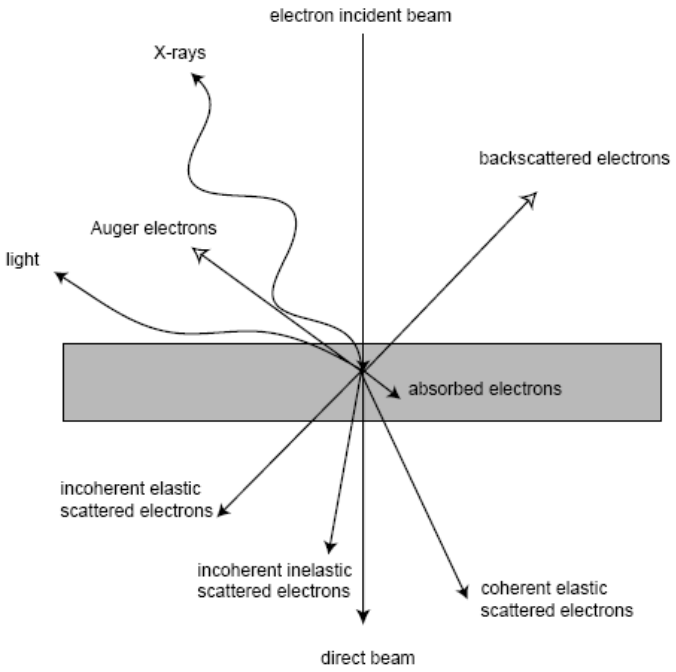

Figure 3.5: Interactions between material and the accelerated electrons

narrow gap in the bore, energized by d.c. [14]. Their focal length can be regulated by varying the current through the coils. Thus, the electron beam can be collimated by the condenser lenses as shown in figure 3.7. The two modes of a TEM are imaging and diffraction, which are explained as follows (see figure 3.8):

Imaging mode: As shown in figure 3.7, the transmission electron microscope is constituted of: (1) two or three condenser lenses to focus the electron beam on the sample, (2) an objective lens to form the diffraction in the back focal plane and the image of the sample in the image plane, (3) some intermediate lenses to magnify the image or the diffraction pattern on the screen. If the sample is thin (< 200 nm) and constituted of light chemical elements, the image presents a very low contrast when focused. To obtain amplitude contrasted image, an objective diaphragm is inserted in the back focal plane to select the transmitted beam (and possibly a few

Figure 3.6: Pictorial view of (a) TEM machine (b) Sample holder and the carbon coated copper grids

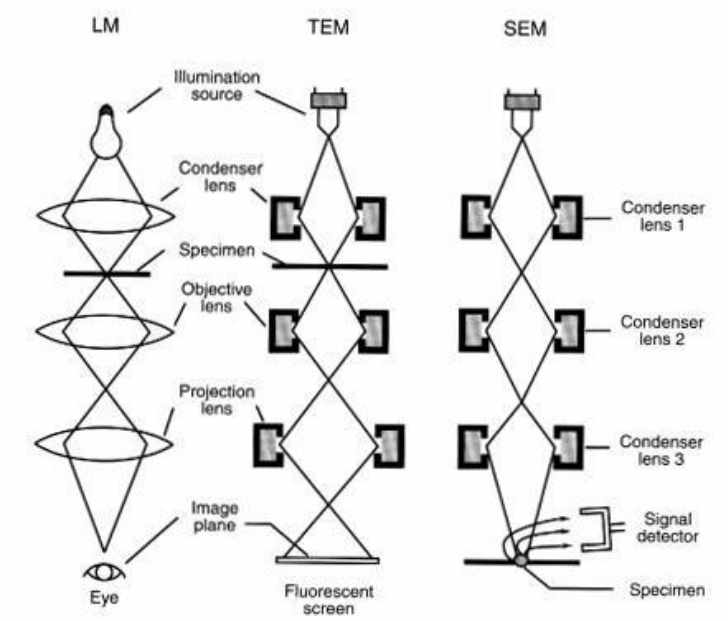

Figure 3.7: Ray diagram showing the comparison between the light microscope (LM), transmission electron microscope (TEM) and scanning electron microscope (SEM)

diffracted beams): the crystalline parts in Bragg orientation appear dark and the amorphous or not Bragg oriented parts appear bright. This imaging mode is called bright field mode BF. If the diffraction is constituted by many diffracting phases, each of them can be differentiated by selecting one of its diffracted beams with the objective diaphragm. To do that, the incident beam must be tilted so that the diffracted beam is put on the objective lens axis to avoid off-axis aberrations. This mode is called dark field mode DF. The BF and DF modes are used for imaging materials to nanometer scale.

In general, the image in TEM can be formed by using the central spot or by using some or all of the scattered electrons. If the central spot is used to form the image, the resultant image is called a bright-filed (BF) image. If the scattered electrons are

selected to form the image, the image is called dark-field (DF) image.

Diffraction mode: The selected area diaphragm is used to select only one part of the imaged sample for example a particle or a precipitate. Therefore, this mode is called selected area electron diffraction SAED. Selected-area electron diffraction (SAED) is used to determine the crystal structure through TEM.

The spherical aberrations of the objective lens limit the area of the selected object to a few hundred nanometers. Nevertheless, it is possible to obtain diffraction patterns of a smaller object by focusing the electron beam with the projector lenses to obtain a small spot size on the object surface (2-10 nm). If the scattering centers, in the specimen, are arrayed in an orderly, regular manner (as in a crystal), the scattering is coherent and results in spot patterns. If the specimen is poly-crystalline, ring patterns are expected. No matter what kind of specimen is used, SAED pattern contains a bright central spot that contains directly transmitted electrons and some scattered electrons. The spots of SAED become disks whose radii depend on the condenser diaphragm. This is called micro-diffraction. SAED and microdiffraction patterns of a crystal enable to obtain the symmetry of its lattice and calculate its interplanar distances (using the Bragg‘s law). This is useful to confirm the identification of a phase, after assumptions generally based on the literature of the studied system and on chemical analyses.

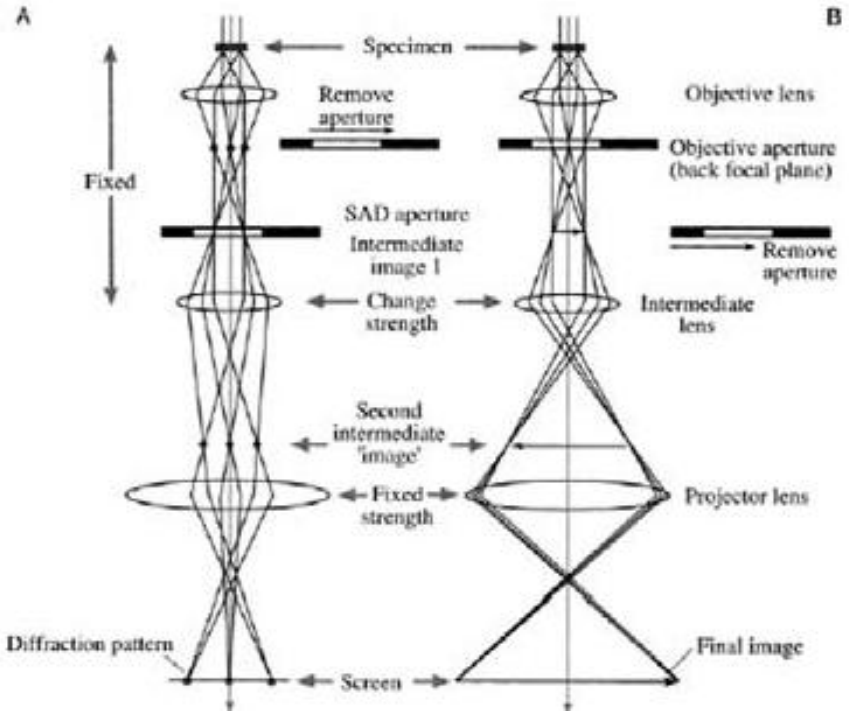

Figure 3.8: Ray diagram showing the two modes of TEM (A) diffraction mode, (B) image mode

3.4 Energy Dispersive Analysis of X-rays (EDAX)

EDAX is an analytical technique used for elemental analysis or chemical characterization of a sample [19]. Energy dispersive analysis of X-ray (EDAX) is one kind of electron spectroscopy, which relies on the emission of photons (X-ray) from the unique energy levels of the atom under investigation. When an incident electron or photon, such as X-ray or γ-ray, strikes an atom, an electron from an inner shell is ejected and leaves a hole in the inner shell. An electron from an outer shell fills the hole by lowering its energy, and simultaneously the excess energy is released through emission of an X-ray, which is utilized in EDAX. As the energy of the X-rays is characteristic of the difference in energy between the two shells, and of the atomic structure of the element from which they were emitted. The measurement of the elemental composition of the specimen becomes possible. The amount of energy released by transferring the electron depends on which shell it is transferring from, as well as which shell it is transferring to. From the EDAX spectra, one can investigate the elementary composition of the materials and the presence of any foreign impurity in the sample. Stoichiometry of the sample is also tested from the elementary analysis of the EDAX spectrum. EDAX systems are most commonly found on scanning electron microscopes (SEM-EDAX) and electron microprobes. Scanning electron microscopes are equipped with a cathode and magnetic lenses to create and focus a beam of electrons. A detector is used to convert X-ray energy into voltage signals; this information is sent to a pulse processor, which measures the signals and passes them onto an analyzer for data display and analysis.

The EDAX spectrum is just a plot of how frequently an X-ray is received for each energy level. An EDAX spectrum normally displays peaks corresponding to the energy levels for which the most X-rays had been received. Each of these peaks is unique to an atom, and therefore corresponds to a single element. The higher a peak in a spectrum, the more concentrated the element is in the specimen.

An EDAX spectrum plot not only identifies the element corresponding to each of its peaks, but also the type of X-ray to which it corresponds. For example, a peak corresponding to the amount of energy possessed by X-rays emitted by an electron in the L-shell going down to the K-shell is identified as a K-α peak. The peak corresponding to X-rays emitted by M-shell electrons going to the K-shell is identified as a K-β peak (figure 3.9).

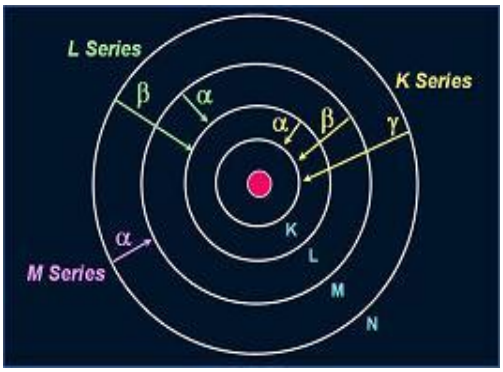

Figure 3.9: Emission of X-rays from specific shells of the atom under consideration

3.5 Fourier Transform Infra-red Spectroscopy (FTIR)

Infrared radiation in the range of 4000-400 cm^{-1} is of practical use to an organic chemist, as it is absorbed and converted by an organic molecule into energy of molecular vibration. These absorption spectra appear as bands since a single vibrational energy change is accompanied by a number of rotational energy changes [20]. These spectra behave like a fingerprint of the samples because the frequency or wavelength of absorption depends on the relative masses of the atoms, the force constants of the bonds, and the geometry of the atoms. Therefore, the FTIR spectra can be used to identify the unknown materials, to determine the quality or consistency of a sample and the amount of components in a mixture.

Molecular bonds vibrate at various frequencies depending on the elements and the type of bonds. For any given bond, there are several specific frequencies at which it can vibrate. According to quantum mechanics, these frequencies correspond to the ground state (lowest frequency) and several excited states (higher frequencies). One way to cause the frequency of a molecular vibration to increase is to excite the bond by having it absorb light energy. For any given transition, between two states the light energy (determined by the wavelength) must exactly equal the difference in the energy between the two states [usually ground state (E_0) and the first excited state (E_1)]. The energy corresponding to these transitions between molecular vibrational states is generally 1-10 kcal/mole which corresponds to the infrared region of the electromagnetic spectrum.

Difference in energy = Energy of light Absorbed

$$E_1 - E_0 = hc/l \tag{3.8}$$

where h is the Plank's constant, and c, the speed of light.

As shown in the schematic diagram, figure 3.10, the infrared energy is passed through an interferometer, where the 'spectral encoding' takes place. The resulting signal passes through the sample, where specific frequencies of energy, which are uniquely characteristic of the sample, are absorbed. The beam finally passes through the detector for final measurement. The detectors used are especially designed to measure the special interferogram signal. The measured signal is digitized and sent to the computer where the fourier transformation takes place. The final infrared spectrum is then presented to the user for interpretation and any further manipulation. The analysis is done by matching the data with the known signatures of identified materials in the FTIR library.

3.6 UV-visible Absorption Spectroscopy

When an incident light beam reaches a medium, part of the beam will be reflected by the medium, part of the beam will be transmitted through the medium, and the rest of the beam will be absorbed. UV-visible absorption spectroscopy involves the absorption spectroscopy of photons in visible, near UV and near infra red region of

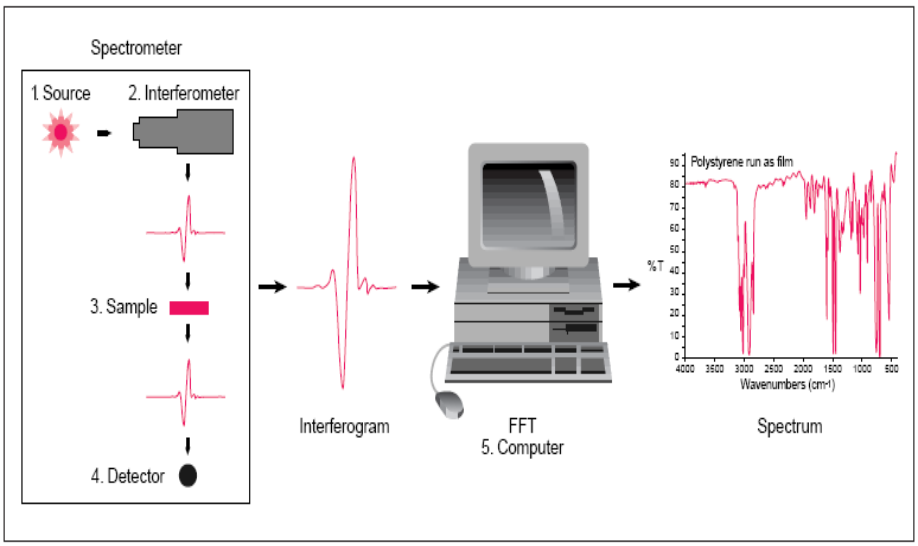

Figure 3.10: Schematic diagram of the signal generation in FTIR spectroscopy [21]

the electromagnetic spectra. It is complementary to the fluorescence spectroscopy as it deals with the transitions from the ground state to the excited state. This characterization technique is based on the principle of Beer-Lambert's law which states that, there is a logarithmic dependence between the transmission (or transmissivity), T, of light through a substance and the product of the absorption coefficient of the substance, α, and the distance the light travels through the material, i.e., the path length, l. The absorption ability of a matter is measured by its absorption coefficient. The absorption coefficient can, in turn, be written as a product of a molar absorptivity of the absorber, ε, and the concentration, c, of the absorbing species in the material.

Mathematically,

$$T = I/I_o = 10^{-\alpha l} = 10^{-\varepsilon lc} \tag{3.9}$$

The transmission (or transmissivity) is expressed in terms of an absorbance (A), which for liquids is defined as:

$$A = -log_{10}(I/I_o) \tag{3.10}$$

The absorption spectrometer is generally composed of a light source, monochromator, and a detector. Figure 3.11 shows the schematic diagram of the dual-beam spectrophotometer used in the work.

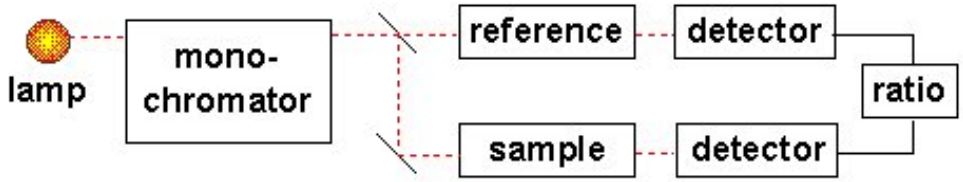

Figure 3.11: Schematic diagram of the dual-beam spectrophotometer

The spectrometer is equipped with two continuous light sources- a tungsten lamp for measuring transmittivity in the visible range (from 1000 nm to 320 nm) and a deuterium lamp for the measurement in ultraviolet range (from 320 nm to 200 nm). Light beam is first split into a monochromatic one by the monochromator, and then it is made incident onto the sample. The transmitted beams both from the reference and the sample, are measured and recorded by the computer, and the ratio between

the two is used for further calculations.

The energy difference between the highest lying valence (the highest occupied molecular orbit, HOMO) and the lowest lying conduction (the lowest unoccupied molecular orbit, LUMO) bands is designated as the fundamental band gap. The penetration depths of electromagnetic radiation are in the order of 50 nm through most of the optical spectra (visible region). Such small penetration depths limit the use of optical absorption spectroscopy for the characterization of bulk materials but can be easily utilized for the nanoscale materials. The absorption edge determined from the peak minimum of the first derivative of the absorption plot gives the band gap of the materials under study. The optical band gap was also determined from the absorbance/transmission spectra. The variation of absorption coefficient (α) with the wavelength (λ) was obtained from the transmittance vs. λ plot. If m represents the nature of optical transition in a semiconducting material, the absorption coefficient (α) may be expressed as [22, 23].

$$\alpha = A/h\nu[h\nu - E_g]^m \tag{3.11}$$

where A is an optical constant, E_g is the band gap of the semiconductor corresponding to the particular value of m. The parameter m, representing the nature of optical transition, may have certain specific values such as, 1/2, 2, 3/2 or 3 corresponding to the allowed direct, allowed indirect, forbidden direct and forbidden indirect transitions respectively [24]. For allowed direct transition $(\alpha h\nu)^2$ versus $h\nu$ was plotted and the linear portion of it was extrapolated to $\alpha = 0$ value to obtain

the corresponding band gap energy, E_g.

3.7 Photoluminescence (PL) studies

All forms of light emission, except the emission of radiation from a hot body (incandescence), are called luminescence. There are many types of luminescence depending upon the source of excitation. Chemiluminescence is produced by certain chemical reactions, chiefly oxidations, at low temperatures; electroluminescence is produced by electric discharges, which may appear when silk or fur is stroked or when adhesive surfaces are separated; triboluminescence is produced by rubbing or crushing crystals; bioluminescence is luminescence produced by living organisms and is thought to be a type of chemiluminescence. The luminescence observed in the sea is produced by living organisms, many of them microscopic, collected at the surface. Other examples of bioluminescence include glowworms, fireflies, and various fungi and bacteria found on rotting wood or decomposing flesh. If the luminescence is caused by absorption of some form of radiant energy, such as ultraviolet, visible or infra-red radiation, then the luminescence is known as photoluminescence.

Photoluminescence (PL) spectroscopy is a powerful technique for investigating the electronic structure, both intrinsic and extrinsic, of semiconducting and semi-insulating materials. It gives an excellent picture of the overall crystal quality and purity, in terms of the impurity concentrations, identification of defect complexes and measurement of band gap of semiconductors. On illuminating the semiconduct-

ing material with a light source having photon energy greater than the band gap of the material, electrons are excited to the conduction band, leaving behind holes in the valence band. The recombination of these electron-hole pairs, leads to the emission of photons having wavelength characteristic to the material.

Depending upon the nature of the ground and the excited states, the photoluminescence is divided into two types: fluorescence and phosphorescence (shown in figure 3.12). In case of a singlet excited state, the electron in the higher-energy orbital has the opposite spin orientation as that of the second electron in the lower orbital. These two electrons are said to be paired. Fluorescence is the emission which results from the return to the lower orbital of the paired electron. Such transitions are quantum mechanically, 'allowed', and the emissive rates are typically near 10^8 s^{-1}. These high emissive rates result in fluorescence lifetimes near 10^8 s or 10 ns. Whereas, in a triplet state these electrons are unpaired, that is, their spins have the same orientation. A change of spin orientation is needed for a triplet state to return to the singlet ground state (see figure 3.12). Phosphorescence is the emission which results from transition between states of different multiplicity, generally a triplet excited state returning to a singlet ground state. Such transitions are forbidden and the emission rates are slow (10^3 to 1 s^{-1}) [25]. Typical phosphorescent lifetimes range from milliseconds to seconds, depending primarily upon the importance of deactivation processes other than emission.

In semiconductors, depending on the character of the radiative transition, one distinguishes between instrinsic, extrinsic and exciton luminescence. Intrinsic, or

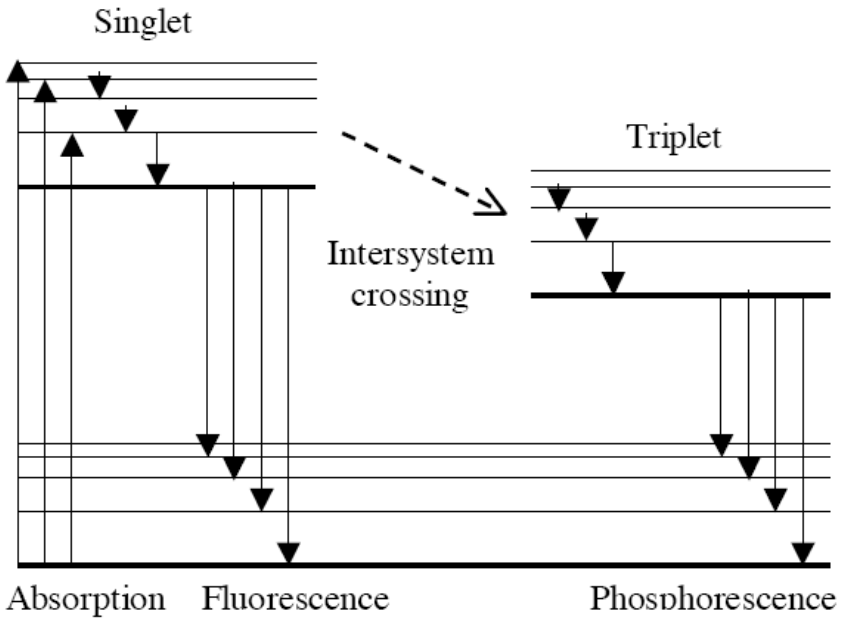

Figure 3.12: Fluorescence and phosphorescence mechanism

band-to-band luminescence is connected with the recombination of free electrons and holes. Extrinsic or impurity luminescence originates from the radiative recombination of free electrons with holes bound to acceptors, or of free holes with bound-to-donar electrons, the so-called bound-to-free emission, as well as from radiative donar-acceptor recombination and optical transitions between the levels of the same impurity centre. Exciton luminescence appears due to the recombination of free, impurity-bound or localized excitons [26].

Figure 3.13 shows the schematic diagram of a spectrofluorometer, consisting of a xenon lamp as a source of exciting light. The excitation grating (acts as a monochromator) is used to select the desired wavelength for the excitation beam. The excitation wavelength can be varied from 220 nm to 800 nm. Light emission from the sample is first diffracted by the diffraction grating. The diffracted emission beam

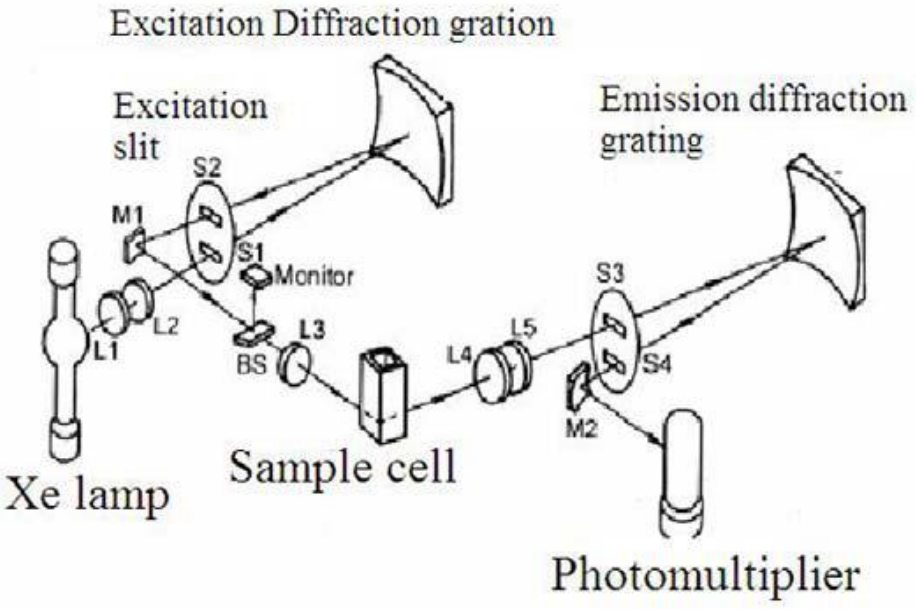

Figure 3.13: Schematic diagram of Hitachi 2500 spectrofluorometer

is then sent to the photomultiplier through the exit slit and finally recorded by the computer. The excitation spectrum can be also measured with this spectrometer. To do so, the emission-diffraction grating has to be fixed at the desired position. The variation of excitation wavelength is achieved by rotating the excitation-diffraction grating.

Most of the spectrofluorometers are equipped so as to record both the excitation and the emission spectra. Emission spectrum is the wavelength distribution of an emission measured at a single constant excitation wavelength. Conversely, excitation spectrum is the dependence of emission intensity, measured at a single emission wavelength, upon scanning the excitation wavelength [25].

3.8 Time-resolved Photoluminescence Studies (TRPL)

Time-resolved measurements are widely used in florescence/photoluminescence spectroscopy, as it contains more information than steady-state data. It provides an effective nondestructive technique for studying the dynamics of impurities and lattice defects in semiconductors [27].

Static and dynamic quenching can be differentiated using life time measurements. Formation of static ground-state complexes do not decrease the decay time of the uncomplexed fluorophores because only the unquenched fluorophores are observed. Dynamic quenching is a rate process acting on the entire excited-state population, thus decreases the mean decay time of the entire excited-state population [25].

TRPL can be measured using two methods: the time-domain and the frequency-domain methods. In time-domain method, the sample is excited by using a pulsed source of light. The intensity is measured across the time scale. The pulse width of size less than the decay time of the sample is used. Then calculations are made to find out the life-time/decay-time, trap depth, oscillator strength, etc. Intensity-modulated light (typically sine-wave modulation) is used to excite the sample in case of frequency-domain method of TRPL. Variation in the intensity of the incident light is done at high frequency. The inverse of this frequency can be compared to the decay time. On excitation of the sample, the emission is forced to respond at the same modulation frequency. The lifetime value of the sample causes a delay in

the emission, w.r.t the excitation. On measuring this delay as a phase shift, decay-time/life-time values can be calculated.

We have used the time-domain method in our work. The intensity of the luminescent radiation, at time, t, is given as [28, 29]

$$I = I_o e^{-pt} \tag{3.12}$$

where I_o is the intensity of radiation at cut-off position, the constant, $p = 1/\tau$, is the transition probability of the corresponding radiative transition, and τ is the life-time of the excited state. The decay curves can be peeled -off into three components by the peeling-off method of Bube. The results of decay curves can be expressed as:

$$I = I_{o1} exp(-p_1 t) + I_{o2} exp(-p_2 t) + I_{o3} exp(-p_3 t) + \tag{3.13}$$

where p_1, p_2 and p_3 are the transition probabilities. I_{o1}, I_{o2}, I_{o3}..... are the intensities at the cut-off position for three probability values. In the present investigation only three components have been taken because further components were having the life times of the order of few seconds.

The value of trap-depth E, has been calculated using the Boltzmann‘s equation [28]:

$$p = Se^{-E/kT} \tag{3.14}$$

where S is the escape frequency factor ($\sim 10^9$ s^{-1}), k is the Boltzmann's constant and T, the absolute temperature. The distribution of traps in the energy band gap of the nanoparticles has been studied using the following equation:

$$I = I_o t^{-b} \tag{3.15}$$

where b is the decay constant. The value of decay constant explains the distribution of the trapping states introduced by the dopant within the band gap of the phosphor. If the value of decay constant is unity, the traps introduced by the impurity are uniformly distributed within the band gap of the nanoparticles. Otherwise there will be non-uniform distribution of the traps.

Chapter 4

Syntheses of undoped/doped ZnS nanoparticles by chemical precipitation technique

4.1 Chemical Precipitation Technique

The most common approach to the syntheses of colloidal nanoparticles/quantum dots is the controlled nucleation and growth in a solution of chemical precursors containing the metal and the anion sources, also called controlled arrested precipitation [30]. Michael Faraday gave this technique by forming monodisperse gold colloids in 1857. In general, chemical precipitation means the formation of a separable solid substance from a solution, either by converting the substance into an insoluble form or by changing the composition of the solvent to diminish the solubility of the substance in it. The distinction between precipitation and crystallization lies largely in whether emphasis is placed on the process by which the solubility is

reduced, or on that by which the structure of the solid substance becomes organized [31]. This technique is used industrially to remove metal ions from aqueous solutions. For example, silver ions present in a solution of a soluble salt, such as silver nitrate, are precipitated by addition of chloride ions, provided, for example, by a solution of sodium chloride; the chloride ions and the silver ions combine to form silver chloride, a compound that is not soluble in water.

For II-VI materials, solutions of chemical reagents containing the group II and VI species are rapidly mixed and homogeneously stirred. Consequently, a large number of nucleation centers are formed. Ostwald ripening, which is the growth of larger particles at the expense of smaller particles to minimize the higher surface free energy associated with particles of small size, is limited by using the surfactants/ capping agents. These surfactants/capping agents like, polyvinyl pyrrolidone (PVP) and thiophenol, form coordinating ligands in the solvent. Furthermore, pH, temperature, concentration of the surfactant, stirring speed and duration, are some of the parameters which are responsible for the resulting size distribution of the nanoparticles.

ZnS is an important and among the oldest members of the family of wide-gap (3.66 eV, at room temperature) semiconductors and probably the most important material used as phosphor host [32]. Due to unique optical properties and potential applications, the doped semiconductor nanocrystals have attracted extensive research interests [33]. This II-VI compound semiconductor has been studied for a variety of applications such as optical coatings, photoconductors, optic modulators,

electro-optic modulators, flat panel displays, electroluminescent devices, sensors, and lasers, and also have been applied in photocatalysts, infrared windows, pigments, and non-linear optical devices [34, 168].

4.2 Backdrop

In recent years, research involving undoped and doped nanocrystalline ZnS has grown extensively, mainly due to the high quantum luminescence efficiencies that have been reported [36, 37]. Transition metal doped II-VI chalcogenide nanomaterials are being studied vastly for their potential applications in solar cells [38], light emitting diodes [39, 40] and in bio-label fields [41]. ZnS nanoparticles have been mostly synthesized with methods like inverse micelle [42], zeolite [43] or vapor phase condensation method [44], but have certain problems such as low powder collection and complex processing procedures. Chemical precipitation method is better than other techniques for producing efficiently luminescent nanophosphors in terms of process simplicity, effectiveness of doping, higher yield, and has a very simple procedure with a very low cost apparatus [45].

Numerous researchers have investigated the structural and luminescent properties of doped phosphor nanoparticles, especially Mn^{2+}-doped ZnS nanocrystals, as ZnS can be doped with Mn very easily [46]. This doping causes a visible orange luminescence at about 585 nm. It is well known that ZnS doped with Mn exhibits attractive light-emitting properties with increased optically active sites for applica-

tions as efficient phosphors [47]. These nanomaterials behave differently from bulk semiconductors as they are influenced by various surface states arising due to quantum confinement effect and large surface-to-volume ratio [48].

The increase in particle size enhances surface energy resulting in agglomeration of the particles. In order to control the size of the semiconductor nanoparticles, numerous researchers have used the capping agents [45]. But if surfactant or capping agent is used to confine particles, then it becomes difficult to completely washout the surfactant molecules from the surface of the nanoparticles, so unintentional defect layers could be introduced in the product, and, therefore it is always desirable to develop technique to synthesize nanoparticles without any capping agent.

Much work has been reported on the optical properties of ZnS nanoparticles doped and co-doped with Mn [33, 176], Co [50], Cu [45, 51], Ni [52, 53], and Fe [54]. However, Ni doped ZnS nanoparticles still need further investigation for their luminescent properties. The potential application of transition metal doped ZnS nanoparticles, as solar cells and LEDs, require the study of the effect of prolonged UV-irradiation on their optical properties. Use of such solar cells or LEDs in space ships and in UV radiation prone regions will possibly show remarkable change in their optical properties viz-a-viz the ambient conditions. Such effects of the prolonged UV-irradiation on the optical properties of ZnS nanoparticles doped with Ni have not been reported in the literature to the best of our knowledge.

Copper doped ZnS crystals are well known as classical luminophosphors as they

have efficient phosphorescent properties and high photosensitivity [55]. Moreover, efforts have been made to study the optical properties of copper doped ZnS nanocrystals, not only because it is a widely luminescent material, but also on account of the stronger interaction of copper ions with the host ZnS. However in our work, we not only demonstrate the remarkable changes in the optical properties of the Cu-doped ZnS nanoparticles by varying the concentration of the dopant but also report the remarkable changes observed on their prolonged exposure to the UV radiation.

In 2001, Yang et al. [50] have reported the synthesis and photoluminescence (PL) characteristics of the first realization of ZnS nanoparticles doped with Co^{2+} and Co^{3+} for the first time. They found that Co^{2+} enhanced the fluorescence efficiencies of ZnS nanocrystallites remarkably. Also, they found that Co^{3+} is a fluorescence decay agent, although it only reduces an electron as combining with Co^{2+}.

Quadri et al. [56] have reported that in case of the nanometer-sized ZnS particles, the equilibrium transition temperature from the zinc-blende to wurtzite structure is significantly reduced (400 ^{o}C) as compared to the bulk value (1020 ^{o}C).

Apart from the doping of transition metal ions, trivalent rare earth ions like: Eu^{3+}, Tb^{3+}, Er^{3+}, have been doped in semiconductor nanoparticles, and their luminescence properties have been reported [57, 58]. Chen et al. in 2001, have reported the luminescence properties of Eu^{2+} in ZnS:Eu nanoparticles [47]. They found that the emission bands of 4.2, 3.2 and 2.6 nm ZnS:Eu nanoparticles are peaked respectively at 670, 580 and 520 nm. They have given the possible mechanism for the

size dependence of the $4f^6 5d^1(t_{2g}) - 4f^7$ transition of Eu^{2+} in ZnS:Eu nanoparticles, and have concluded that the decrease in the electron-phonon coupling and in crystal field strength upon a decrease in size are the two major factors responsible for the shift.

4.3 Preparation

Chemical precipitation technique has been used to synthesize undoped and doped ZnS nanoparticles, at room temperature and in aqueous solution. Also, in some of the experiments, the nanoparticles have been passivated by using the surfactants , so as to tailor their size. All the chemicals used in the syntheses are of analytic grade and have been used without any further purification.

For the synthesis of undoped ZnS nanoparticles, 0.5 M Zinc acetate (aqueous media) solution was slowly mixed with 0.5 M sodium sulphide solution. To dope the ZnS nanoparticles with transition metal impurities, like: Mn, Cu, Ni, Co, and the rare earth impurity, Eu, the corresponding salt solutions having varying concentration of the dopant ions, were mixed with the zinc acetate solution. Table 4.1 shows the list of all the dopants and the corresponding salts used in their syntheses. The mixing was done with constant magnetic stirring at room temperature. A colloidal suspension was obtained immediately, after adding Na_2S solution. The solution was centrifuged and the precipitates were filtered and washed several times using distilled water and ethanol. Then the products were dried in vacuum oven

at a temperature of about 60 ^{o}C. The dried flakes were crushed in a pestle-mortar till very fine powder was obtained. This powder was collected in airtight containers and was used for further characterization.

To see the effect of prolonged UV radiation on the physical and chemical properties of the synthesized nanomaterials, the ZnS nanoparticles doped with Cu and Ni were UV-irradiated by a 40 watt UV lamp at a wavelength of 255 nm for 24 hour at room temperature. Also, the effect of annealing on the ZnS:Co and ZnS:Eu has been studied in the present work. The nanoparticles were placed in a preheated oven, at 200 ^{o}C, in the nitrogen gas atmosphere. After 2 hour, they were allowed to cool normally to the room temperature.

4.4 Reaction Mechanism

Chemical precipitation is widely used for the preparation of colloidal nanoparticles. In the method described above, we used the following exchange/replacement reactions:

$$Zn(CH_3COO)_2 \rightarrow Zn^{2+} + 2CH_3COO^{-} \tag{4.1}$$

$$Zn^{2+} + Na_2S \rightarrow ZnS + 2Na^{+} \tag{4.2}$$

Zn^{2+} ions react with a sulphide (S^{2-}) source, i.e., Na_2S (sodium sulphide). ZnS forms instantaneously at a certain pH value. The equilibrium of Eq. (4.1) lies far on the right side because of the high solvation energy in water. The driving force for

Table 4.1: List of the synthesized samples along with the dopants, dopant salt and the capping agent

Sample Type	**Dopant Salt**	**Capping Agent**	**Concentration of the dopant**
ZnS	—	None	—-
ZnS:Mn	$Mn(CH_3COO)_2$	None	0, 5.0, 10.0 and 15.0 (atomic %)
ZnS:Ni	$NiCl_2.6H_2O$	Polyvinyl pyrrolidone K-30 (PVP)	0.01, 0.05, 0.1, 0.5, 1.0, 3.0, 5.0 and 10.0 (atomic %)
ZnS:Cu	$CuSO_4.5H_2O$	PVP	0.01, 0.05, 0.1, 0.5, 1.0, 3.0, 5.0 and 10.0 (atomic %)
ZnS:Co	$CoCl_2.6H_2O$	PVP	0.01, 0.05, 0.1, 0.5, 1.0, 3.0, 5.0 and 10.0 (atomic %)
ZnS:Eu	$EuCl_3.6H_2O$	Mercaptoethanol ($HOCH_2CH_2SH$)	0.0, 1.0, 1.5, 2.0, 2.5, 3.0 4.0 5.0 mM

the reaction (4.2) is the formation of strong ZnS bonds. The ZnS particles nucleate by consuming more Zn^{2+} and S^{2-} ions from the solution, which can be explained on the basis of Ostwald ripening [59].

In addition to the above mentioned ions, acetate ions (Ac^{-}), Na^{+} and the dopant related ions, like Mn^{2+}, Ni^{2+}, Cu^{2+}, Co^{2+} , Eu^{3+}, are also present in the solution, during the synthesis via chemical precipitation route. For example, in case of Mn doping, due to high surface energy of the particles, acetate (Ac^{-}) and sulphur (S^{2-}) anions accumulate around the ZnS particles, thereby attracting the Zn^{2+} , Na^{+} and Mn^{2+} cations. Zn^{2+} and Mn^{2+} react with S^{2-} get incorporated into the crystal lattice whereas Na^{+} ions accumulate to form the stern layer over ZnS nanoparticles, attracting Ac^{-} ions to form a diffuse layer over it. In this way, the particle growth is completely stopped [60]. This leads to the concept of in-built passivating agent, ie. Ac^{-} ions.

However, to passivate the surface of the nanoparticles, polyvinyl pyrrolidone (PVP) has also been used in case of ZnS doped with Cu, Ni and Co, and mercaptoethanol has been used in case of ZnS:Eu nanoparticles.

4.5 Phase Detection

The crystal structure of the ZnS nanoparticles have been studied through X-ray diffraction (XRD) studies, using a PANalyticals X'Perto Pro X-ray diffractometer

using copper characteristic wavelength, 1.518 $\AA$. It has been reported that for bulk ZnS, two basic structures are observed: the cubic zinc-blende structure (3C) and the hexagonal wurtzite structure (2H) [61]. The most stable form of zinc sulfide is the cubic structure and in the bulk it transforms to wurtzite structure at 1020 ^{o}C. The bulk zinc sulfide melts at a temperature of 1650 ^{o}C.

Figure 4.1 shows the X-ray diffraction (XRD) pattern for ZnS:Mn (5 %, 10 %, 15 at. %) nanocrystallites, which indicate that all the samples are of zinc blende (cubic) structure. Diffraction peaks from (111), (220) and (311) planes have only appeared in XRD patterns and all other high angle peaks have submerged in the background due to the large line broadening, which is attributed to nanosize of the particles. The average crystallite size was estimated from the line broadening of the XRD peaks using the Scherrer's equation [62]

$$d = 0.89\lambda/\beta \; cos \; \theta_B \tag{4.3}$$

where d is the average crystallite size, λ is the wavelength of Cu $K\alpha$ (1.541) radiation, β (in radian) is the full width at half maximum (FWHM), and θ_B is the Bragg angle. The average crystallite size, calculated using above formula, was found to be between 2 and 3 nm. No passivating agent has been used in the fabrication of the ZnS:Mn nanoparticles but still no apparent difference was observed in the XRD peak shape and broadening of ZnS nanoparticles even after two weeks of the fabrication. This suggests that no agglomeration of the particles has taken place.

The XRD patterns of $Zn_{0.995}Ni_{0.005}S$ nanoparticles before and after UV-irradiation have been shown in figure 4.2. In both the spectra, the diffraction peaks

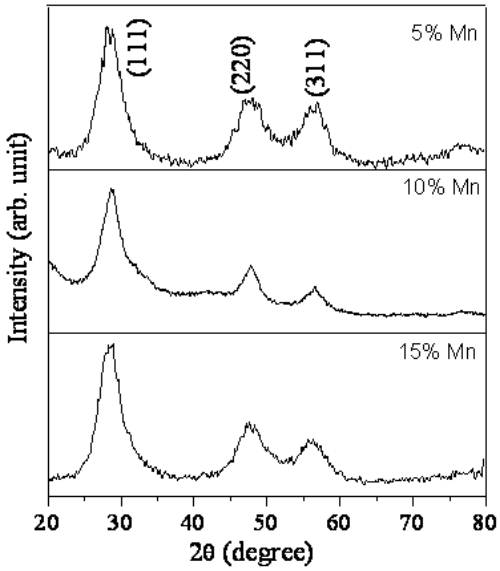

Figure 4.1: XRD pattern of Mn^{2+} doped ZnS nanoparticles (average crystallite size $\sim$ 2 nm calculated from peak broadening).

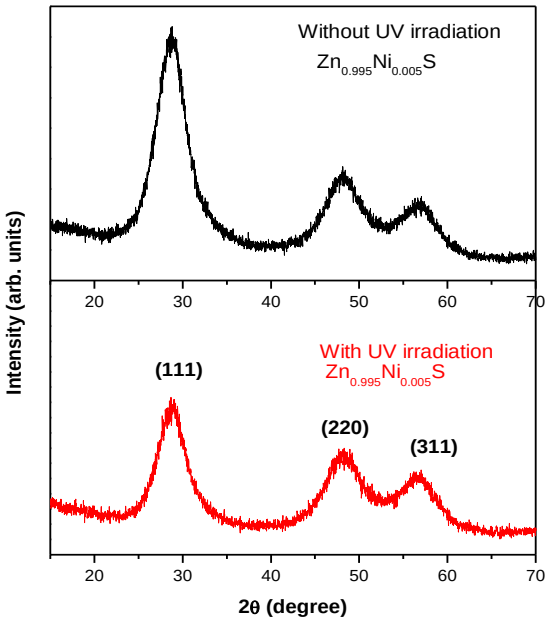

Figure 4.2: XRD patterns of ZnS:Ni (0.5 %) nanoparticles, with and without UV-irradiation

positioned at 29.11 ^{o}, 48.35 ^{o}, and 56.45 ^{o}, correspond respectively to the (111), (220), and (311) crystal planes of the zinc blende cubic phase of ZnS. No impurity or dopant related peak has been observed. The crystallite size has been calculated by using the Scherrer's equation (4.3), and is found to be 2.5 nm. On prolonged UV-irradiation, the peak intensity of (111) plane has decreased with no shift in the peak position as shown in figure 4.2.

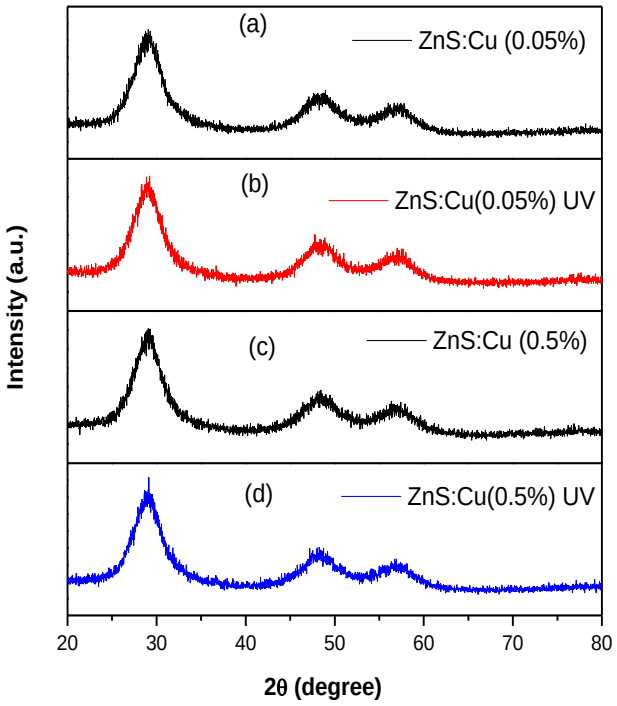

Figure 4.3: XRD pattern of ZnS:Cu nanoparticles having various concentration of Cu (a, b) 0.05 at. %, (c, d) 0.5 at. % ; (with and without UV-irradiation)

As shown in figure 4.3, the XRD pattern of the ZnS:Cu nanoparticles having varying concentration of the dopant as well as the respective samples, when exposed to UV radiation, are found to be identical with respect to the peak position and the peak broadening.

Figure 4.4 shows the XRD pattern of ZnS:Co (0.5 % and 5.0 %) nanoparticles with and without annealing at 200 ^{o}C for 2 hour in nitrogen gas atmosphere. Before anealing the nanoparticles, they exhibit broad diffraction peaks corresponding to the zinc blende cubic phase of ZnS. The diffraction peaks correspond to the (111), (220) and (311) crystal planes and the Scherrer‘s equation has been used to give the crystallite size, which lies between 2 and 3 nm. No impurity or dopant related peak has been observed in the samples without annealing. However, on annealing, it has been observed that the XRD pattern has changed drastically for the concentration of Co, 0.5 % and 5.0 %. As shown in figure 4.4, the annealed ZnS:Co (0.5 %) nanoparticles exhibit diffraction peaks centered at 26.88^o, 28.58^o, 30.45^o, 39.63^o, 47.58^o, 51.80 ^{o} and 56.4 ^{o}, which match well with the standard JCPDS data card No. 36-1450. These peaks correspond respectively to the (100), (002), (101), (102), (110), (103) and (112) crystal planes of the hexagonal wurtzite- 2H planes of ZnS. This shows a transition from the cubic to hexagonal phase at 200 ^{o}C, in case of the nanoparticles. Qadri et al. [56] have also reported such transitions in the undoped ZnS nanoparticles, but they have observed no such transition below 350 ^{o}C. However, they had annealed the samples for only 45 minute and had allowed the sample to cool at regulated speed of 15-20 celcius/minute.

The XRD pattern of the annealed ZnS:Co (5.0 %) nanoparticles, also show the hexagonal wurtzite phase. In addition to these, there are some diffraction peaks positioned at 2θ values of 41.90^o, 48.88^o, and 72.48^o, which match with the diffraction peaks of cobalt sulphide (Co_3S_4), according to the PDF card No. 110121. Such

dopant realated peaks have not been observed in the samples without annealing and also in the samples having less concentration of Co. This shows that the transition from cubic to hexagonal phase of ZnS has also led to the crystallization of the cobalt sulphide in case of 5.0 % doping of the ZnS nanoparticles. The sharp peaks of cobalt sulphide show the high crystalline quality.

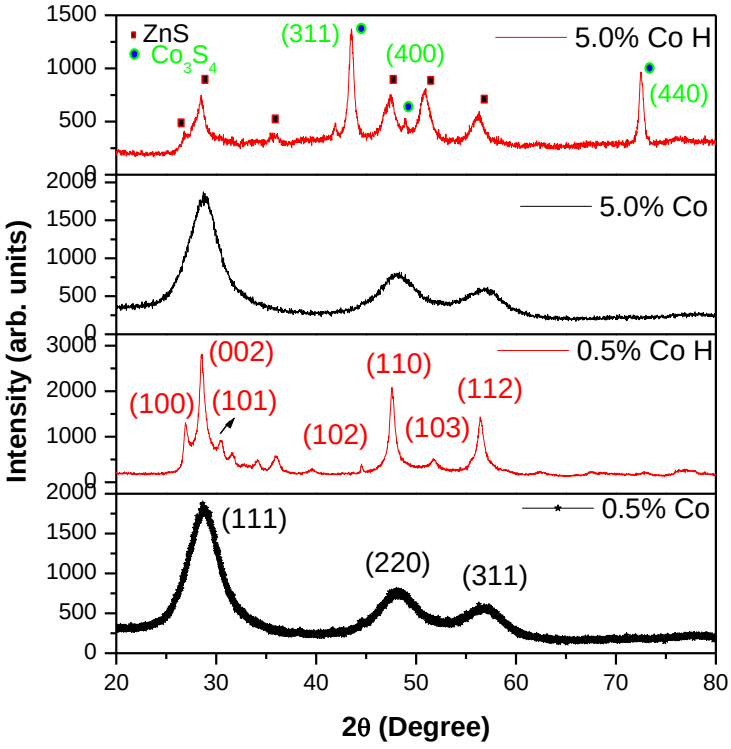

Figure 4.4: XRD patterns of ZnS:Co nanoparticles with and without annealing at 200 ^{o}C for 2 hour in nitrogen gas atmosphere

Figures 4.5 and 4.6 show the XRD patterns of ZnS:Eu (1 mM and 4 mM) nanoparticles, with and without annealing of 200 ^{o}C for 2 hour in the nitrogen gas atmosphere. All the patterns match well with the cubic zinc blende crystal structure, with broad diffraction peaks corresponding to (111), (220) and (311) crystal

planes of ZnS. No transition from cubic phase to hexagonal phase has been observed in these samples. However, a slight increase in the intensity of the diffraction peaks of the annealed samples has been observed. The crystallite size has been calculated to lie between 4 and 5 nm in case of the synthesized ZnS nanoparticles, which has increased by about 0.5 nm in case of the annealed samples.

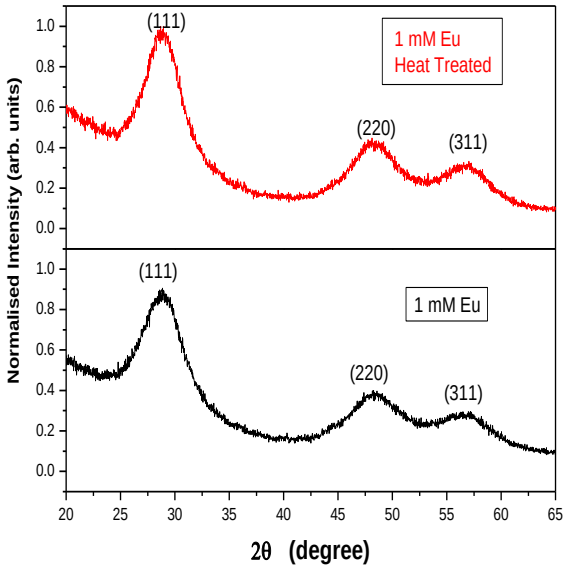

Figure 4.5: XRD pattern of ZnS:Eu (1 mM) nanoparticles, with and without heat treatment

Therefore, it has been observed that chemical precipitation of undoped and doped ZnS nanoparticles leads to the cubic zinc blende crystal phase. Moreover, the mean calculated crystallite size of the ZnS nanoparticles is of the order of or less than the Bohr's Exciton radius for ZnS, i.e., 5 nm. This shows that the synthesized nanoparticles are in the quantum confinement regime. Thus, these nanoparticles may also be called the quantum dots.

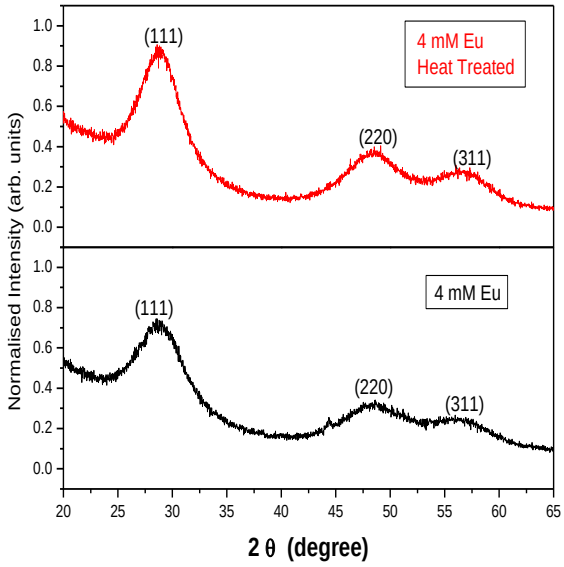

Figure 4.6: XRD pattern of ZnS:Eu (4 mM) nanoparticles, with and without annealing

4.6 Energy Dispersive X-ray (EDX) Spectroscopy

The composition of the nanoparticles was analyzed by EDX studies, using Noran System Six. Electron beam induced inner-shell ionization and subsequent emission of characteristic fluorescence are analyzed in order to obtain the composition.

As shown in figure 4.7, the EDX analysis of ZnS:Eu (3 mM) gives the Zn L-fluorescence (Lα around 1 keV energy range), Zn K-fluorescence (Kα in the energy range 8-9 keV and Kβ in the energy range 9-10 keV), S K-fluorescence (Kα in the 2-3 keV energy range) and Eu L & M-fluorescence (Lα, Lβ and Lγ in the energy range 6-8 keV, and Mα in the energy range 0.5 to 1.5 keV) are observed. Apart from these the Kα fluorescence from carbon and oxygen has also been detected. The atomic ratio of Zn : S : Eu is 1.000 : 0.808 : 0.002. This shows that the incorporation of Eu is quite poor in the ZnS nanoparticles.

As explained by Blasse and Grabmaier in 1994 [63], there are several reasons for the poor incorporation of Eu^{3+} in nanocrystalline ZnS. First, the ionic radius of the Eu^{3+} ion (0.95) is larger than that of Zn^{2+} (0.75). For Eu^{3+} ion to replace a Zn^{2+} lattice site, the ZnS host lattice has to deform, which is energetically unfavorable. Besides, due to the large ionic radius, the Eu^{3+} ion prefers sites with high coordination numbers (six or higher). In ZnS, however, the coordination number of the cation lattice site is only four, which is very unusual for Eu^{3+}. In addition, the 3+ charge of the Eu^{3+} ion has to be compensated for somewhere in the lattice.

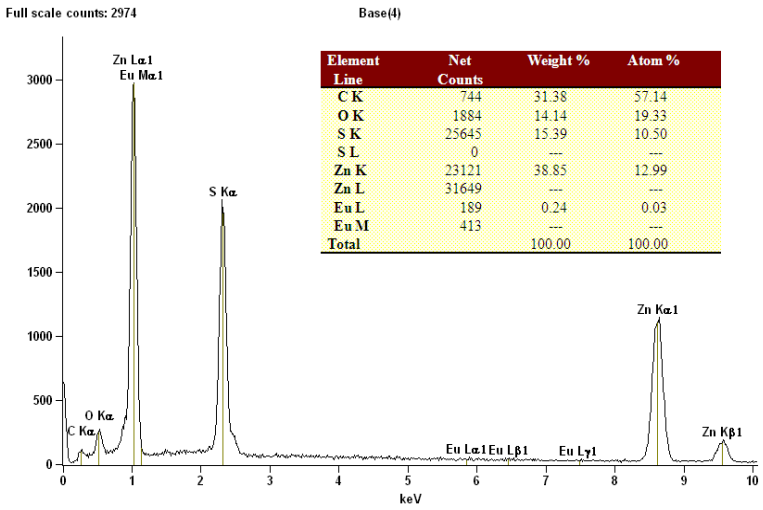

Figure 4.7: EDX spectrum of the ZnS:Eu (3mM) nanoparticles

4.7 Microstructural Analysis

Chemical precipitation leads to the synthesis of nanoparticles, and the XRD studies reveal that the crystallite size of the synthesized ZnS nanoparticles lies between 3 and 5 nm. Therefore, transmission electron microscopy (TEM) has been used to

study the morphology of the synthesized nanoparticles. The specimen preparation has been done by finely dispersing the nanoparticles in spectroscopic grade ethanol, and then putting a drop of the dispersed solution on the carbon coated copper grid.

Figure 4.8 (a) shows the TEM image of ZnS:Mn (5%) nanoparticles. The diameters of most of these particles lie in the range 3 and 5 nm. This can also be seen from the high-resolution transmission electron micrograph (HRTEM) in figure 4.8 (b). These results are nearly in accordance with those of the X-ray diffraction analysis. The selected area diffraction pattern, presented in the inset of Figure 4.8 (b), shows the crystallanity of the fabricated nanoparticles. The dominant diffraction patterns in the micrograph are indexed as (111), (220) and (311) planes of the cubical ZnS.

Figure 4.9 shows the high resolution transmission electron micrograph (HRTEM) of $Zn_{0.995}Ni_{0.005}S$ nanoparticles. The diameters of most of these particles lie in the range 3 and 5 nm. These results are also in accordance with those of the X-ray diffraction analysis. The selected area diffraction pattern presented, in the inset of figure 4.9, shows poly-crystallanity of the fabricated nanoparticles. The dominant diffraction patterns in the micrograph are indexed as (111), (220) and (311) planes of the cubical ZnS.

Figure 4.10(a) shows the transmission electron micrograph (TEM) of ZnS:Cu (0.5 at.%) nanoparticles. The diameters of most of these particles lie in the range 3 and 5 nm. The selected area diffraction pattern presented, in the inset of fig-

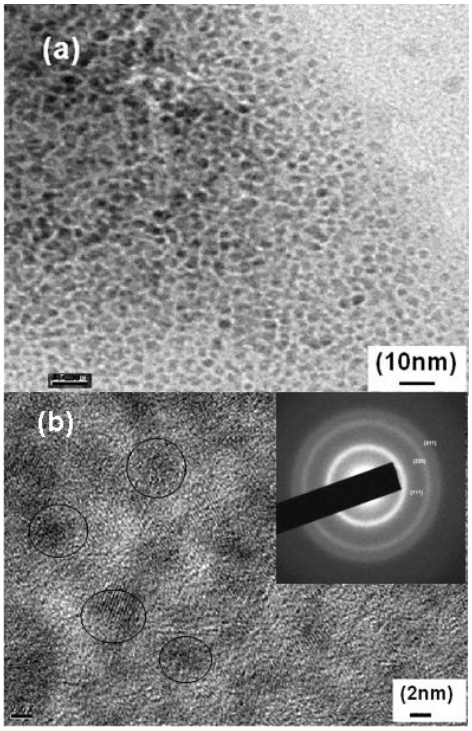

Figure 4.8: (a) Transmission electron micrograph (TEM) of ZnS:Mn (5 %) nanoparticles; (b) High resolution TEM and the inset shows the selected area diffraction pattern (SAED)

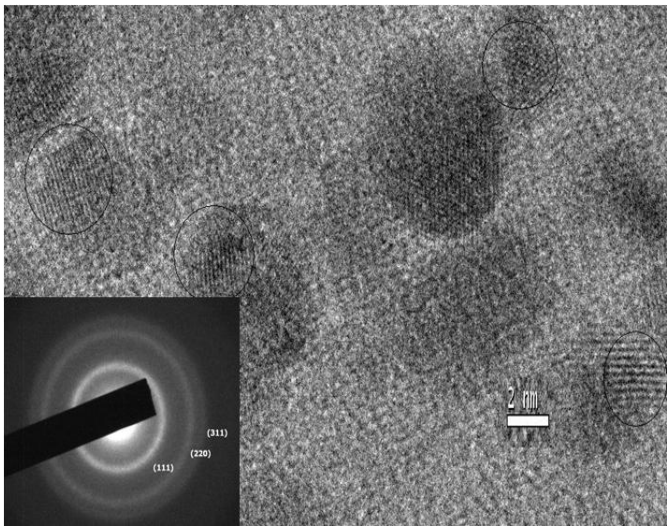

Figure 4.9: HRTEM image of $Zn_{0.995}Ni_{0.005}S$ nanoparticles, and the SAED pattern (inset) showing the polycrystalline nature of the nanoparticles

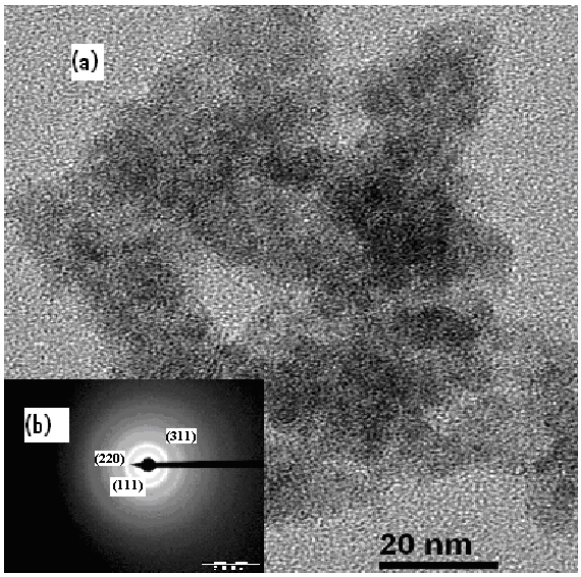

Figure 4.10: TEM image of the ZnS:Cu (0.5%) nanoparticles along with the SAED pattern in the inset.

ure 4.10(b), shows poly-crystallanity of the fabricated nanoparticles. The dominant diffraction patterns in the micrograph are indexed as (111), (220) and (311) planes of the cubical ZnS. Figures 4.8, 4.9 and 4.10 show the reproducibility of the results of the results obtained from the chemical precipitation technique, used to synthesize ZnS nanoparticles with different dopants.

4.8 FTIR Analysis

Figure 4.11 shows the FTIR spectra of the synthesized nanoparticles, confirming the interaction of acetate anions derived from the starting zinc acetate, with the ZnS nanoparticles. The bands at 1404 cm^{-1} and 1558 cm^{-1} can be assigned to the symmetric and asymmetric stretching of COO^{-} respectively [64]. The broad band at 3366 cm^{-1} is due to O-H stretching and band at 929 cm^{-1} due to O-H out of

plane bending. Whereas, the band having moderate intensity at 1339 cm^{-1}, may be due to the in-plane C-O-H bending [65]. A moderate intensity band at 1019 cm^{-1} may be due to S-O-C stretching. The stretching vibrations assigned to the C-S linkage occur in the region of 700-600 cm^{-1} and the weak S-S stretching vibration falls between 500 and 400 cm^{-1}. Thus, the acetate ions are acting as inbuilt surfactants to control the size of the ZnS nanoparticles.

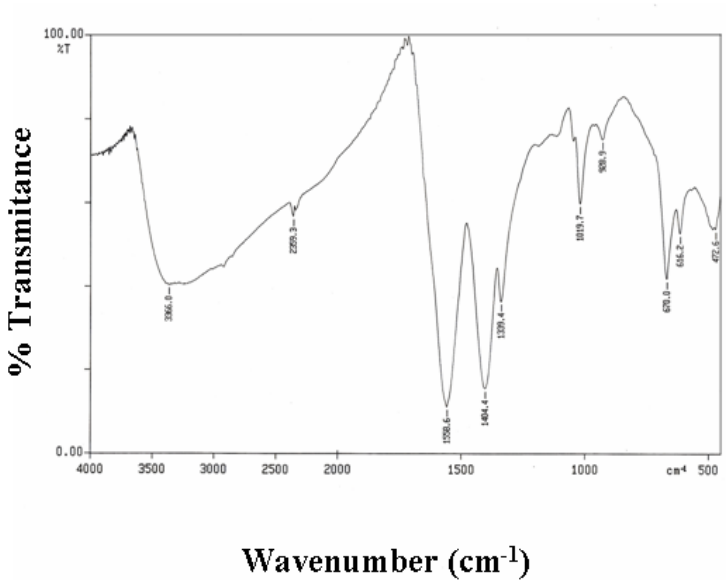

Figure 4.11: FTIR spectra of ZnS nanoparticles having a layer of acetate ions adhered to its surface

To confirm the presence of polyvinyl pyrrolidone- K30 (PVP) as a capping agent, and to investigate the effect of UV-irradiation on the surface chemistry of the synthesized nanoparticles, FTIR spectroscopy has been carried out. FTIR spectra of the PVP capped Ni doped ZnS nanoparticles, with and without UV-irradiation, have been shown in figure 4.12. The absorption peaks matches well with those of PVP according to the reported data [66, 67]. Broad band at 3366 cm^{-1} is due to the O-H stretching. The strong absorption peak at 1555 cm^{-1} is due to the C=O

bonding which has shifted to lower frequency as compared to the reported data for PVP due to the resonance effect. This occurs because of a weak coordinative chemical bonding between the carbonyl carbon and the Zn^{2+} ions. The absorption peak at 1413 cm^{-1} may be ascribed to the asymmetrical vibrations of the C-H in the methyl group whereas a weak absorption at 2889 cm^{-1} is due to the C-H stretching vibrations in tertiary C-H group [65]. This provides a direct evidence for the presence of PVP capping agent on the synthesized Ni doped ZnS nanoparticles. The FTIR spectrum of the UV-irradiation nanoparticles is almost similar to that of the as synthesized nanoparticles as shown in figure 4.12, apart from a slight shift in the broad absorption at 3366 cm^{-1} to 3084 cm^{-1}. This shows that the UV-irradiation has not altered the surface chemistry.

Moreover, the FTIR spectra of the undoped, and ZnS:Co (0.05 %) nanoparticles with and without annealing have also been shown in figure 4.13. These spectra are similar to those of Ni doped ZnS nanoparticles, showing the presence of PVP. However, the spectra for the annealed sample, shows a slight deviation from the unannealed sample. The intensity of the peaks centered at 1556 and 1406 cm^{-1} are too low. This might be due the evaporation of CO_2 at higher temperature, due to the presence of COO^- group.

As shown in figure 4.14, the FTIR spectra of ZnS:Eu (4mM) nanoparticles, with and without annealing, show the presence of stretching vibrations of the OH group, with a broad band centered at around 3373 cm^{-1}, and the band at 938 cm^{-1} due to O-H out of plane bending. This broad band has decreased in intensity and further

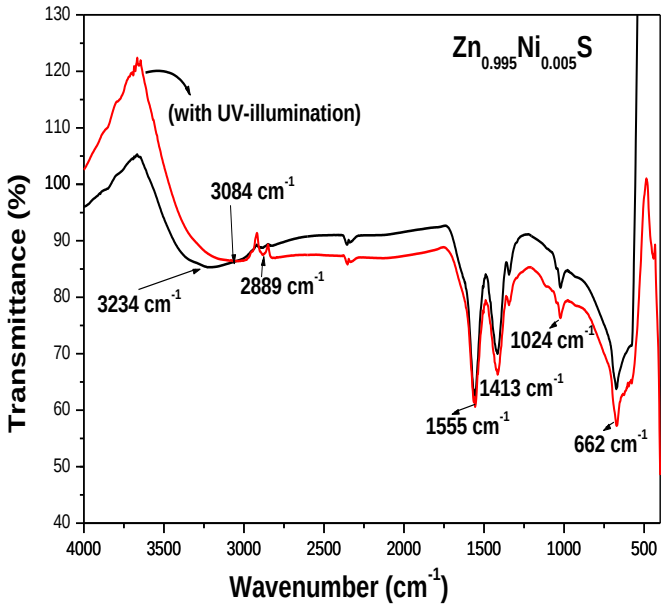

Figure 4.12: FTIR spectra of $Zn_{0.995}Ni_{0.005}S$ nanoparticles, with and without UV-irradiation

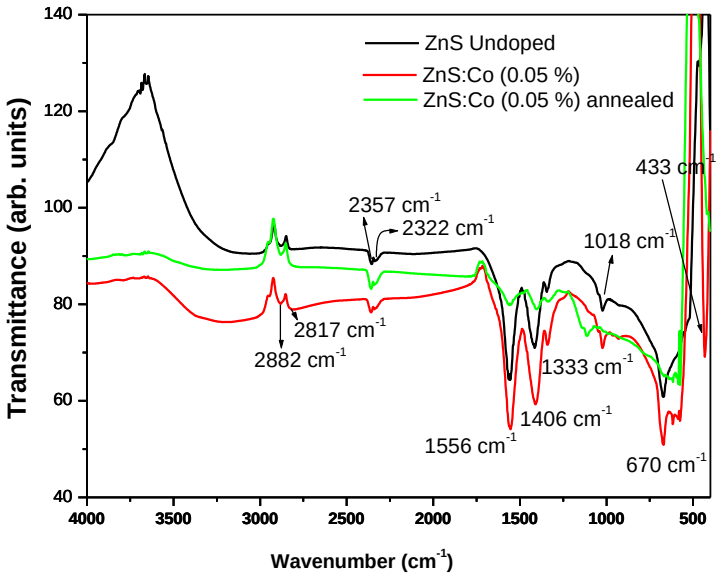

Figure 4.13: FTIR spectra of undoped Zns, and ZnS:Co (0.05 %) nanoparticles with and without annealing

broadened on annealing the nanoparticles at 200 ^{o}C for 2 hour in nitrogen gas atmosphere.

As explained above, for figure 4.11, the bands at 1405 cm^{-1} and 1558 cm^{-1} can be assigned to the symmetric and asymmetric stretching of COO- respectively [64]. This shows that the acetate group from the zinc acetate precursor used for zinc ions, have been retained in the synthesized nanoparticles.

Also, the moderate intensity band at 1015 cm^{-1} may be due to S-O-C stretching, and the weak S-S stretching vibration falls between 500-400 cm^{-1}. The weak peak appearing in both, the samples, at 666 and 670 cm^{-1} respectively might be due to the presence of C-S linkage. This shows the presence of mercaptoethanol ($HOCH_2CH_2SH$), which has been used as the surfactant/capping agent in the synthesis of the ZnS:Eu nanoparticles.

4.9 Absorbance Spectroscopy

Room temperature optical absorption study of the ZnS nanoparticles was performed by ultrasonically dispersing the samples in spectroscopic grade ethanol, and the optical absorbance was recorded by a spectrophotometer (Hitachi; U-3410). Figure 4.15 shows the optical absorption spectra of the undoped and Mn doped ZnS nanoparticles. The absorption coefficient (α) was determined from the absorbance versus wavelength (λ) traces recorded for the Mn-doped and undoped ZnS nanoparticles.

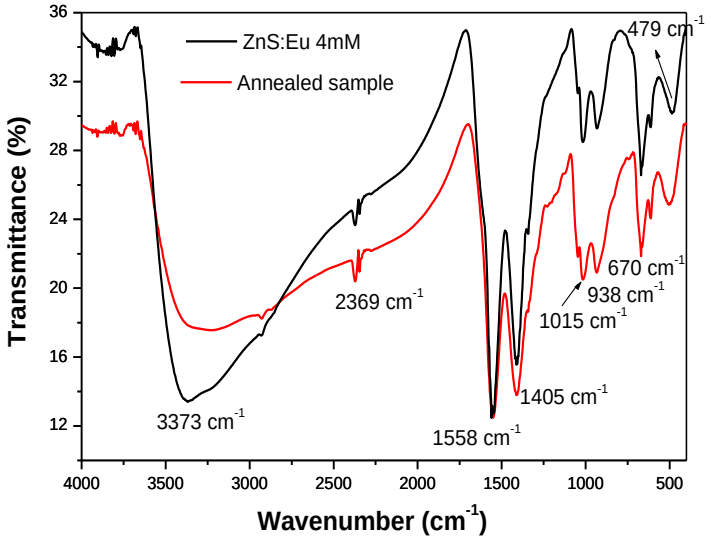

Figure 4.14: FTIR Spectrum of ZnS:Eu (4 mM) nanoparticles, with and without annealing

The optical band gap (E_g) in a semiconductor is determined by assuming the nature of transition (m) and plotting $(\alpha h\nu)^{1/m}$ versus $h\nu$, where m represents the nature of transition. Now, m may have different values, such as: 1/2, 2, 3/2 or 3 for respectively allowed direct, allowed indirect, forbidden direct and forbidden indirect transitions [24]. For allowed direct transition $(\alpha h\nu)^2$ versus $h\nu$ was plotted and the linear portion of it was extrapolated to $\alpha = 0$ value to obtain the corresponding band gap (E_g).

Also, the absorption coefficient, α, may be expressed as [22, 68]:

$$\alpha h\nu = A(h\nu - E_g)^m \tag{4.4}$$

$$d(ln(\alpha h\nu))/d(h\nu) = m/(h\nu - E_g) \tag{4.5}$$

Therefore, the plot of $d(ln(\alpha h\nu))/d(h\nu)$ versus $h\nu$ will show a discontinuity at $(h\nu - E_g)$.

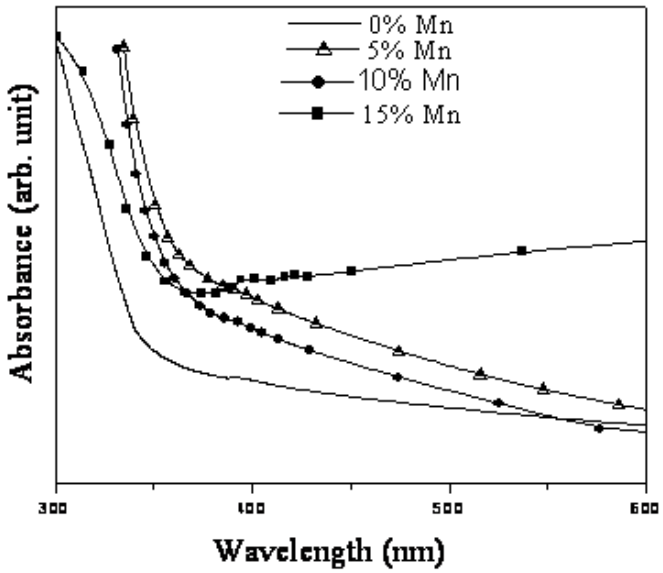

Figure 4.15: Plot of Absorbance versus Wavelength of ZnS: Mn nanoparticles

For undoped ZnS nanoparticles, the band gap has been calculated to be 3.88 eV, which indicates a blue shift as compared to the band gap of bulk ZnS (3.66 eV), indicating the quantum confinement in the ZnS nanocrystallites. It may also be noticed that the band gap values of Mn doped ZnS nanoparticles has reduced, which is due to the Mn related levels introduced in the host lattice. This can also be confirmed from the trap-depth values as obtained from the time resolved PL spectra discussed ahead.

Figure 14.17 shows the UV-visible absorption spectra of $Zn_{0.995}Ni_{0.005}S$ and $Zn_{0.97}Ni_{0.03}S$ nanoparticles, dispersed in spectroscopic grade ethanol, with and without UV-irradiation. The spectra have been recorded using Specord 205 spectrophotometer (Analytik Jena). The band gap energies have been calculated from the

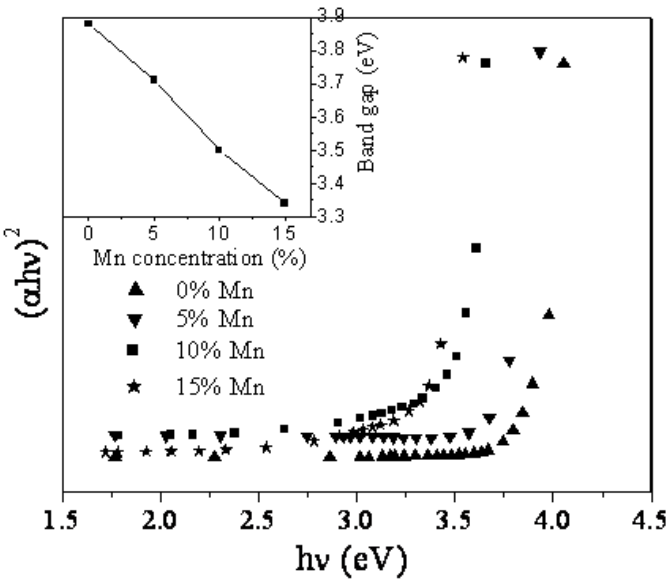

Figure 4.16: Plot of $(\alpha h\nu)^2$ versus $h\nu$ for the ZnS: Mn nanoparticles with inset showing the variation of band gap with Mn concentration

differential minima of the absorbance spectra [69], which comes out to be 4.01 and 4.10 eV for $Zn_{0.995}Ni_{0.005}S$ and $Zn_{0.97}Ni_{0.03}S$ nanoparticles, respectively; these values respectively have red-shifted to 3.90 and 4.02 eV, in case of prolonged UV-irradiated samples.

The optical absorbance of the synthesized ZnS:Cu samples has been measured and optical band gap (E_g), calculated. The corresponding plots of $(\alpha h\nu)^2$ versus hν, as a function of the copper concentration and on prolonged UV-irradiation have been shown in figure 4.18. No significant shift, on UV-irradiation, in the absorption edge, has been observed. This can also be observed from the band gap values, as shown in Table 4.3, that there is no remarkable difference between the band gap values before and after UV- irradiation. There is a slight increase in the band gap value of the ZnS:Cu nanoparticles (3.78 eV) from the bulk value (3.67 eV), which indicates the quantum size effects.

Table 4.2: Band Gap values of ZnS: Mn nanoparticles calculated from optical absorption spectra

S.No.	Sample	Band Gap (eV)
1	ZnS (Bulk)	3.66
2	ZnS: Mn (0%)	3.88
3	ZnS: Mn (5%)	3.71
4	ZnS: Mn (10%)	3.50
5	ZnS: Mn (15%)	3.34

Table 4.3: Band gap values of the ZnS:Cu nanoparticles with and without UV-irradiation

S. No.	Sample Name	Band Gap (eV)	
		Without UV-irradiation	With UV-irradiation
1.	ZnS:Cu (0.05%)	3.73	3.75
2.	ZnS:Cu (0.5%)	3.78	3.73
3.	ZnS:Cu (1%)	3.77	3.78

Figure 4.19 shows the UV-visible absorption spectra of ZnS:Co nanoparticles, with changing concentration of Co from 0.05 at. % to 10.0 %. There is an appreciable blue shift in the absorption edge in case of 3.0 % and 10.0 % Co doped samples.

Undoped and Eu-doped ZnS nanoparticles, finely dispersed in ethanol, have been

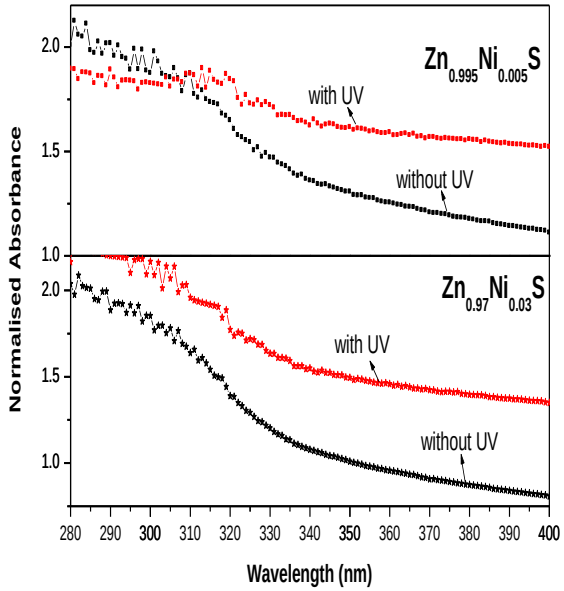

Figure 4.17: UV-visible absorption spectra of $Zn_{0.995}Ni_{0.005}S$ and $Zn_{0.97}Ni_{0.03}S$ nanoparticles with and without UV-irradiation

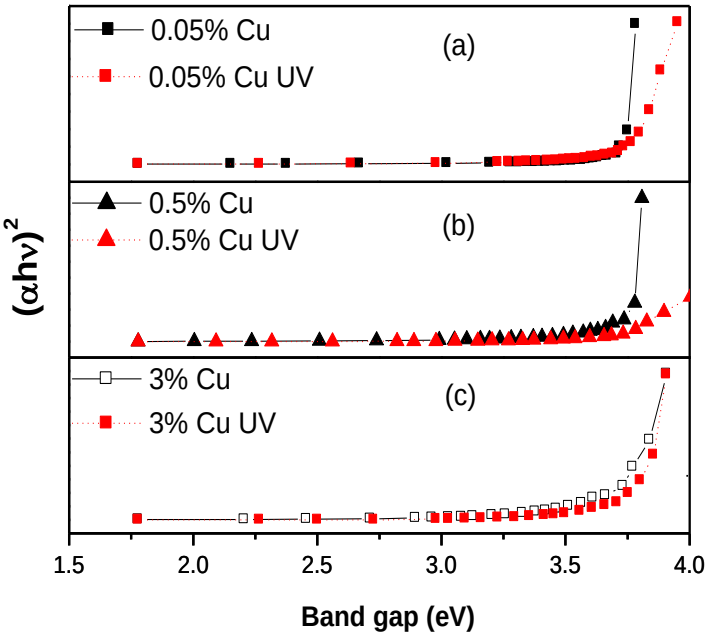

Figure 4.18: Plot of $(\alpha h\nu)^2$ versus hν for the ZnS:Cu nanoparticles with Cu concentrations (a) 0.05 % (b) 0.5 % (c) 3 %

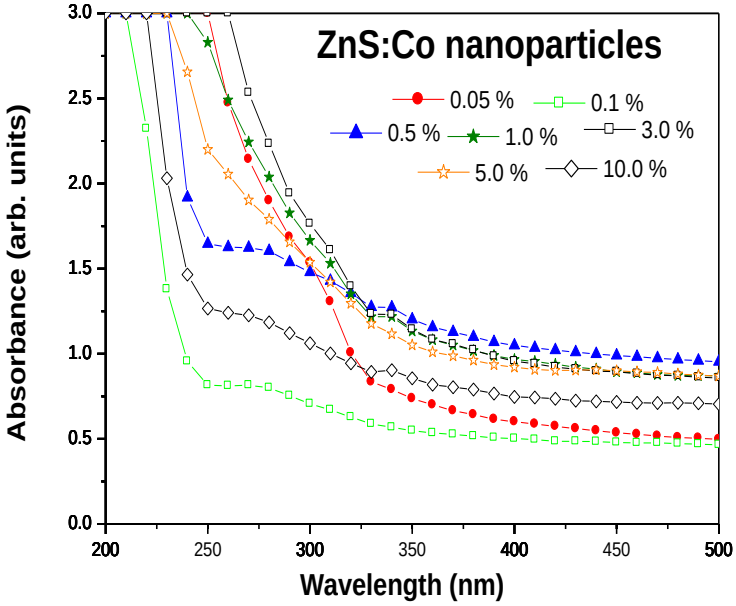

Figure 4.19: UV-visible absorption spectra of ZnS:Co nanoparticles, with varying concentration of Co

used for the UV- visible absorption studies by using Specord 205 spectrophotometer (Analytik Jena). Figures 4.20 to 4.24 show the UV-visible absorption spectra of the ZnS:Eu nanoparticles, with and without heat treatment. All the spectra show an absorption edge around 325 nm, with a slight red shift observed after the heat treatment of the samples. Moreover, the as-synthesized samples show the excitonic peak centered at around 315 nm. This is due to the quantum confinement effect. This excitonic peak fades away after annealing the nanoparticles.

Moreover, ZnS is a direct band gap semiconductor. Therefore, the optical band gap values have been calculated from the differential minima of the absorbance versus energy plots. Band gap of ZnS:Eu calculated by differential minima varies from 3.8 to 4.6, as shown in Table 4.4. This value has been found to be higher than that of the bulk ZnS, i.e., 3.67 eV. This enhancement in the optical band gap can be

attributed to the quantum confinement effects.

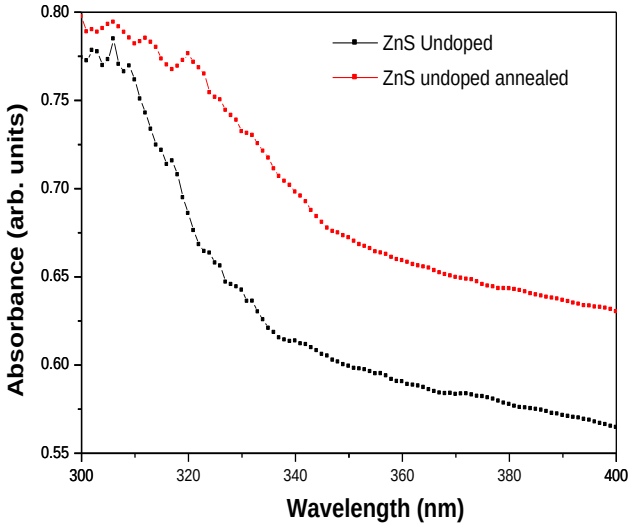

Figure 4.20: Absorbance versus wavelength graph of ZnS undoped with and without heat treatment

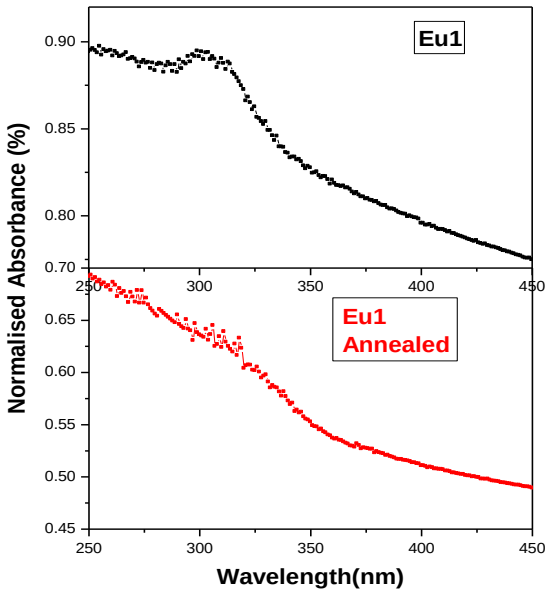

Figure 4.21: Absorbance versus wavelength graph of ZnS:Eu (1mM) with and without annealing

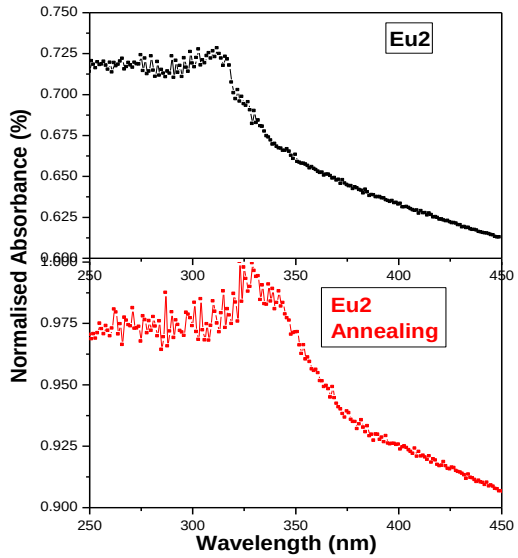

Figure 4.22: Absorbance versus wavelength graph of ZnS:Eu (2 mM) with and without annealing

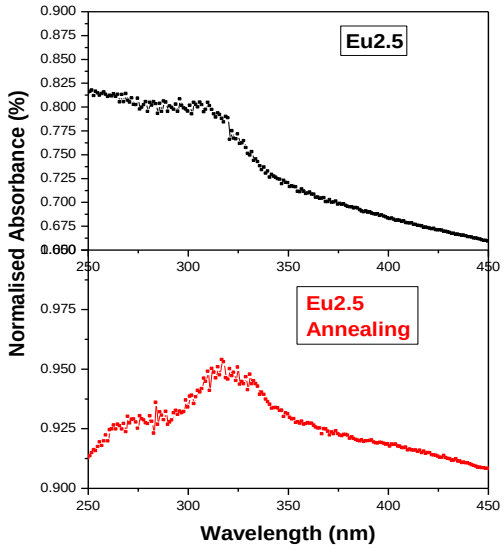

Figure 4.23: Absorbance versus wavelength graph of ZnS:Eu (2.5 mM) with and without annealing

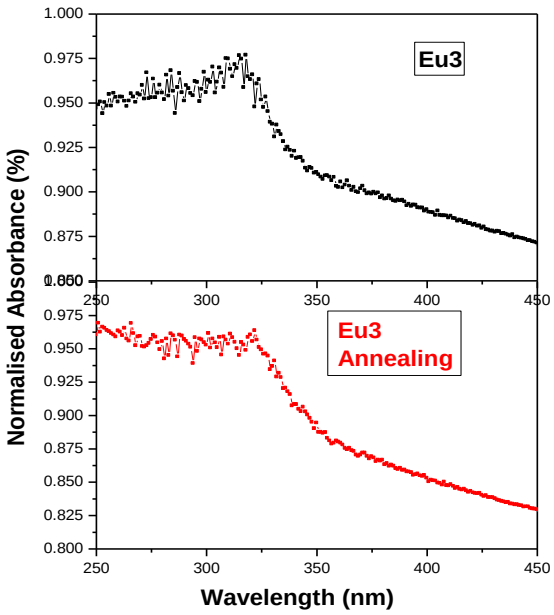

Figure 4.24: Absorbance versus wavelength graph of ZnS:Eu (3 mM) with and without annealing

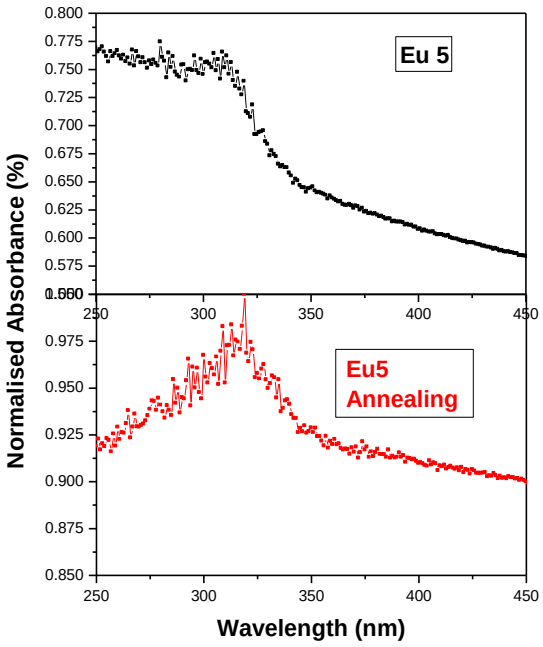

Figure 4.25: Absorbance versus wavelength graph of ZnS:Eu (5 mM) with and without annealing

Table 4.4: Band gaps of different ZnS:Eu nanoparticles

Sr. No.	**Sample Name**	**Band gap (eV)**
1	ZnS:Eu0	4.2
2	ZnS:Eu0 H	3.8
3	ZnS:Eu1	3.9
4	ZnS:Eu1 H	3.9
5	ZnS:Eu1.5	3.7
6	ZnS:Eu1.5 H	3.9
7	ZnS:Eu2	3.9
8	ZnS:Eu2 H	4.1
9	ZnS:Eu2.5	3.9
10	ZnS:Eu2.5 H	3.9
11	ZnS:Eu3	4.3
12	ZnS:Eu3 H	4.6
13	ZnS:Eu4	3.9
14	ZnS:Eu4 H	4.1
15	ZnS:Eu5	3.9
16	ZnS:Eu5 H	3.8

Chapter 5

Synthesis of CdS nanostructures by template synthesis

5.1 Template Synthesis Technique

Recently, one dimensional (1-D) nanostructures such as wires, rods, belts, and tubes have become the focus of intensive research owing to their unique applications in mesoscopic physics and fabrication of nanoscale devices [70–72].

The template synthesis is a simple and versatile method for preparing nanostructural materials (metals, semiconductors, polymers, metal-semiconductor junctions), which entails synthesizing the desired material within the pores of a template/membrane. The role of a template is two fold: (1) it allows reproduction of the structure with the best possible reproducibility, and (2) it is used to link the structure to the macroscopic word, i.e., the contacts. It is generally accepted that template-directed synthesis provides a simple, high-output, cost-effective procedure that also allows the complex topology present on the surface of a template to be

duplicated in a single step. Nearly any material, in principle, can be synthesized within the pores of the membrane, provided a suitable chemical pathway can be adopted. Typical concerns that require attention include the ability of the precursor solutions to 'wet' the pore, speed of the deposition reaction which may not be fast enough to block the pore opening, and stability of the membrane in the reaction conditions [73]. Various chemical strategies involved in the template synthesis of the nanostructures are (1) electrochemical deposition, (2) electroless deposition, (3) chemical polymerization, (4) sol-gel deposition, and (5) chemical vapour deposition. Electrochemical deposition is the electrolysis involving deposition of solid material on an electrode. It involves the oriented diffusion of positively charged growth species through the solution on applying the electric field and the reduction of the negatively charged growth species at the deposition surface, which also acts as an electrode. The electrochemical synthesis in templates has been taken as one of the most efficient methods in controlling the growth of micro/nano structures (heterogeneous-including multilayered, short, squat fibrils, long needle-like fibrils [74], tubules, tapered conical-single or double cones), because the growth is controllable almost exclusively in the direction normal to the surface [75, 76]. Moreover, the nanostructures obtained by this technique can be assembled into a variety of architectures [73]. Protruding, bristle-like crop of the fabricated nanostructures can be obtained on dissolving the membrane, or they can remain inside the pores of the membrane, or they can be freed from the membrane and can be collected as an ensemble of free nanostrutures. Semiconductor 1-D nanostructures have been extensively investigated worldwide, as they are the building blocks for fabricating functional nanoscale systems with a wide range of technological applications, in-

cluding nanoelectronics, photonics, nanocomputing, data processing, and biological and medical sensing [77–79]. Cadmium sulphide (CdS) is a typical direct band gap II-VI semiconductor having a bandgap of 2.42 eV at room temperature. This material is being widely investigated in semiconductor laser, x-ray detector, nonlinear optical devices, photovoltaic cells, display devices, thin film transistors, and also for tagging biological molecules [169]. Among the several experimental techniques that have been reported to fabricate the 1-D CdS nanostructures, template-mediated techniques have been demonstrated to be very effective [73, 81–94, 177]. Generally, these templates included soft templates, e.g. organic gelator [81], DNA [82], proteins [83] as well as the assemblies of surfactant [84] and hard templates, like: carbon nanotubes [85], porous membrane [73, 86–94, 96, 177], etc.

The 'trach-etch' polymeric membranes and porous alumina membranes have been much used by various researchers for the template synthesis of nano/micro materials. The commercially available trach-etch polymeric membranes, used for filtration, are prepared by bombarding nuclear fission fragments on the non-porous sheet to create damage cracks, which on further etching results into pores. Possin was the first to electrodeposit metallic nanowires in the diamond shaped pores of ion-track etched mica for superconducting studies of Sn nanowires in 1970 [97]. By the late 1980s and early 1990s Vetter and Spohr, Whitnetney et al. and Martin extended metallic electrodeposition to ion-trach etched plastic membranes [86, 98, 99].

Nuclepore polycarbonate membranes, as shown in figure 5.1, having pore size of 800-80 nm, pore density of 108 cm^{-2} and thickness 11 μm, have been used as templates for the synthesis of cadmium sulphide micro/nanostructures through electrochemical deposition. Figures 5.2 (a, b) show the SEM image of a polycarbonate

membrane of pore diameter, 100 and 50 nm, respectively, used as a template for the electrochemical deposition. All the pores are cylindrical and randomly scattered in the lamina of the polycarbonate membrane.

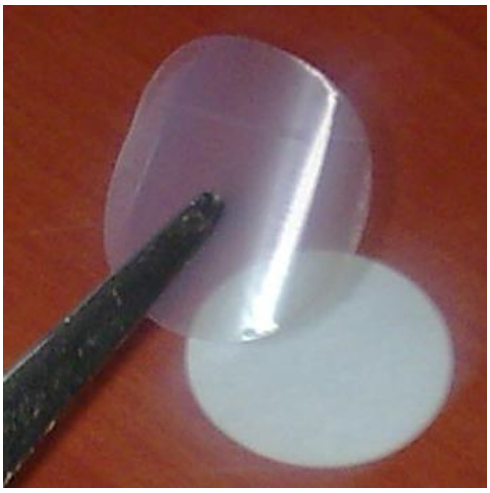

Figure 5.1: Image of the polycarbonate membrane used for electrochemical template synthesis

5.2 Electrochemical Cell

A simple but versatile electrochemical template synthesis cell has been used for the synthesis. Using this teflon-made cell, various parameters, like: temperature, exposed area of the template to the electrolyte, stirring rate, distance between anode and cathode have been controlled. Figure 5.3 shows the block diagram of the fabricated electrochemical template synthesis cell to carry out the dc electrochemical deposition using template synthesis technique.

The cell is fabricated using polytetrafluoroethene (teflon) which is a tough, wax-like, heat-resistant plastic (m.p. 327 ^{0}C). This cell consists of a hollow cylinder

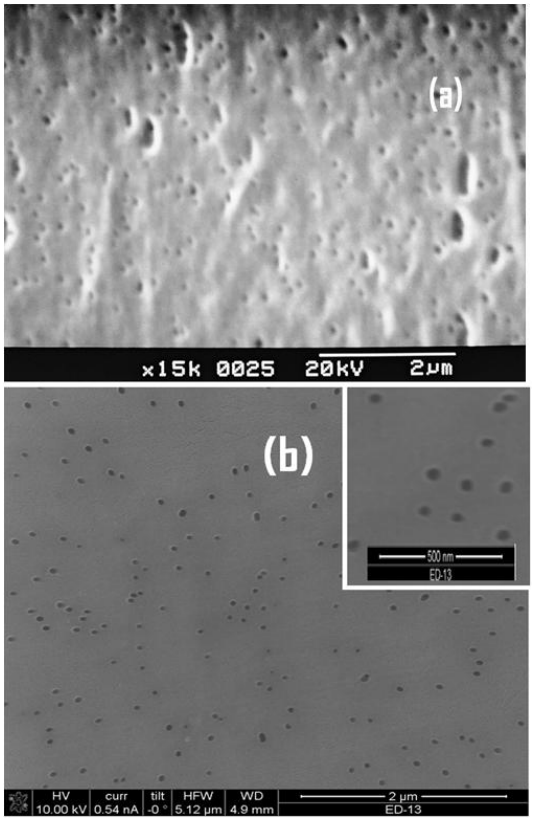

Figure 5.2: SEM image of the polycarbonate membrane having pore diameter (a) 100 nm and (b) 50nm

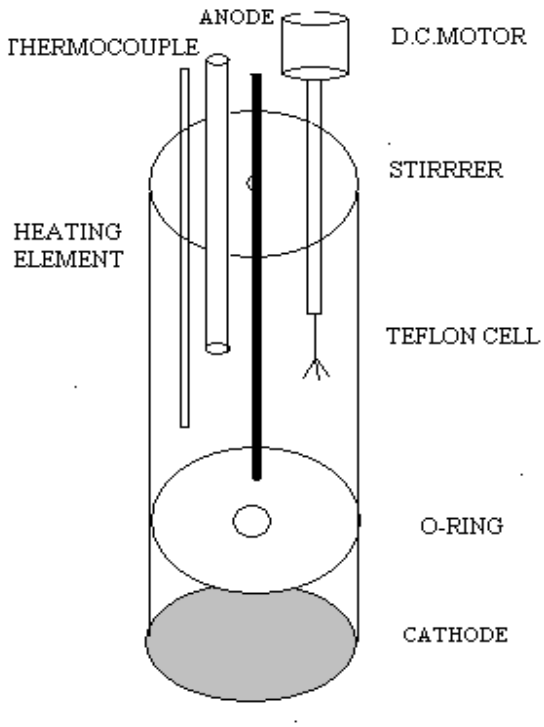

Figure 5.3: Schematic diagram of the electrochemical template synthesis cell

with inner diameter, 4.7 cm, open from both the ends. The O-ring is fitted at its lower end in a specially grooved teflon circle. A circular aluminium plate having diameter equal to that of the outer diameter of the teflon cylinder is taken. This plate can be tightened to the hollow teflon cylinder with screws so that it closes the lower end of vertical cylinder. This aluminium plate will work as cathode during electroplating process. The upper open end of the cylinder is covered with a teflon lid having four holes to suspend heating element, thermocouple, central electrode (anode) and stirrer. As the resistance of the cell depends upon interelectrode distance, the facility of changing inter electrode distance is provided, which will control the deposition quality. Even the facility of change of anode is provided as central electrode is not permanently fitted into the upper lid. As the circular teflon plate

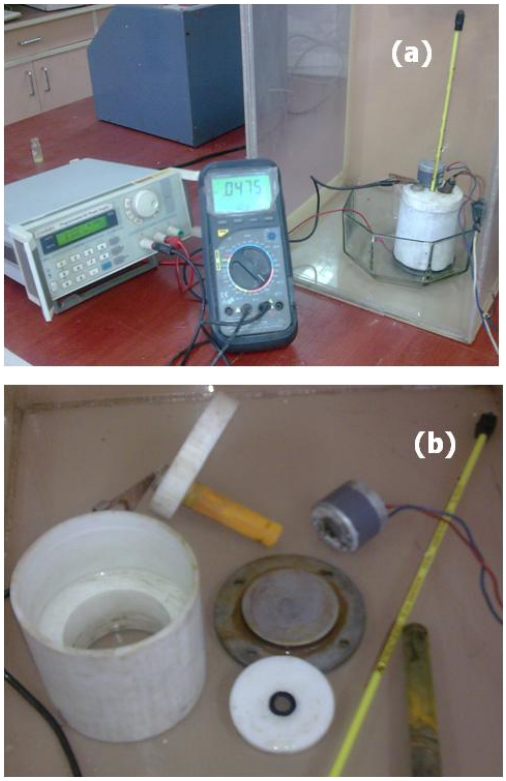

Figure 5.4: (a) Electrochemical template synthesis set-up (b) Various components of the electrochemical template synthesis cell

placed over porous membrane is detachable, therefore, various plates of same diameter and different O-ring diameters can be used, which will control the exposure area of the porous membrane, and will provide the facility of controlled yield.

The cell is placed in a special type of template fabrication chamber, which has been made using perspex sheets of dimensions 30 cm × 30 cm × 40.5 cm. An exhaust fan along with an outlet pipe is fitted to the chamber to provide the facility of outlet of the toxic gases produced in the process of electrochemical synthesis.

5.3 Preparation

The electrolyte solution consisted of 0.1539g/100ml $3CdSO_4.8H_2O$ (98 %) and 1.2604g/100ml Na_2SO_3 (99.9 %) in the double-distilled de-ionized water [100]. The pH of the electrolyte was adjusted in-between 1.65 and 1.80 using concentrated sulphuric acid. It was observed that the electrolyte once made should be used within 10-15 hour, as no desired electrochemical reaction occurs after its aging. It is advisable to prepare fresh electrolyte for every experiment.

The wetting of the membrane was done by dipping it in the electrolyte for a while. Proper wetting of the membrane was found to be an essential condition for the simultaneous growth of the structures in all the pores of the membrane [101]. In case of fabrication of microtubules, the membrane was dipped in 50 ml of 0.01M $SnCl_2$ solution, to which 4-5 drops of concentrated HCl had been added. This was done to activate the pore walls of the membrane so that, the deposition starts at the walls of the membrane. While adhering the membrane to the cathode (the copper tape), extra electrolyte was wiped off from the membrane. This is to prevent

the formation of a layer of electrolyte between the copper tape and the membrane, which will hinder the contact between the two. Subsequently, the membrane was fixed in the electrochemical cell with the pores exposed to the growth solution and the deposition reaction was carried out. The deposition process was performed at temperatures between 40^o and 45^o celsius. The applied voltage was kept low to avoid side reactions such as hydrogen evolution.

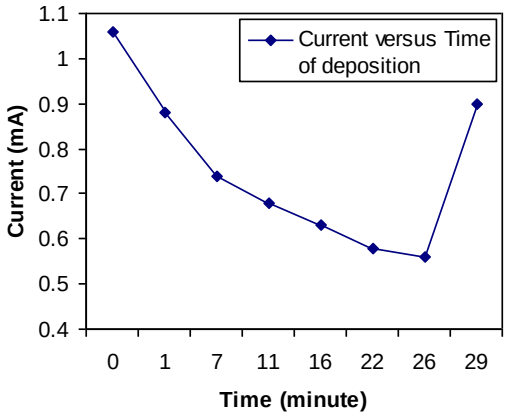

Figure 5.5: Current-time plot for the deposition of CdS inside the pores of the membrane

It was observed that the current decreased slowly throughout the pore filling process and after the deposition inside the pores is completed; it becomes nearly constant for a couple of minute and then increased. After the electrodeposition process the polymer membrane was dissolved in dichloromethane.

5.4 Growth Mechanism

CdS nanorods are synthesized in the pores of the polycarbonate membrane following the reaction between the Cd^{2+} ions and the S^{2-} ions. The initial process possibly

Table 5.1: Variations in different parameters and observations to obtain the optimized reaction conditions

S. No.	**pH**	**Temperature (celsius)**	**Voltage (V)**	**Time (minute)**	**Stirrer**	**Observation**
1.	1.71	25^o	5.4	50	Yes	Black colored over deposition
2.	1.71	25^o	1.1	30	Yes	Yellow colored solution
3.	2.45	32^o	4.2	30	No	Grey colored over deposition
4.	1.77	34^o	1.9	30	Yes	Yellow solution and deposition
5.	1.77	34^o	1.9	30	Yes (electrolyte aged by 1day)	No reaction
6.	1.62	31^o	1.2	30	Yes	Yellow solution and deposition
7.	1.70	32^o	0.9	30	No	Black deposition and yellow solution
8.	1.70	32^o	2.2	30	No (electrolyte aged for 1 day)	No reaction
9.	1.85	32^o	1.5	30	No	Black colored deposition and yellow solution
10.	1.77	34^o	5.5	20	Yes	Yellow solution and black deposition
11.	1.71	27^o	3.4	30	Yes	Black deposition
12.	1.90	15^o	3.0	30	Yes	Black deposition
13.	1.87	35^o - 40^o	2.8	20	Yes	Yellow deposition and solution
14.	1.87	35^o - 40^o	3.5	20	No	Black deposition
15.	1.67	35^o - 45^o	1.2	30	Yes	Yellow deposition and solution
16.	1.77	35^o - 45^o	1.2	30	Yes	Yellow deposition and solution (SEM image confirmed good deposition)

involves the conversion of SO_3^{2-} into $S_2O_3^{2-}$ ions. These thiosulphate ions act as the source of sulphur. When electric field (1.2 V) is applied between the cadmium anode and the conductive copper tape as the cathode, Cd^{2+} ions enter inside the pores of the membrane while moving towards the cathode. The S^{2-} ions enter the pores by the process of diffusion, leading to the formation of CdS molecules, which nucleate inside the pores of the membrane, thereby restricting the dimensions of the nanoforms to the shape and size of the pores.

The schematic diagram of pore filling process of a template/polycarbonate membrane and the type of the products formed has been shown in figure 5.6. The membrane is adhered to the adhesive copper tape (figure 5.6(a)), which acts as a cathode during the electrochemical deposition. The wetting of the pores is done using a drop of the electrolyte, which, in addition, also facilitates the membrane to adhere to the copper tape. Figure 5.6(b) shows the pores of the membrane filled with CdS. The free standing crop of the CdS nanorods is obtained after the dissolution of the membrane (figure 5.6(c)). Figure 5.6(d) shows the free nanorods/wires on a glass slide obtained on dissolving the peeled off membrane.

The pore walls of the membrane were activated using aged $SnCl_2$ solution, which initialized the pore filling starting from the pore wall inwards rather than starting from the bottom of the pore upwards (figure 5.7). This leads to the fabrication of the nanotubules rather than the nanorods.

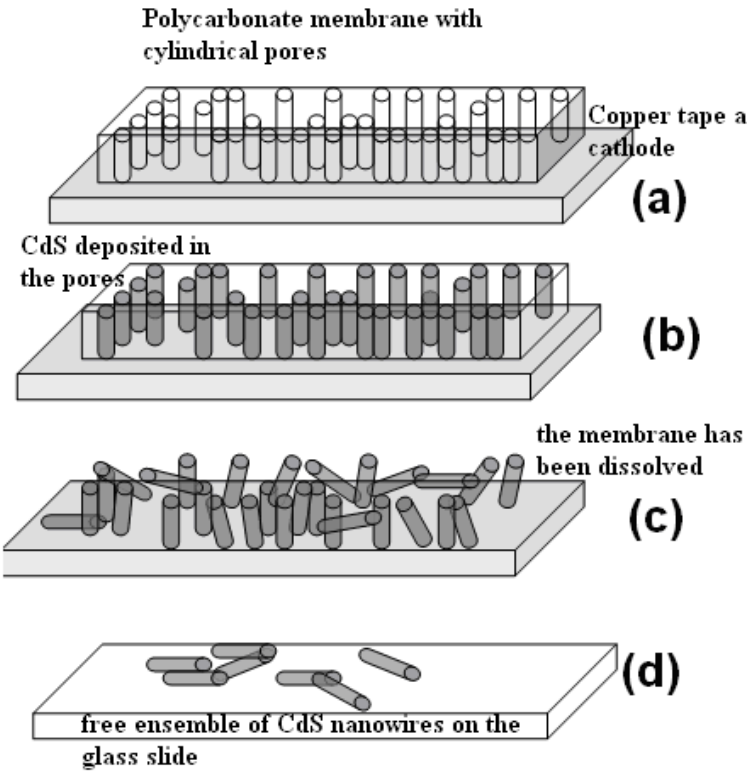

Figure 5.6: Schematic diagram of the pore filling process of a template/polycarbonate membrane

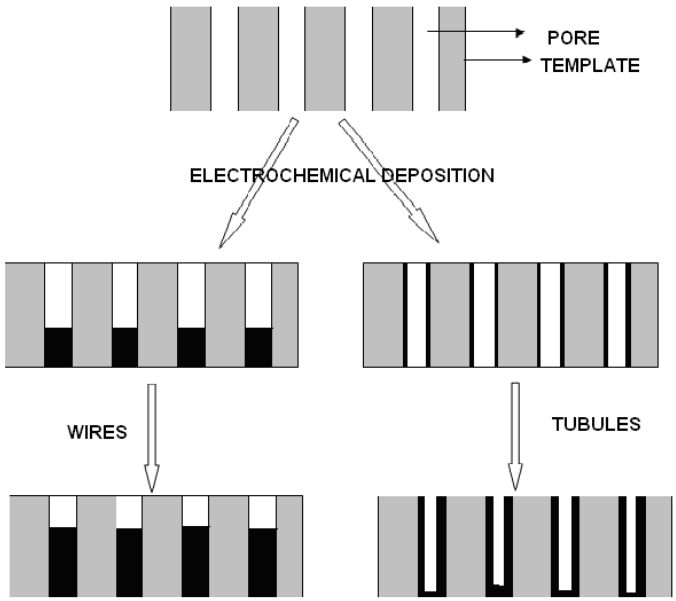

Figure 5.7: Schematic diagram of the pore filing processes in a template

5.5 Phase Detection

To structurally characterize the fabricated nano/microstructures, the polycarbonate membrane was pealed off from the adhesive copper strip, and was mounted over the sample holder of X-ray diffractometer.

Figures 5.8 and 5.9 show the X-ray diffraction patterns of CdS micro and nanostructures in 800 and 80 nm pore sized templates, respectively. Three distinct peaks appear in the spectra corresponding to the diffraction from (111), (220) and (311) planes of the CdS crystal according to the JCPDS data of the cubic phase of CdS (JSPDS card no. 10-454).

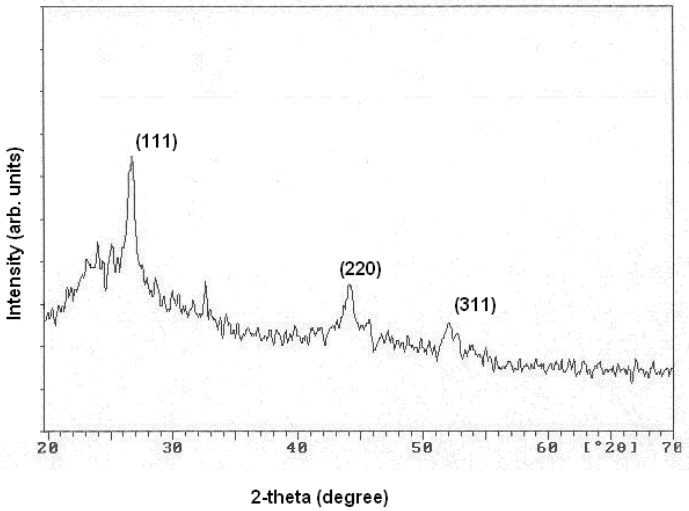

Figure 5.8: XRD spectrum of CdS microstructures in 800 nm pore diameter polycarbonate membrane

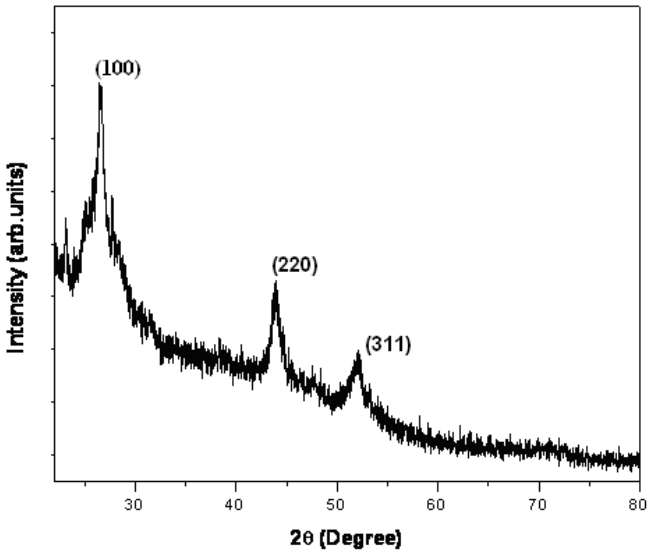

Figure 5.9: XRD spectrum of CdS nanostructures in 80 nm pore diameter polycarbonate membrane

5.6 Microstructural Analysis

For the microstructural studies, the polycarbonate membrane was dissolved to either give a crop of nanostructures on the copper substrate, used in the synthesis, or on the glass substrate to get the free ensemble of the nanostructures.

Figure 5.10 shows the SEM image of the bulk deposition of CdS, on the membrane. This has resulted from the unoptimised growth conditions such as longer time duration, high voltage supplied, pH value of the electrolyte, and temperature inside the electrochemical cell during the deposition. Stirring was also found to play an important role in the electrochemistry involved in synthesizing CdS electrochemically. In the absence of stirring, the color of the electrolyte did not change after the experiment and a grey colored layer of cadmium was deposited on the cathode instead of the yellow colored CdS (see table 5.1 for optimised conditions).

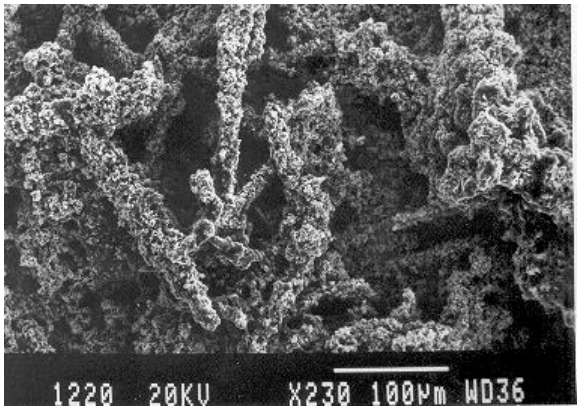

Figure 5.10: SEM image of the bulk deposition of CdS due to unoptimised reaction conditions

The unoptimised conditions have also led to some microstructures resembling the rectangular rods and a fan having six arms, with each arm grown in a symmetrical fashion depicting a regular hexagon (figure 5.11). The symmetrical structures might have been formed due to the etching of the membrane by the reaction conditions applied like high voltage and pH. These structures could have assembled in the fan like structures during the dissolution of the membrane.

Figures 5.12 (a, b) show the cauliflower morphology of the fabricated microstructures using 800 nm pore size template. After the template was removed, the embedded arrays of microwires having high aspect ratio, collapsed into an entangled mass due to the surface tension force exerted on the nanowires. Figure 5.12 (c) shows the uneven deposition due to improper wetting of the polycarbonate membrane. A full grown microwire, as shown in figure 5.12 (c), resulted from the proper adhesion of the membrane with the cathode strip, whereas the other microwires had just begun to grow, as the wetting in this region was not proper. Figure 5.12 (d) shows a crop

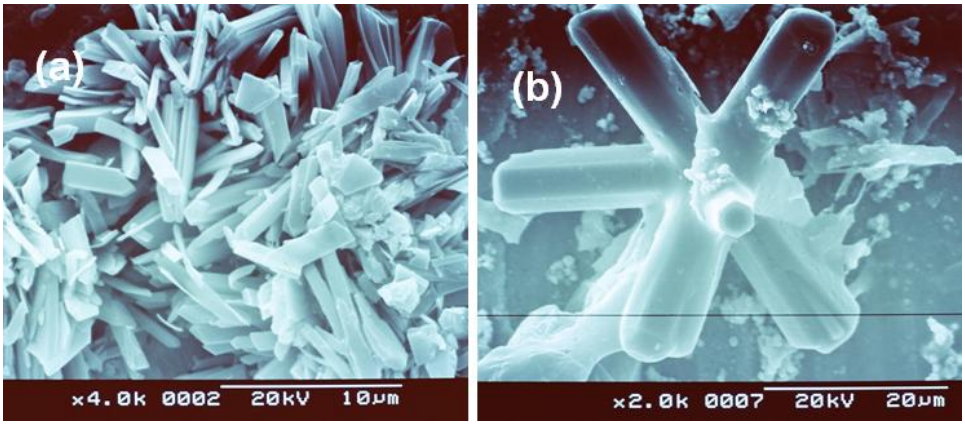

Figure 5.11: SEM images of CdS microstructures resembling (a) rectangular rods (b) a fan having six arms

of well separated microwires grown normal to the cathode and having high aspect ratio. The onset of the growth of microtubules having outer diameter 720 nm and thickness, varying between 125 nm and 185 nm, have been shown in figure 5.13. These were achieved by functionalizing the pore walls of polycarbonate with $SnCl_2$ solution, which enabled the onset of the tubule like growth inside the pores of the membrane during the electrochemical deposition.

Figure 5.14 (a) shows the SEM image of the CdS microrods standing on the copper tape, where the polycarbonate membrane of pore size 400 nm has not been completely dissolved. The uneven crop of the CdS microrods is due to the improper wetting of the membrane by the electrolyte. Moreover, some of the fabricated micro/nanostructures get destroyed or eroded away during the dissolution of the membrane. Figure 5.14 (b, c) show the SEM images of horizontally lying CdS nanorods obtained by dissolving the peeled off membrane (pore diameter 400 nm) on a glass slide. The microrods have good morphological quality and smooth walls; their length

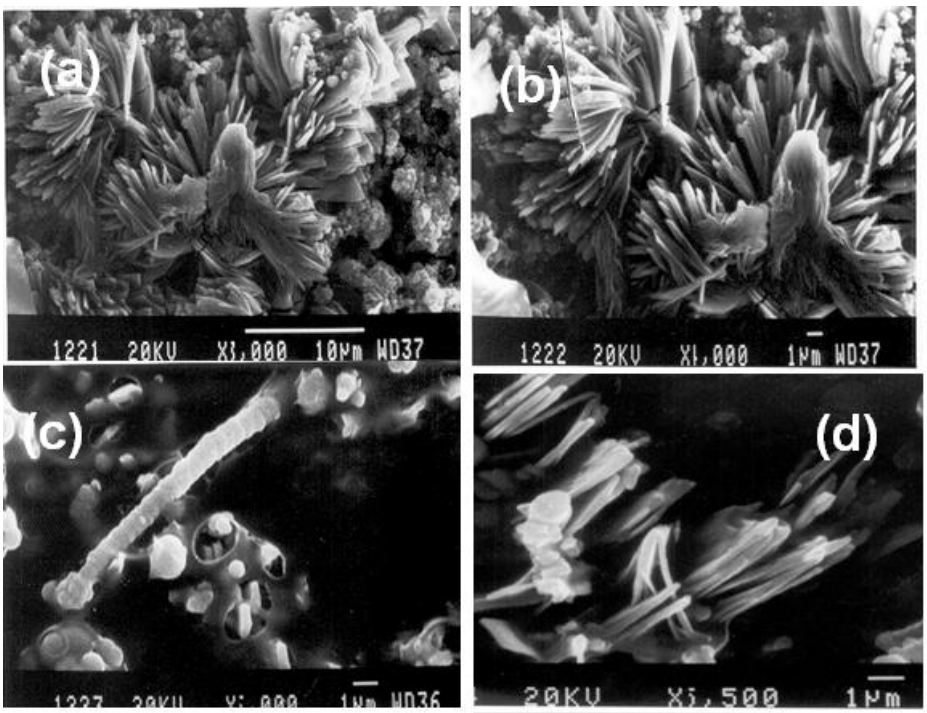

Figure 5.12: SEM images of CdS microstructures

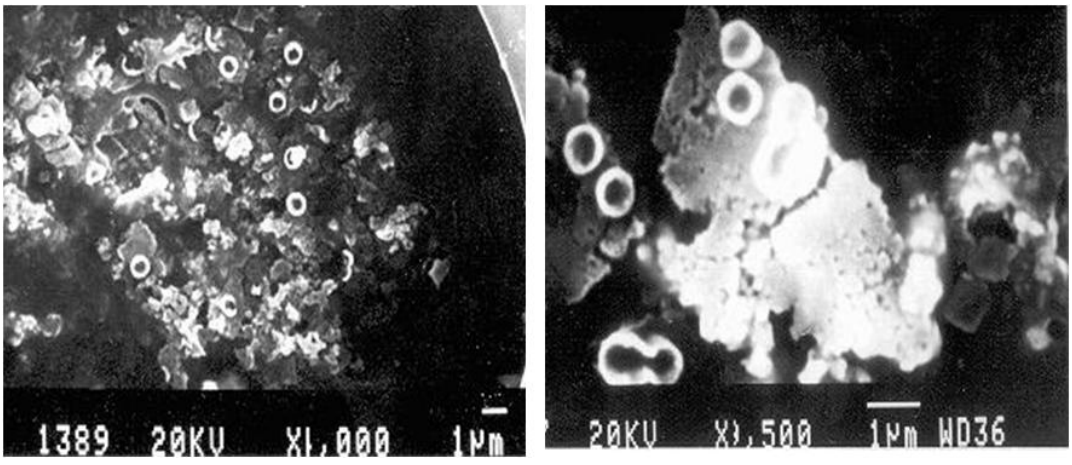

Figure 5.13: SEM images of CdS microtubules

varying from 3.0 to 10.8 μm, and diameter, from 313 to 390 nm. The variation in length of the microrods may be due to their breakage during the dissolution of the membrane or due to improper wetting of the pores of the membrane, which also results in delayed deposition of CdS in some of the pores. Figure 5.14 (d) shows the SEM image of the highly dense product of CdS nanowires having 100 nm diameter.

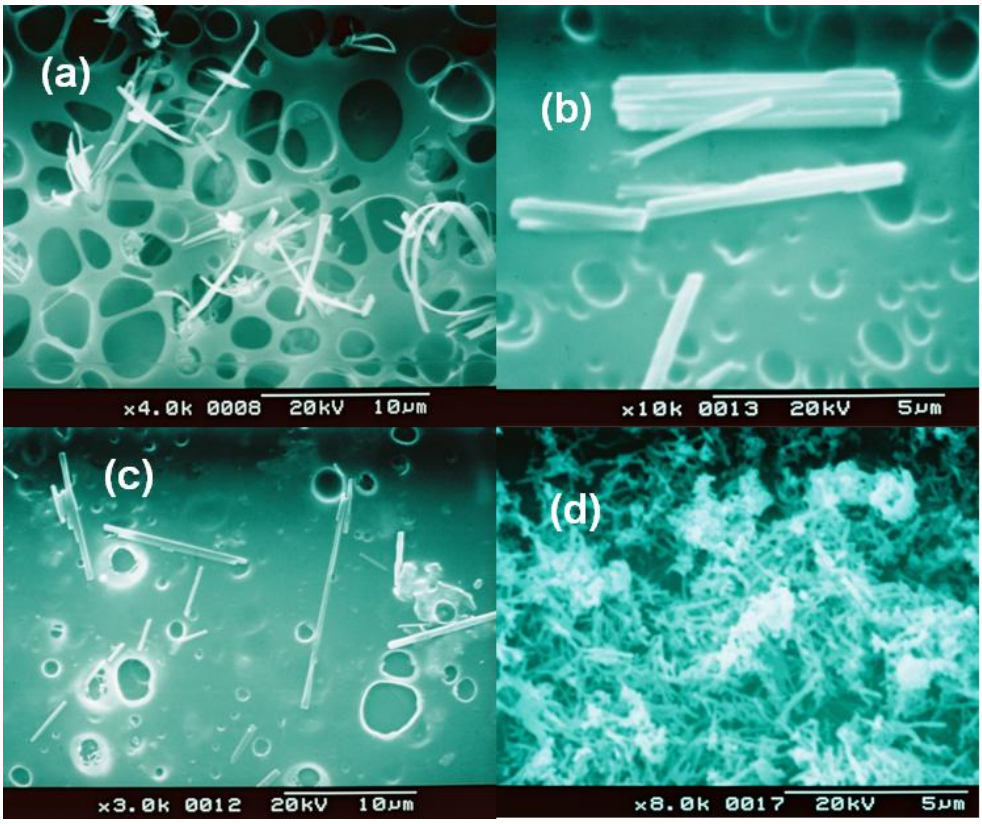

Figure 5.14: SEM images of CdS miro/nanostructures in different forms. (a) microrods in 400 nm pore size template where the template is not completely dissolved (b, c) CdS microrods on the glass slide (d) CdS nanowires fabricated in 100 nm pore size template

Figure 5.16 shows the CdS nanowires and nanoflowers fabricated using the 80 nm pore diameter polycarbonate membrane. Even here, the nanowires, having high aspect ratio, had formed entangled mass due to surface tension force exerted on

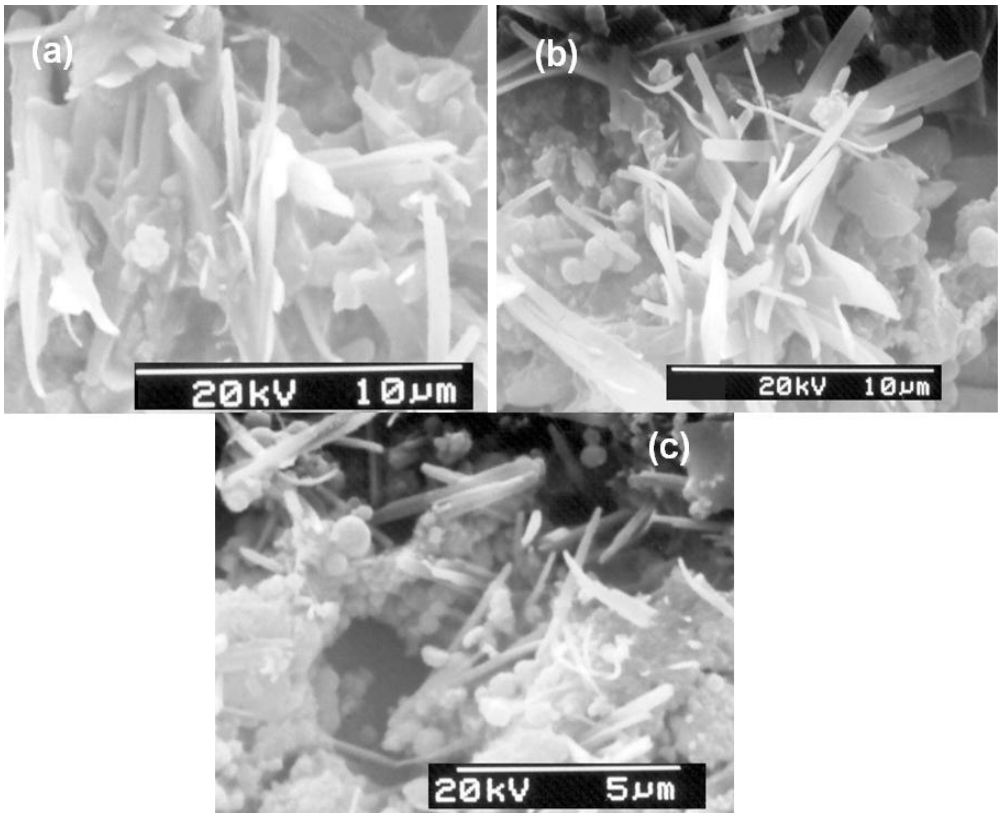

Figure 5.15: SEM images of the CdS nanorods haing diameter 100 nm

them. This may also be due to weak bonding of the base of CdS nanowires with the copper tape, acting as the cathode during the electrochemical deposition. It has been observed that the deposited semiconductor material, indeed, fills the pores uniformly, and the measured diameter of the CdS wires correspond closely to the pore diameter. No surfactant or capping agent had been used in the synthesis; however, the dimensions of the nanoforms were mechanically controlled using the templates of desired pore sizes.

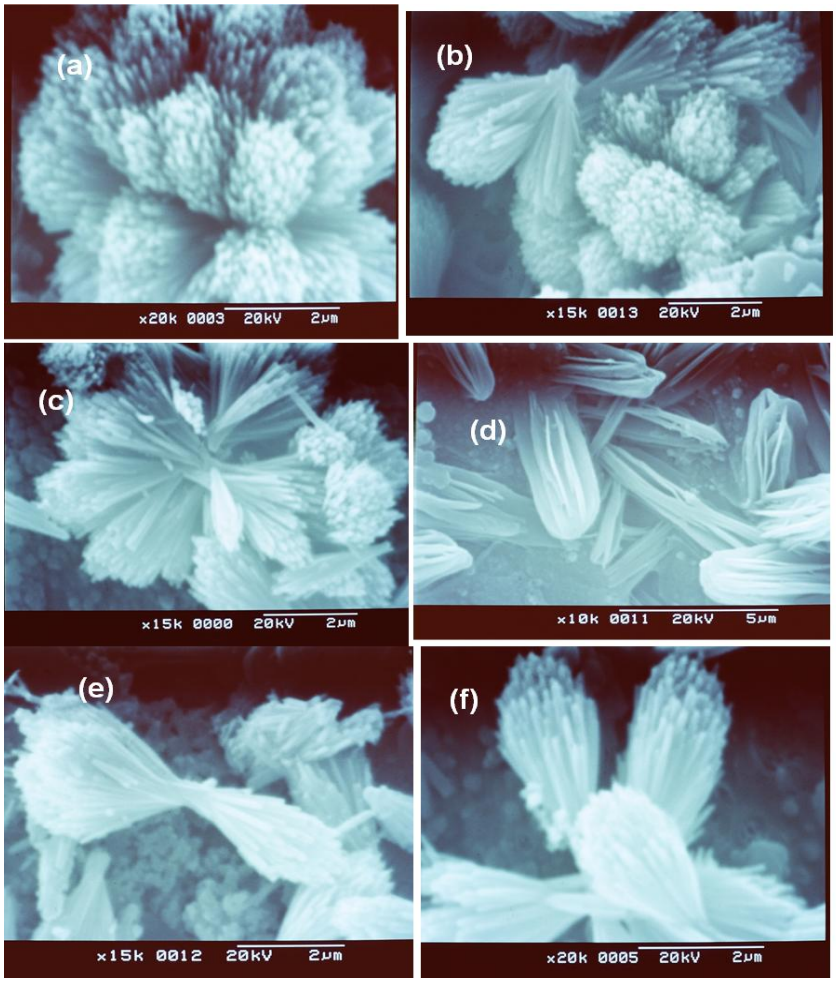

Figure 5.16: SEM images of the CdS nanorods haing diameter 100 nm

Thus, the results discussed above reveal that the electrochemical template synthesis technique can be efficiently used to fabricate the 1-D nanostructures of desired geometry.

5.7 Optical Absorbance

The optical absorbance of the fabricated CdS nanostructures was examined by dispersing the free ensembles of the micro/nanostructures in spectroscopic grade ethanol. Figure 5.17 and 5.18 show the UV-Visible absorption spectra of the CdS micro/nanorods of diameter 800 nm and 80 nm respectively. The fundamental absorption, which corresponds to the transition from the valence band to the conduction band, can be used to determine the band gap of material. The absorption coefficient (α) is determined from the absorbance versus wavelength (λ) traces recorded for the microstructures. The optical band gap (E_g) in a semiconductor is determined by assuming the nature of transition (m) and plotting $(\alpha h\nu)^{1/m}$ versus $h\nu$, where m represents the nature of transition. Here, m may have different values respectively 1/2, 2, 3/2 or 3 for allowed direct, allowed indirect, forbidden direct and forbidden indirect transitions [68]. For allowed direct transition $(\alpha h\nu)^2$ versus $h\nu$ has been plotted and the linear portion of it has been extrapolated to $\alpha = 0$ value to obtain the corresponding band gap ($E_g = 2.48$ eV) (inset of figure 5.17).

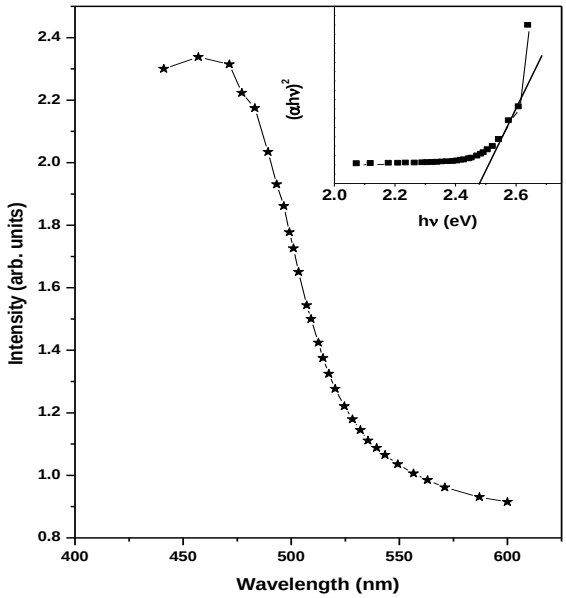

Figure 5.17: UV-Visible absorption spectra of CdS microrods having diameter 800 nm

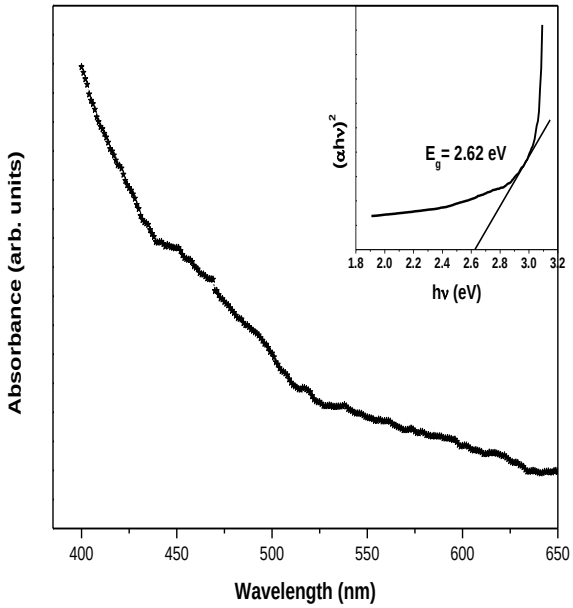

Figure 5.18: UV-Vis absorption spectra of CdS nanostructures fabricated in 80 nm pore size membranes

Chapter 6

Synthesis of CdS-based nanostructures by solvothermal route

6.1 Solvothermal Technique

In order to study and use the 1-D sulphides, much emphasis should be laid on their syntheses in terms of the crystal growth mechanism and kinetics at the nanoscale. Moreover, passive or active intervention in the crystallization of the 1-D nanoforms must be induced strategically and there must be an absolute control of the nanowire/ nanorod growth so that the diameter, length, growth direction, and morphology can be varied at atomic precision.

Solvothermal synthesis is a relatively mild method for the fabrication of sulphide nanorods and nanowires. It involves dissolving inorganic and/or organometallic precursors in a suitable solvent and conducting reactions in autoclaves, normally at

temperatures above the boiling point of the solvent, so that the autogenous pressure far exceeds the ambient pressure. This automatically raises the effective boiling point of the solvent. The solvent under pressure and temperature above its critical point is utilized to enhance the solubility of the solid reactants and speed up the reactions. In the typical procedure, the precursors and a solvent are placed in an autoclave, which is then placed at an elevated temperature and pressure to speed up the reaction to generate nanoforms. The major advantage of this approach is that most of the materials can be made soluble in a solvent by heating and pressurizing it close to its critical point. The solvent properties such as polarity, ability to donate or accept lone pair of electrons, softness, self-cohesiveness and viscosity will strongly influence the solubility and transport behavior of the ions involved in the heterogeneous liquid-solid reactions. The solvent polarity is generally used to describe the overall solvation ability of a solvent, which influences the interactions between the solvent and the solute molecules or ions [102].The products obtained by this approach are generally in the form of powder. However, substrates can be used to get film of nanostructures. Different solvents based on their properties are utilized to synthesize different nanoforms.

6.2 Backdrop

Due to wide range of practical applications, synthesis of CdS nanoforms, especially one-dimensional (1-D) nanoforms, such as: nanorods, nanowires, nanoribbons, have attracted immense research interest in the recent years [72]. Since many fundamental properties of semiconductor materials have been expressed as a function of

size and shape, controlling the size and shape of semiconductor nanocrystallites would provide opportunities for tailoring properties of materials and offer possibilities for observing interesting and useful physical phenomena [104]. Therefore, the engineering of materials in nanometer-scale has attracted much attention in optics, electronics, magnetics, catalysis, and ceramics [105]. The growth of 1-D nanostructures has been reported through many methods, such as electrochemistry [171], templates [107, 176] (mesoporous silica, carbon nanotubes, polycarbonate, alumina, etc.), emulsion or polymeric systems [108], arc discharge and laser-assisted catalytic growth [109], solution [110], and vapor transport methods [177]. Despite these exciting developments, a general synthetic strategy to grow nanowires is still significant to both nanotechnology and fundamental research. Moreover, these processes either require a high temperature of 400-900 ^{o}C, or have limitations in terms of sample uniformity, substrate choice, low product yield and commercial feasibility. However, solvothermal/hydrothermal methods have served as powerful tools for generalizing and systematizing controllable syntheses of nano-morphologies.

In 1980s, Rabenau [111] had defined hydrothermal synthesis as the use of water as a solvent, in a sealed chamber, when the reaction temperature was increased above 100 ^{o}C. This technique, when extended to the organic solvents, and the reaction temperature is made to exceed the boiling point of that solvent, is known as the solvothermal synthesis. Under these conditions, autogeneous pressure (i.e. self-developing and not externally applied) is developed. The pressure within the sealed reaction container is found to increase dramatically with temperature, but also will depend on other experimental factors, such as the percentage fill of the vessel and any dissolved salts [112]. In solvothermal technique, the starting materials/precursors

are exposed to special conditions, giving rise to unexpected reactions. These are accompanied with the formation of nanoscopic morphologies, which cannot be achieved by classical reactions [113]. Moreover, the nanoscopic morphologies can usually be controlled by varying the parameters in the reaction system, such as choices of solvents, capping agents/surfactants, organometallic and coordination, control of reaction temperature, change of pH value, etc. [114]. Yu et al. [104] has reported the effect of various solvents like, polyamines[ethylenediamine (En), diethylenetriamine (dien)], pyridine (py), ethanol (EtOH), ethylene gycol (EG), butane-1,4-diol (BUT), tetrahydrofuran (THF), and water (H_2O), on the morphology of the CdS nanoparticles synthesized using solvothermal technique.

Apart from the less complex 0-D, 1-D and 2-D nanostructures, branched nanostructures are known to offer a novel route for increasing structural complexity and endowing greater function. Branched nanocrystals, nanowires, and nanoribbon structures have been reported previously [115]. Yao et al. have reported complex CdS and CdSe nanostructures with flower-like, wire-like, and tree-like structures synthesized via a solvothermal method with use of a mixed solution made of diethylenetriamine (DETA) and deionized water (DIW) [116]. The photocatalytic activity of these complex nanostructures for degradation of acid fuchsine has been also investigated.

Dutta et al. have reported [69] the synthesis of size controlled CdS:Mn (0.05-0.09 mol.%) nanorods by the solvothermal technique, using pure ethylenediamine (En) and En/water solvent systems. They have observed that the diameter and length of the undoped nanorods were $\sim$ 35 nm and 1200-1400 nm. However, with the incorporation of Mn in CdS, both the diameter and the length of the nanorods

increased from 40 to 70 nm, and 1500 to 2500 nm, respectively. This effect might be due to the increase in solubility constant of the other salts, due to the organic ligand present in the Mn salt, which has facilitated the growth at higher doping concentration.

Moreover, rare-earth materials, like: samarium, europium, terbium, and erbium are known to be a source of effective luminescent centers when doped in II-VI chalcogenide semiconductors, because their excitation can occur by the recombination of photogenerated carriers confined in the semiconductor, and subsequent transfer of energy to these rare-earth ions [117]. Eu finds applications in the oxide form as a phosphor activator, europium-activated yttrium vanadate is used as the red phosphor in color TV tubes and Eu-doped plastic is known as a laser material.

Reisfeild et al. have reported the syntheses of the CdS particles in ZrO_2 films, together with Eu^{3+} and Tb^{3+} ions. They have studied the steady-state, as well as the time-resolved luminescence, which revealed that the intensity of emission of the rare earth ions is increased significantly in the presence of CdS particles [179]. Julian et al. and Hayakawa et al. have reported the enhancement of europium luminescence in Eu-doped SiO_2 materials by interaction with adsorbed CdS nanoparticles [119–121]. However, the effect of Eu doping on the optical properties of CdS nanorods has not been reported yet to the best of our knowledge.

The properties of nanomaterials can be tailored by passivating or functionalizing their surface with organic or inorganic materials. Encapsulation of the core nanostructures with a shell of desired material leads to a new class of materials, known as core/shell nanostructures, having modified optical, conductive and catalytic properties [122]. Owing to a variety of applications of these core/shell nanocomposi-

ties as compared to their individual single-component nanostructures, like in solar photovoltaic devices, chemical/biological sensors, light-emitting diodes, and optical switches [123–125, 127, 174]; it has led to the fabrication and study of the metal and semiconductor-based core/shell nanostructures. Many efforts have been made in the recent past to synthesize and characterize the semiconductor-based core/shell nanostructures, like: CdSe/ZnS, CdSe/CdS, ZnO/ZnS, TiO_2/CdS, CdS/SiO_2, CdS/ZnS, CdS/ZnS/SiO_2, etc. [128–132], but most of them are focused on nanoparticles. However, there are some reports on CdS/ZnS based 1-D nanorods as well [122, 133].

Thus, how to design and develop new solution-based methods to prepare novel CdS nanostructures and other similar semiconductors, is still one of the most important tasks.

6.3 Preparation of CdS nanostructures

The synthesis of CdS nanostructures has been carried out in a closed cylindrical teflon-lined stainless steel chamber as shown in figure 6.1. All of the chemical reagents used in this experiment were of analytical grade and used without further purification. Cadmium foils were used as a substrate and also as an additional source of cadmium. Pure and thin Cd foils were washed by distilled water and then cleaned by sonicating in acetone for 20 minute. However, the Cd foils were used as a substrate only when the vertical growth of CdS nanostructures was required.

Desired molar ratio of cadmium nitrate $[Cd(NO_3)_2.4H_2O]$ / cadmium acetate $[Cd(ac)_2.2H_2O]$ and/or Cd foils; and thiourea $[CSN_2H_4]$ were taken with 70ml of ethylenediamine (En) which acted as the solvent in the teflon chamber (capacity

100ml). To dope the CdS nanostructures with transition metal ions like Mn^{2+} and with rare-earth materials like Europium and Terbium, the respective salts were also added in the teflon-lined chamber, in desired concentrations.

Figure 6.1: Schematic and the pictorial view of the teflon-lined stainless steel chamber used in solvothermal synthesis

The properly sealed teflon-lined stainless chamber was maintained at a desired temperature and for desired time in an electric oven and afterwards, it was allowed to normally cool down to room temperature. The foil and the yellow colored precipitates were collected from the reaction vessel and were washed with de-ionized water and ethanol several times and subsequently dried in air at 50 ^oC for 6-12 hour.

With a view to study the effect of Cd source, reaction temperature, time, and the dopants, a series of experiments have been performed, as listed in Table 6.1.

6.4 Growth Mechanism

In case of solvothermal synthesis, temperature, time, and concentration play an important role in the formation of crystal structure, shape, and size of the nanoforms. The mechanism behind the formation of nanorods, in presence of ethylenediamine

Table 6.1: Summary of the experimental parameters varied in the solvothermal synthesis keeping En as the solvent

Sample No.	**Source(s) of Cd**	**Dopant**	**Temperature** (^oC)	**Time (hour)**	**Types of Nanostructures**
C1	Cd foil	—	80	12	Nanodics
C2	Cd foil	—	200	12	Cauliflowers and lamella
C3	Cd foil + cadmium nitrate	Undoped and Mn doped (5 and 10 mmol conc.)	120	24	Nanowires
C4	Cd foil	Undoped and Mn doped	140	24	Standing crop of nanorods
C5	Cadmium acetate	Undoped and Eu doped (1, 3, 5 at. %)	200	10	Nanorods
C6	Cadmium acetate	Undoped and Tb doped (1, 3, 5 at. %)	200	10	Nanorods
C7	Cadmium acetate	CdS and CdS/ZnS	160	6 + 6	Nanorods + Nanoslabs

(En) as chelating agent and solvent, has already been discussed by many researchers [134]. The ethylenediamine (En) molecules play the role of a director for the nanorod or nanowire growth. Reactions to form the CdS 1-D nanostructures can be formulated as follows:

$$Cd^{2+} + 2(En) \rightarrow [Cd(En)_2]^{2+} \tag{6.1}$$

$$[Cd(En)_2]^{2+} + S^{2-} \rightarrow CdS.0.5(En) \rightarrow CdS + En \tag{6.2}$$

En reacts with the Cd^{2+} ions to form Cd-En complex lamellar products, which react with the S^{2-} ions to produce CdS-En lamellar materials. These lamellae have many folds on them, which agglomerate together before breaking into needle like fragments. Finally, these needles grow to well-crystallized nanorods. The high temperature leads to the breakage of volatile amine groups giving rise to lamellar-to-rod transitions. This is known to proceed via the rolling mechanism [135].

6.5 Phase Detection by X-ray Diffraction (XRD)

The crystal structure of the CdS nanostructures prepared by solvothermal process was studied by XRD. According to the XRD pattern of the CdS nanowires (sample C3), as shown in figure 6.2, all the diffraction peaks correspond to the hexagonal wurtzite phase of CdS. These match well with those in the JCPDS (Joint Committee on Powder Diffraction Standards) Card no. 41-1049. No impurity peaks were detected, indicating high purity product. In addition, the intense and sharp diffraction peaks suggest that the obtained product is well crystallized. The d-spacing of

the CdS nanowires has been calculated using the XRD analysis and compared with the standard JCPDS data (Table 6.2). Both the data match well with each other. The corresponding (hkl) values are also illustrated in Table 6.2.

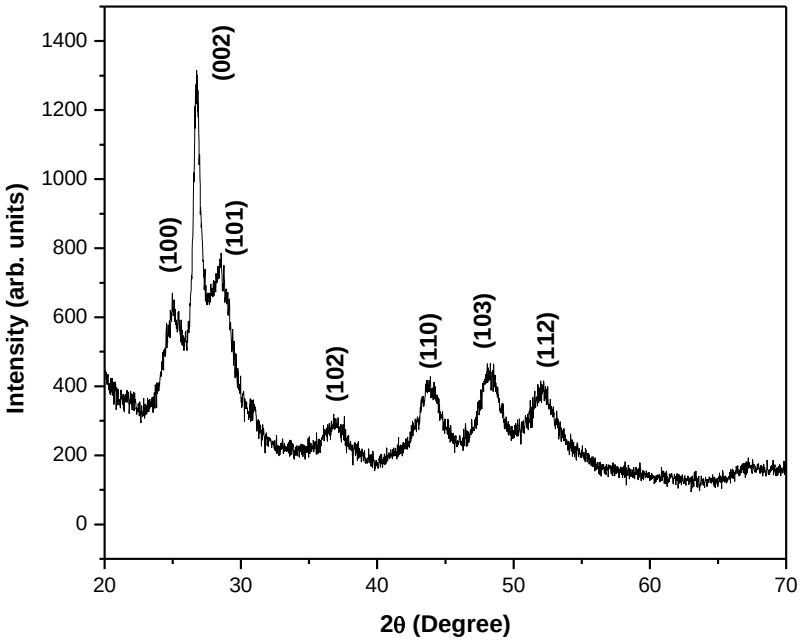

Figure 6.2: XRD pattern of CdS nanowires (sample C3) synthesized using solvothermal technique

The XRD pattern of the CdS undoped and Mn-doped nanorods, synthesized at 140 ^oC for 24 hour (sample C4) have been shown in figure 6.3. The diffraction peaks positioned at 2θ values of $25.09^o, 26.88^o, 28.46^o, 44.12^o, 48.12^o$, and 52.27^o can be indexed to the hexagonal wurtzite phase of CdS, whereas the peaks positioned at 2θ values of $32.18^o, 35.12^o, 38.76^o, 61.36^o$, and 62.52^o are due to the substrate (Cd foil). As shown in figure 6.3, on increase of Mn concentration, the relative intensity of the peak corresponding to (002) plane of CdS has been found to decrease appreciably. Also, there an overall decrease in the intensity of other peaks. This may be due to the decrease in the alignment of the nanorods on increase in concentration of Mn, as seen in the SEM images also (figure 6.13). The narrow FWHM (full width at half

Table 6.2: The comparison of d-values, obtained from XRD and JCPDS, and illustration of the corresponding (hkl) values

Peak	2θ ^{o}	$d_{XRD}(\AA)$	$d_{JCPDS}(\AA)$	**(hkl)**
1.	25.04	3.5561	3.5861	100
2.	26.78	3.3289	3.3599	002
3.	28.52	3.1296	3.1630	101
4.	37.07	2.4251	2.4519	102
5.	43.88	2.0632	2.0705	110
6.	48.08	1.8924	1.8998	103
7.	52.09	1.7557	1.7627	112

maximum) of the diffraction pattern indicates that the nanorods are of excellent crystal quality.

XRD pattern of CdS nanorods, undoped and doped with Eu, prepared by using Cadmium acetate as the source of Cd^{2+} ions (sample C5) has been shown in figure 6.4. The diffraction peaks can be indexed to the hexagonal wurtzite phase of CdS, having a good match with the JCPDS Card No. 41-1049. XRD data has also been used to quantify the preferred crystallographic orientation by texture analysis. The texture coefficients (TCs) of preferred orientation were determined by Harris formula [15]:

$$TC(h_ik_il_i) = [I(h_ik_il_i)/I_0(h_ik_il_i)][\frac{1}{n}\sum I(h_ik_il_i)/I_0(h_ik_il_i)]^{-1} \qquad (6.3)$$

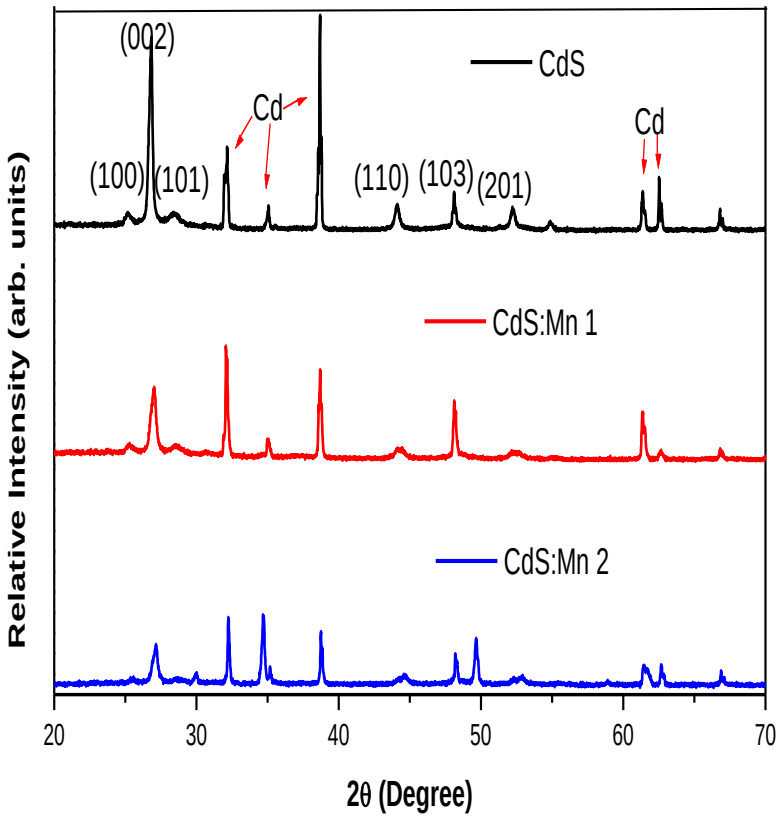

Figure 6.3: XRD pattern of CdS and CdS:Mn nanorods grown solvothermally at a temperature of 140 ^oC for 24 hour, using Cd foil as the substrate

where $TC(h_ik_il_i)$ is the texture coefficient,$I(h_ik_il_i)$ is the observed intensity and $I_0(h_ik_il_i)$ is the standard intensity of the $(h_ik_il_i)$ plane, and n is the reflection number. The value of texture coefficient indicates the maximum preferred orientation of the nanorods [16] along the corresponding diffraction plane. As shown in Table 6.3, the diffraction peaks centered at $2\theta = 26.59^o, 43.85^o$, and 52.00^o corresponding respectively to CdS planes (002), (110), and (112) have high texture coefficients as compared to those of other planes.

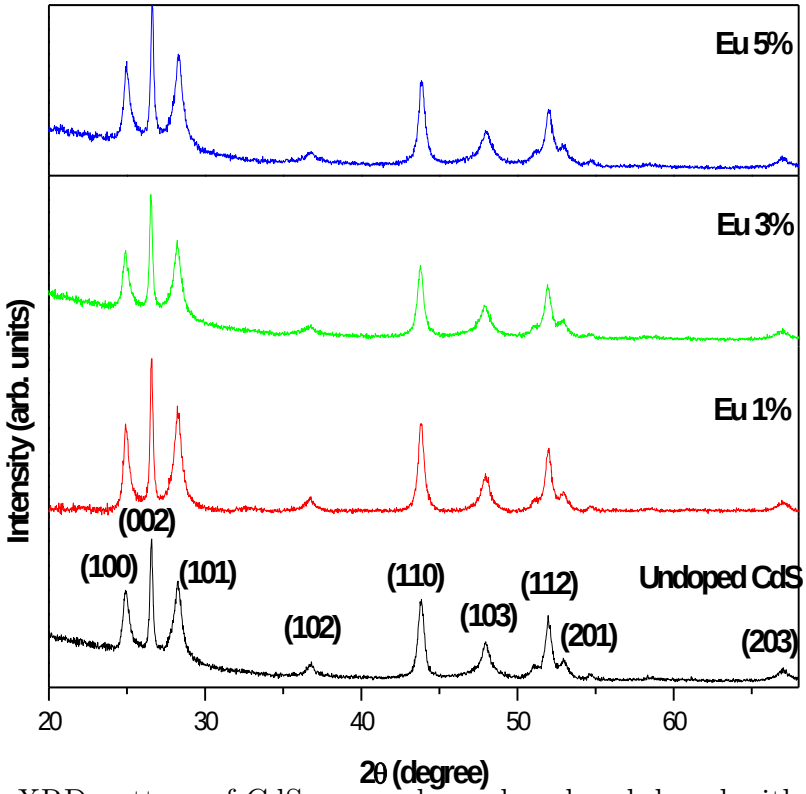

Figure 6.4: XRD pattern of CdS nanorods, undoped and doped with Eu (1.0, 3.0, 5.0 at.%), synthesized at 200 ^{o}C for 10 hour (sample C5)

Figure 6.5 shows the plot of the texture coefficients of the undoped and Eu^{3+} doped CdS nanorods as a function of the (hkl) planes. Addition of 1% Eu^{3+} dopant

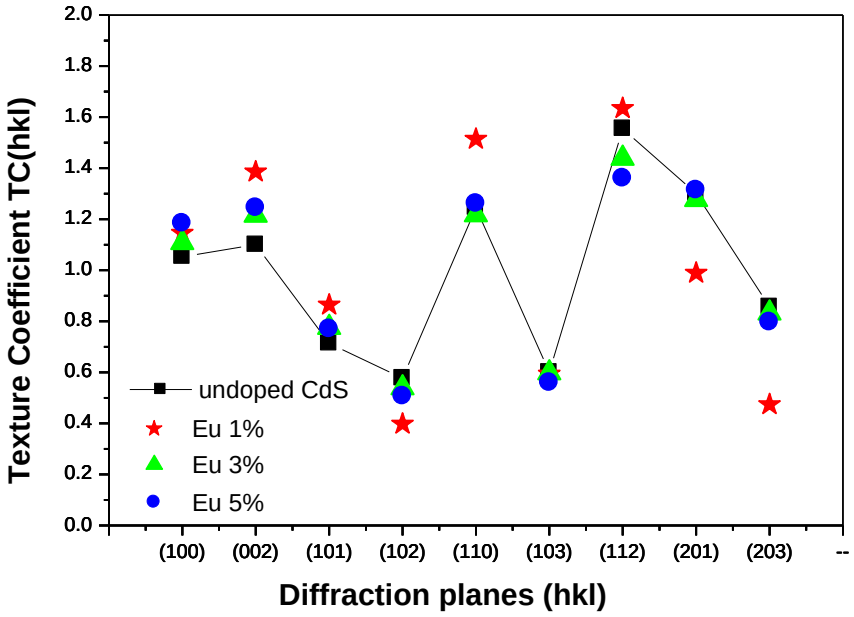

Figure 6.5: Plot of the texture coefficient of the undoped and Eu^{3+} - doped CdS nanorods as a function of (hkl) diffraction plane

to the CdS nanorods have increased the TC value corresponding to (002), (110), and (112) planes and have simultaneously decreased its value corresponding to (102), (201), and (203) planes. Whereas higher concentration of Eu^{3+} ions have not shown much change in the TC values as compared to the undoped CdS nanorods.

Figures 6.6 and 6.7 show the XRD pattern of CdS nanorods doped with terbium with atomic concentration of 0.1 % and 3.0 % respectively. The diffraction peaks are positioned at 2θ values of $24.83^o, 26.59^o, 28.33^o, 36.71^o, 43.77^o, 47.85^o, 50.98^o, 51.85^o$, and 52.87^o in case of Tb concentration, 0.1 at. %, and at 24.77 ^{o}, 26.53 ^{o}, 28.29 ^{o}, 36.77^o, 43.8^o, 47.82^o, 50.95 ^{o}, 51.82 ^{o}, and 52.93^o in case of Tb concentration, 3.0 at.%. These can be indexed to the wurtzite phase of CdS as compared to the JCPDS Card No. 41-1049. No dopant or impurity related peak has been observed. The effect of annealing at 200^o C for 2 hour in nitrogen gas atmosphere has also been

Table 6.3: Comparison of the texture coefficient of the CdS:Eu nanorods with the (hkl) planes

(h k l)	**Intensity**					**Texture Coefficient P(hkl)**			
	Standard (Io) (bulk CdS)	**Observed (I)**							
		Undoped CdS	Eu 1%	Eu 3%	Eu 5%	Undoped CdS	Eu 1%	Eu 3%	Eu 5%
100	62	65.03	56.11	61.88	64.29	1.0531	1.14563	1.10774	1.18401
002	91	99.69	99.64	99.62	99.23	1.09991	1.38608	1.21502	1.2451
101	100	71.08	68.3	69.91	67.51	0.71367	0.8646	0.77592	0.77085
102	29	16.66	9.11	14.08	12.87	0.5768	0.39766	0.53887	0.50674
110	48	59.54	57.41	52.63	53.03	1.24542	1.51406	1.21694	1.26149
103	50	29.87	23.46	26.93	24.52	0.59981	0.59396	0.59778	0.55996
112	31	48.00	40.03	40.17	36.95	1.55463	1.63463	1.4382	1.36099
201	15	19.42	11.72	17.26	17.26	1.29989	0.98908	1.27711	1.31387
203	15	12.80	5.62	11.25	10.47	0.85677	0.47429	0.83241	0.797

studied, which shows no appreciable change in the peak position and intensity of the diffraction peaks of the sample (sample C6). This proves that the fabricated CdS nanorods are quite stable in terms of their crystallanity even at higher temperatures.

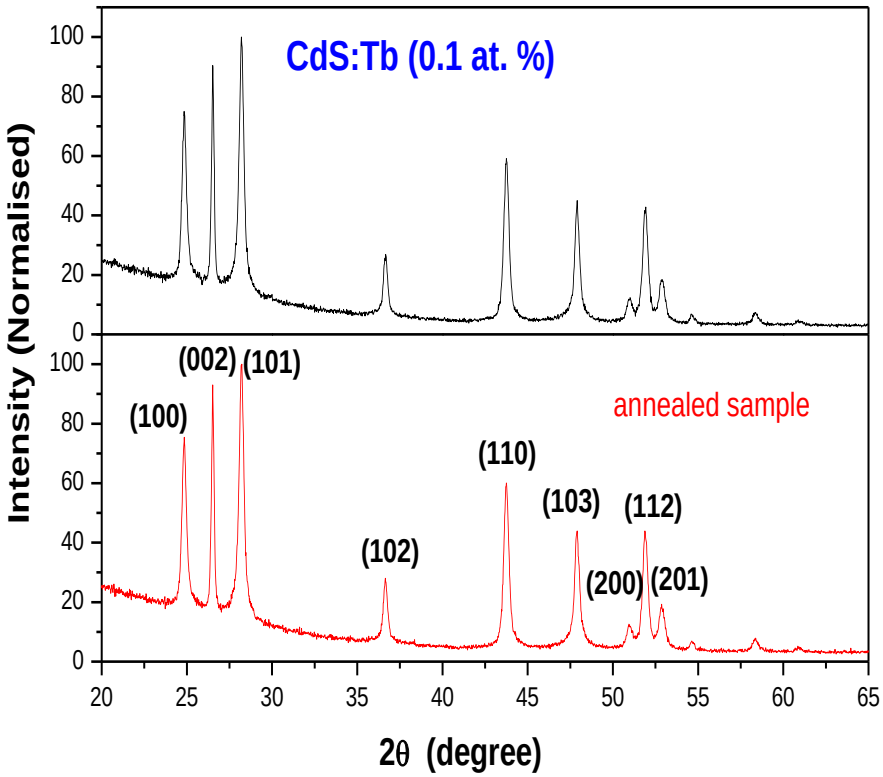

Figure 6.6: XRD pattern of CdS:Tb (0.1%) nanorods (sample C6), with and without annealing at 200 ^{o}C for 2 hour in nitrogen gas atmosphere

Figures 6.8 (a, b) show the XRD pattern of CdS and CdS/ZnS nanostructures synthesized using the solvothermal technique, in two steps. Figure 6.8 (a) shows the XRD pattern of the CdS core, synthesized in the first step of the solvothermal process. The diffraction peaks positioned at 2θ values of $25.1^o, 26.8^o, 28.5^o, 36.9^o, 44.0^o, 48.2^o$, and 52.1^o match well with the respective, (100), (002), (101), (102), (110), (103), and (112) crystal planes of the hexagonal wurtzite phase of CdS, according to the standard JCPDS data card no. 41-1049. XRD pat-

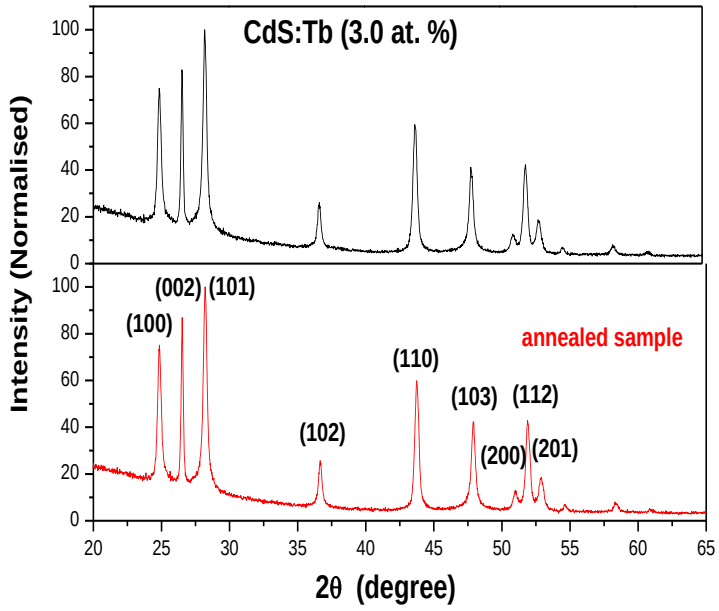

Figure 6.7: XRD pattern of CdS:Tb (3.0 %) nanorods (sample C6), with and without annealing

tern of the CdS/ZnS nanostructures, synthesized in the second step of the solvothermal process, shows the diffraction peaks due to the hexagonal wurtzite crystalline phases of both CdS and ZnS. In case of the CdS/ZnS nanostructures, the diffraction peaks due to the presence of CdS are in coherence with that of the CdS core, as shown in figures 6.8 (a, b). Whereas, the peaks positioned at 2θ values of $27.8^o, 29.3^o, 31.5^o, 41.7^o, 47.6^o$, and 49.0^o, match well with the respective, (100), (002), (101), (102), (110), and (103) crystal planes of hexagonal wurtzite-2H phase of ZnS, according to the JCPDS data card no. 36-1450. On comparing the CdS diffraction peaks in figures 6.8 (a) and 6.8 (b), it is found that the preferential orientation of the CdS nanorods is along the (002) plane, as its intensity is highest, however, in the case of CdS/ZnS nanostructures, the intensity of the peak corresponding to (100) has become comparable to that of (002), showing the change in the preferred crystallographic orientation. Apart from this, there are some diffrac-

tion peaks at 2θ values of $10.2^o, 17.2^o, 20.6^o, 22.4^o, 33.1^o, 34.2^o, 53.1^o$, and 53.5^o, which are due to the presence of CdS/ZnS-En complexes [136, 137]. In the reaction mechanism, ethylendiamine (En) has two NH groups to chelate, with the Cd^{2+} and Zn^{2+} ions. Moreover, En is known to have a relatively weak intermolecular coordination interaction, which allows it (En) to act as a molecular template for the growth of the CdS; ZnS and CdS/ZnS nanostructures, offering a less rigid confinement for the crystal growth [138]. Therefore, the preferred growth direction of the crystal can change easily.

The reactions following the CdS and CdS/ZnS nanostructures, using the solvothermal technique in two steps, with En as the solvent, can be formulated as follows:

Step I

Refer equations 6.1 and 6.2.

These reactions have been supported by many researchers [137, 139]. However, as seen from the FTIR spectra, figure 6.26, there is a presence of En in the product, showing incomplete transfer of CdS. 0.5 (En) molecules to CdS and En.

Step II

$$Zn^{2+} + 2(En) \rightarrow [Zn(En)_2]^{2+} \tag{6.4}$$

$$[Zn(En)_2]^{2+} + S^{2-} \rightarrow ZnS.0.5(En) \rightarrow ZnS + En \tag{6.5}$$

$$CdS + En + ZnS \rightarrow [CdS - En - ZnS] \tag{6.6}$$

En molecules interact with Cd and Zn ions to form Cd-En and Zn-En complexes, which react with S ions to give CdS-En and ZnS-En complexes. Due to high temperature and pressure, these complexes break up into the CdS or ZnS crystal structures along with En molecules, according to the equations 6.2 and 6.5. However, there is a possibility of the formation of CdS-En-ZnS complexes (equation 6.6), in the second step of the solvothermal technique used to synthesize CdS/ZnS nanostructures. This can be justified from the XRD pattern as shown in figure 6.8 (b), as there are CdS/ZnS-En related diffraction peaks. However, no CdS-En related crystal diffraction peak has been observed from figure 6.8 (a).

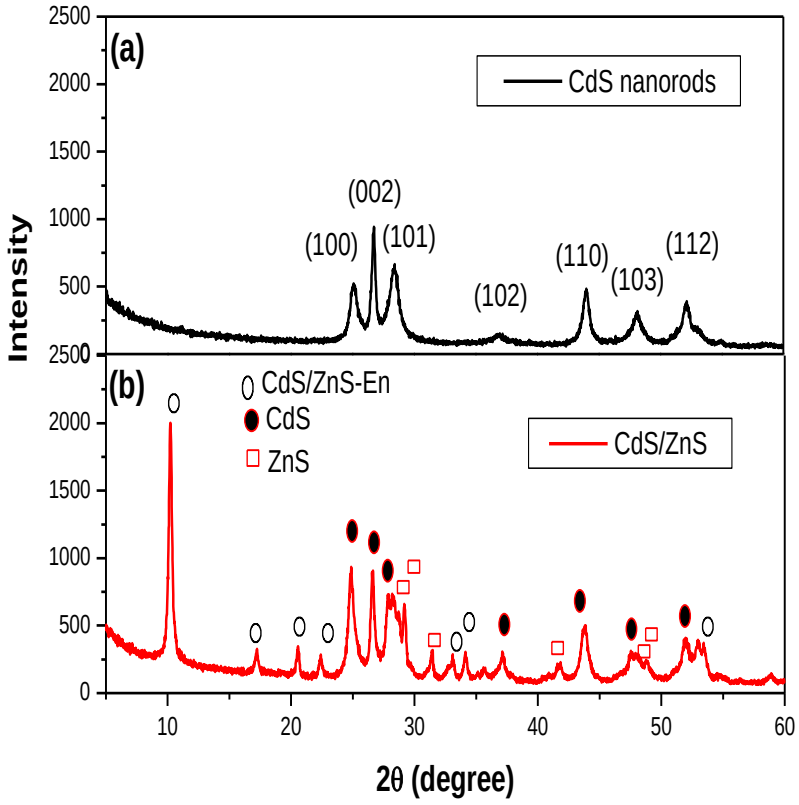

Figure 6.8: XRD patterns of CdS nanorods and CdS/ZnS core/shell nanostructures (sample C7)

6.6 Microstructural Analysis

The CdS-based nanostructures have been synthesized either in the powder form or as a crop on the Cd foils, as the substrate. For the microstructural analysis, these Cd foils/ the powdered samples were directly transferred to the SEM stubs for the specimen preparation. A thin layer of gold/palladium was deposited on the specimens so as to make them conductive for the SEM analysis. Figures 6.9 (a) and (b) show the SEM images of CdS nanodiscs having diameter, 1.9 μm, and thickness, 95 nm. These CdS nanodiscs have been synthesized solvothermally at 80 ^oC for 12 hour. On further increasing the temperature of the oven to 200 ^oC but maintaining the reaction time of 12 hour, the nanodiscs, as synthesized at 80 ^oC, have merged together to give a cauliflower-like morphology, as shown in figures 6.10 (a) and (b). These flower-like nanostructures, which have a large specific area on the surface, may provide a good reaction catalyst ability or increase the interface area in optoelectronic devices. Moreover, as explained in the growth mechanism, the lamellar to needle-like transition has also set in at 200 ^oC, as shown in figure 6.10 (c).

However, enhancement in the reaction time to 24 hour, maintaining the temperature in the oven at 120 ^{o}C, has led to wire-like formation as shown in figure 6.11 (a). Figures 6.11 (a, b), (c) and (d) show the SEM images of undoped, 5 mmol, and 10 mmol Mn doped CdS nanostructures respectively. Figures 6.11 (a, b) show the growth of highly dense CdS nanowires having diameters between 9 and 40 nm and lengths varying from 0.5 to 2 μm. The ends of the nanowires are still attached to adjacent nanoforms, possibly due to the incomplete transformation of the lamellae to the nanowires. Whereas, on doping with Mn, and on increasing the concentration of

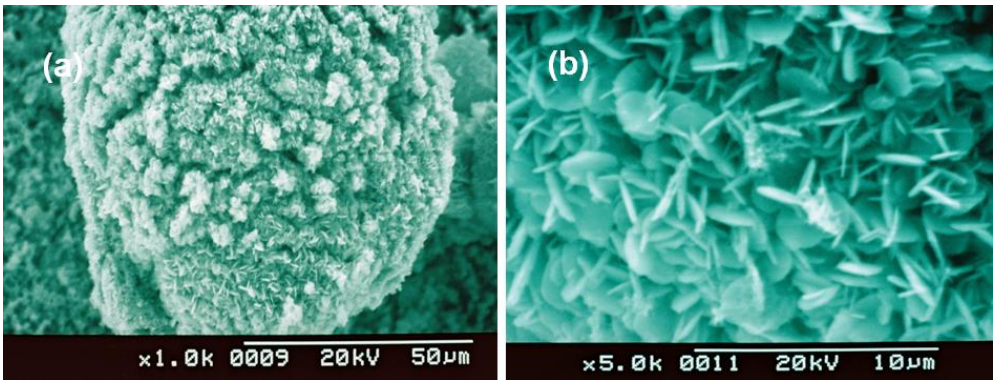

Figure 6.9: SEM images of nanodiscs (sample C1)

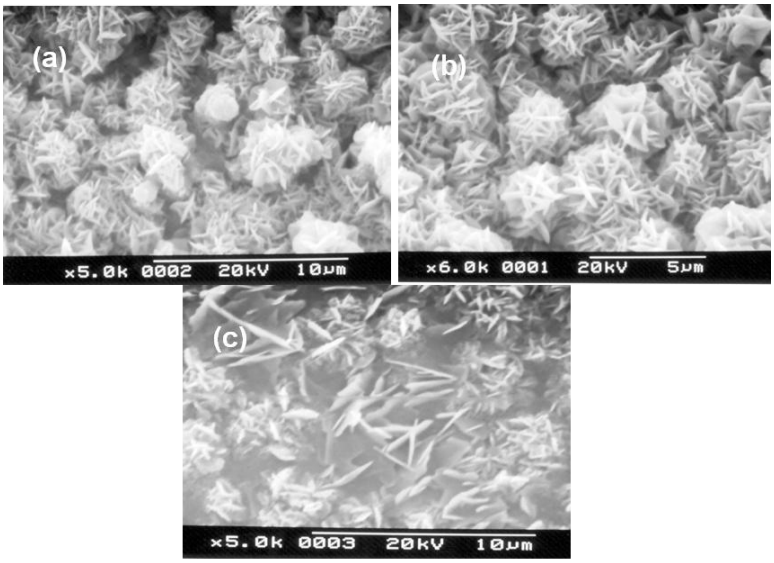

Figure 6.10: SEM images of CdS showing (a, b) cauliflower morphology, (c) lamellar to needle like transition

Mn from 5 to 10 mmol (as per the experiment performed), it has been observed that this lamellar-to-rod transition has decreased. Figure 6.11 (c) shows the fragmentation of these Mn doped CdS-En (5 mmol Mn) lamellae to higher level as compared with those of figure 6.11 (d) (10 mmol Mn), where this fragmentation is still in the initial stage. The reason behind this inhibition of CdS nanowire growth, on addition of Mn dopant, is not clear at the moment. The Mn dopant is considered to bind to the most stable surface sites formed during the nanowire nucleation, which inhibits the advancement of the growth in the particular direction [140].

Figures 6.12 (a, b, c, and d) show the formation of high aspect ratio (up to 100) CdS nanowires. The diameters of the synthesized nanowires range from 9 to 18 nm, whereas the length varies from 0.5 to 1.5 μm. Figures 6.12 (a, b) show the bundles of the CdS nanowires, where the individual nanowires can be well distinguished, whereas figures 6.12 (c, d) show the individual nanowires. Moreover, the flexibility of the CdS nanowires can be observed from figures 6.12 (c, d), by their wavy nature.

Figures 6.13 (a, b) show the uniform and high yield of CdS nanorods, synthesized on the Cd foil, as a substrate, at 140 ^{o}C for 24 hour (sample C4). The CdS nanorods, having diameter, 30 nm, and length, around 200 nm, are cylindrical in shape and are bundles of around 20-30 nanorods, as seen in figure 6.13 (b). At some places on the Cd substrate, tetrapod-like nanostructures have also been fabricated, as shown in figure 6.13 (c). An enlarged view of these tetrapods shows that the cross-section of the arms is of hexagonal shape. This shows that the solvothermal technique can be used to synthesize more sophisticated structures, where size, shape, and connectivity of multiple parts of a structure can be tailored in an independent and predictable manner [141]. This can be achieved by optimizing the reaction pa-

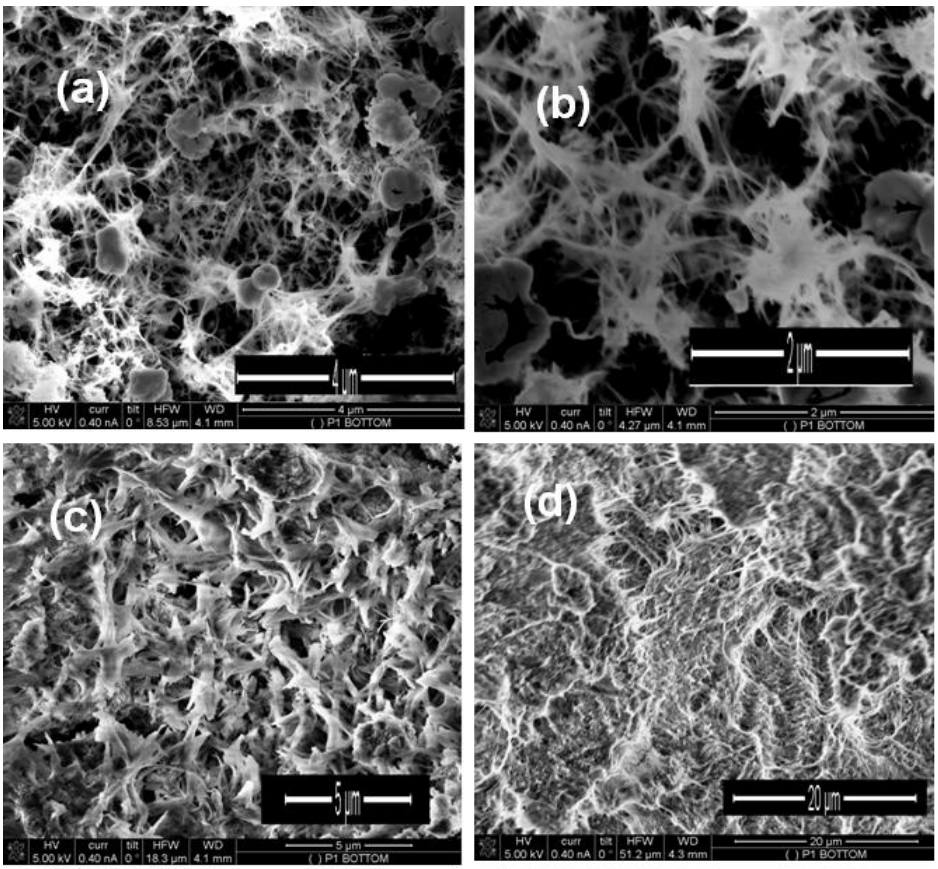

Figure 6.11: SEM images of undoped and Mn doped CdS nanostructures (sample C3); (a, b) undoped, (c) 5 mmol Mn doped and (d) 10 mmol Mn doped

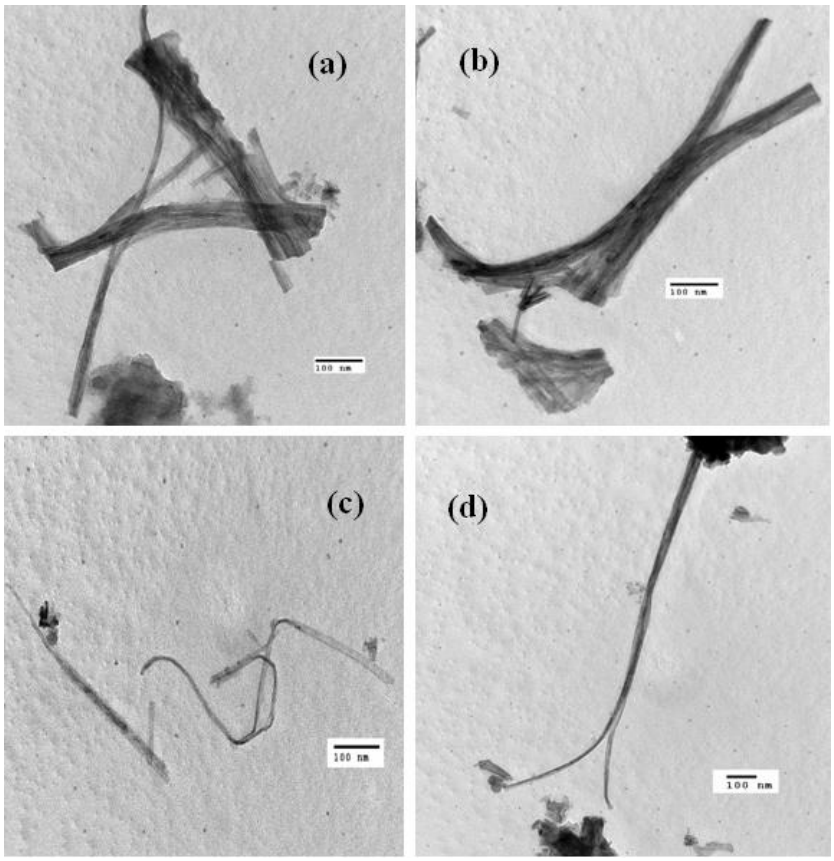

Figure 6.12: TEM images of CdS nanowires (sample C3)

rameters so that the nucleation and the growth rate can be balanced to yield such complex morphologies.

To study the effect on Mn dopant on these nanorods, synthesized at 140 ^oC for 24 hour (sample C4), 5.0 and 10.0 % atomic concentrations of Mn were added additionally, in the teflon-lined chamber during the solvothermal synthesis. As shown in figures 6.14 (a, b), a high yield of $Cd_{0.95}Mn_{0.05}S$ nanorods has been synthesized. These nanorods have diameters between 52 to 175 nm and the length, around 600 nm. The crop of Mn (5.0 at. %) doped CdS nanorods is unevenly aligned. Moreover, as seen from figure 6.14 (a), at certain areas, the tetrapod-like nanostructures have also been synthesized. The reason, behind this increase in the diameter and length of the Mn doped CdS nanorods, is not clear at the moment. As explained by Datta et al., the organic ligand present in the Mn-salt has possibly increased the solubility constant, of the other salts, and has facilitated the growth, at higher doping concentration [142].

Whereas, on further increase in the concentration of Mn dopant ions to 10 atomic %, the diameter of the nanorods has decreased to 35 nm and the length has decreased to around 350 nm, on an average, as shown in figures 6.14 (c, d). The crop of CdS:Mn (10 %) nanorods is well aligned and homogeneous. This shows the effect of Mn doping on the morphology of the CdS nanorods.

Moreover, as seen in figure 6.15, pyramidal microstructures have also been synthesized along with the nanorods in case of CdS:Mn (10 %) sample. These micropyramids are of uniform shape and size and are spread on the entire surface of the

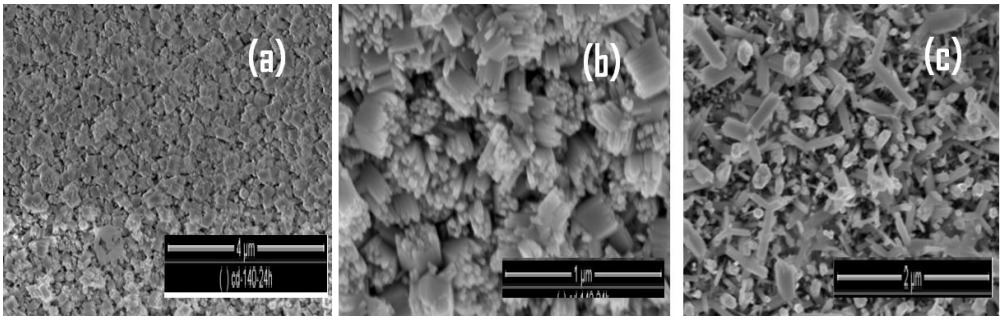

Figure 6.13: SEM images of the CdS nanorods (a, b) at different magnifications, (c) tetrapod-like structures (sample C4)

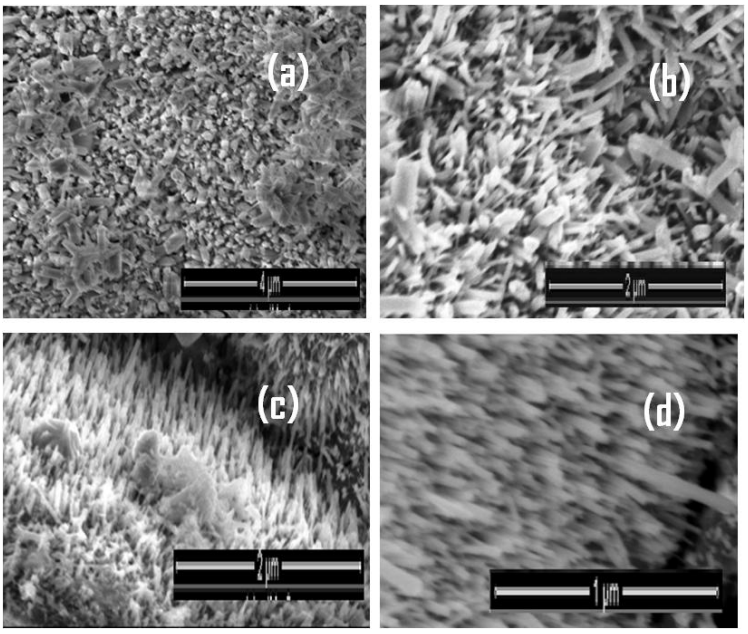

Figure 6.14: SEM images at different magnifications and angles: (a, b) $Cd_{0.95}Mn_{0.05}S$ nanorods and (c, d) $Cd_{0.90}Mn_{0.10}S$ nanorods

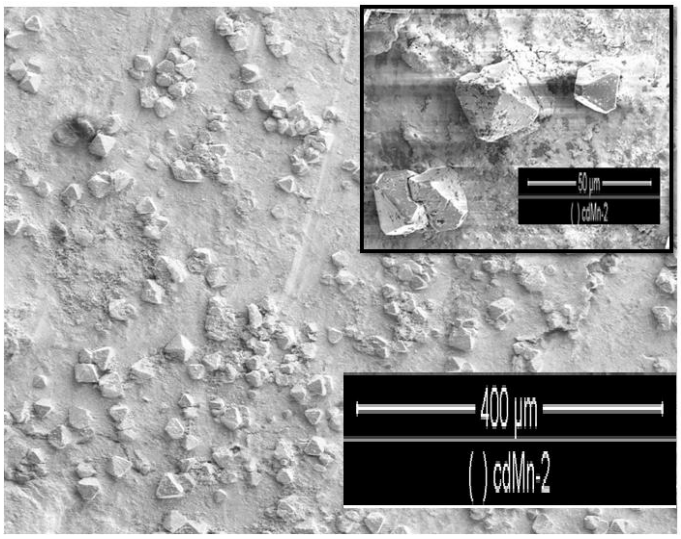

Figure 6.15: SEM image showing the CdS:Mn micro-pyramid formation along with a highly dense crop of CdS:Mn nanorods. Inset shows the magnified image of the CdS pyramid.

substrate, i.e., Cd foil.

Figures 6.16 (a, b) show the SEM images of the highly dense crop of Eu-doped CdS nanorods. The diameter of these nanorods is $\sim$ 16 nm and the length is varying between 50 and 150 nm as shown in the TEM image (figure 6.17). The fabricated CdS:Eu nanorods have uniform diameter throughout their length and are cylindrical. TEM images show that the nanorods are monodispersed and no coalescence with the neighboring nanorods has been observed. Figure 6.17 (d) shows an L shaped nanorod during its fabrication, indicating the change in the growth direction.

The EDAX spectrum of CdS:Eu (1 %) nanorods is shown in figure 6.16 (c). The Cd L-fluorescence (Lα in the 3-4 keV energy range), S K-fluorescence (Kα in the 2.0-2.5 keV energy range) and Eu L and M-fluorescence (Lα, Lβ and Lγ in the energy range 5.5-8.0 keV, and Mα in the energy range 1-2 keV) are observed. This fluorescence spectrum shows the presence of Cd, S and Eu as the elementary components

in the atomic percentage respectively 46.78 %, 52.35 %, and 0.87 %. This shows that Eu has replaced Cd upto only 0.87 atomic %, whereas 1.0 % concentration of Eu has been added during the synthesis process.

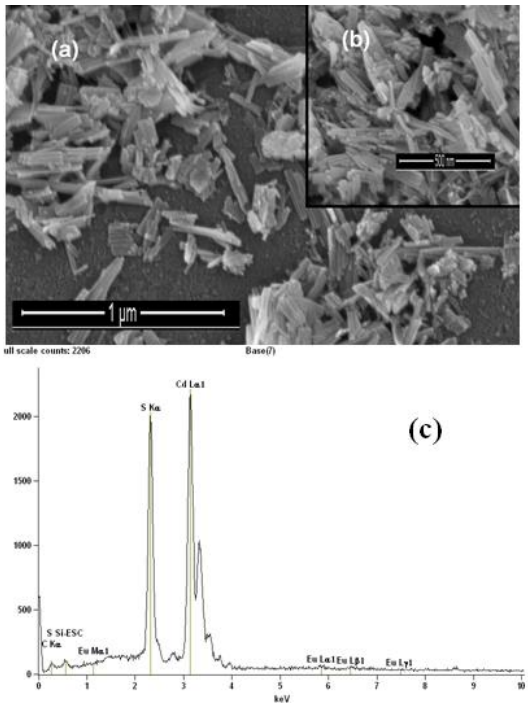

Figure 6.16: (a, b) SEM image of CdS:Eu nanorods, inset shows the high resolution image, (c) EDAX spectrum of CdS:Eu nanorods

Figures 6.18 (a, b, c, and d) show the SEM images of the undoped and Tb doped (1.0 and 5.0 at. %) nanorods (sample C6). Figures 6.18 (a, b) show that the CdS nanorods have an average diameter of 45 nm, and the length, varying from 311 to 540 nm. On doping the CdS nanorods with Tb (1.0 at. %), the average diameter of the nanorods has been found to increase to 72 nm and the length, varying between 414 to 903 nm, as shown in figure 6.18 (c). With further increase in the dopant concentration to 5.0 %, the average diameter of the nanorods has increased to 92

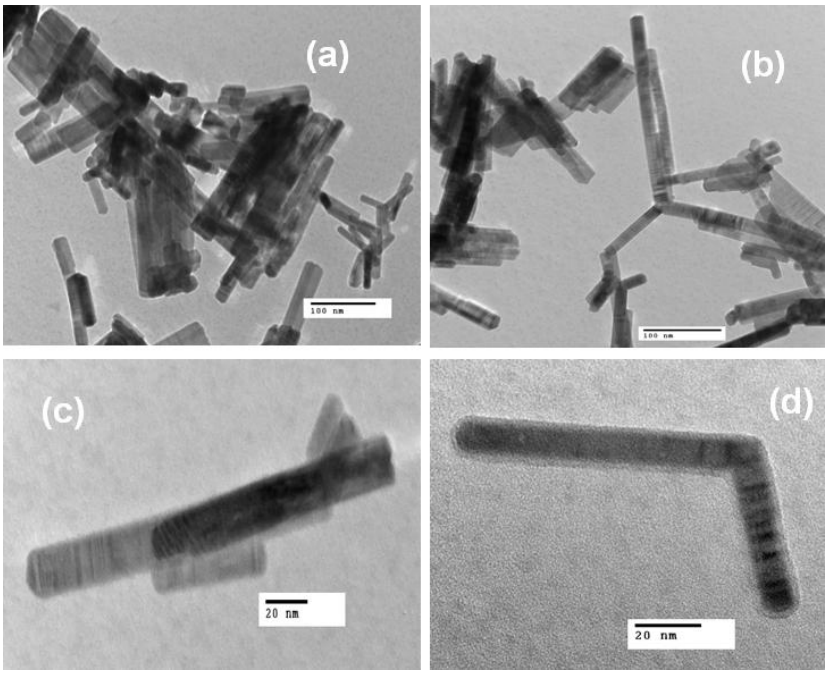

Figure 6.17: TEM images of the CdS:Eu nanorods at different resolutions

nm and the length is found to vary between 910 to 1006 nm (figure 6.18 (d)). This shows that the morphology of the nanorods is highly influenced by the presence of Tb ions as a dopant, and further, it is changing with increase in the concentration of Tb. The synthesized nanorods are of uniform diameter throughout the length of the nanorods, giving them a cylindrical shape. The yield of the nanorods is quite high. This shows the effectiveness of the solvothermal technique used to synthesize the sample. Moreover, on comparing the SEM images for CdS:Tb nanorods having Tb concentrations of 0 %, 1.0 % and 5.0 %, it seems that the roughness of the surface of the nanorods is increasing.

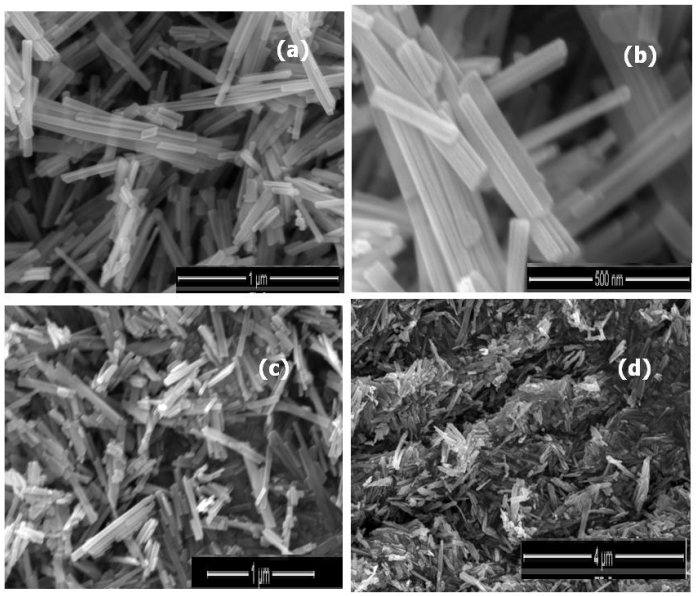

Figure 6.18: SEM images of nanorods: (a,b) undoped CdS (c) CdS:Tb (1.0 at %) and (d) CdS:Tb (5.0 at. %)

The TEM images of CdS:Tb (0.1 %) nanorods are shown in figure 6.19 (a, b), and the selected area diffraction pattern (SAED) is shown in figure 6.19 (c). The nanorods finely dispersed in ethanol were taken on the carbon coated copper grid and TECHNAI G220 S-TWIN transmission electron microscope of FEI Nether-

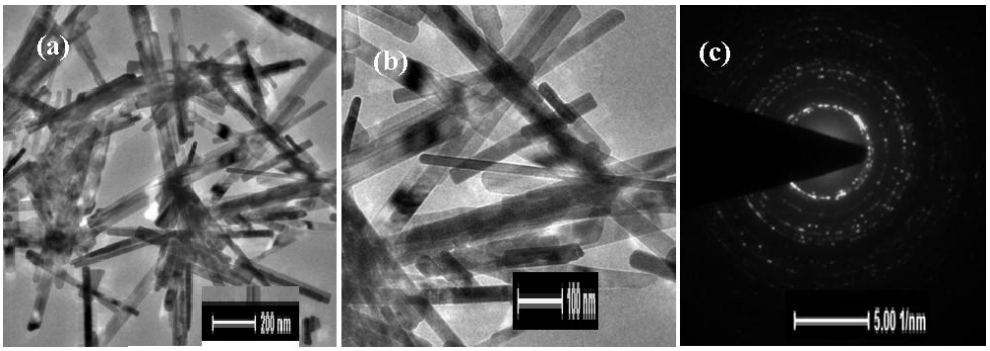

Figure 6.19: (a, b) TEM images of the annealed nanorods of CdS:Tb(0.1 %); (c) SAED pattern corresponding to (a)

lands, have been used. The diameter of the monodisperse and uniformly cylindrical nanorods is around 40 nm. The SAED pattern shows the polycrystallanity of the synthesized product.

The composition of the CdS:Tb (1.0 %) nanorods was analyzed by EDAX spectroscopy, using Noran System Six, as shown in figure 6.20. Electron beam induced inner-shell ionization and subsequent emission of characteristic fluorescence are analyzed in order to obtain the composition. As shown in figure 6.20, Cd L-fluorescence (Lα in the 3 - 4 keV energy range), S K-fluorescence (Kα in the 2.0 - 2.5 keV energy range) and Tb L and M-fluorescence (Lα, Lβ and Lγ in the energy range 6.0 - 8.5 keV, and Mα in the energy range 1 - 2 keV) are observed. This fluorescence spectrum shows the presence of Cd, S, and Tb as the elementary components in the atomic percentage respectively, 48.55 %, 51.0 %, and 0.45 %. This shows that Tb has replaced Cd upto only 0.45 atomic %, whereas 1.0 % concentration of Tb has been added during the synthesis process. The concentration of S is slightly more than that of Cd, as expected. This is due to the fact that the molar ratio of Cd and

S taken during the synthesis was 1:3. A good amount of S is also removed along with the byproducts of the reaction.

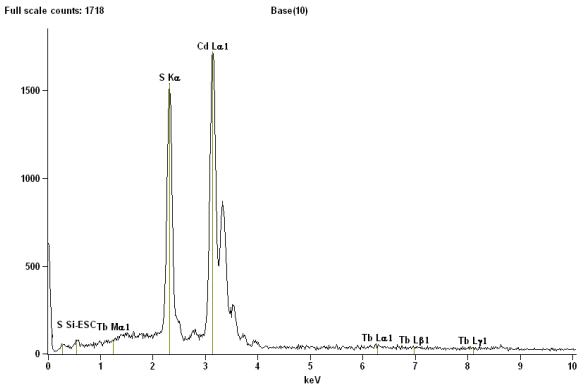

Figure 6.20: EDAX spectrum of the CdS:Tb (1.0 %) sample

Figure 6.21 (a) shows the SEM image of monodisperse and cylindrical CdS nanorods having diameter, 22 nm, and length varying between 120 and 300 nm. Whereas the SEM image of CdS/ZnS nanostructures, figure 6.21 (b), show that they are in the form of rectangular slabs having thickness, 83 nm, breadth, 430 nm and the length varying between 660 and 830 nm. This data has also been supported by the TEM images, as shown respectively in figures 6.22 (a) and 6.23 (a, b). As seen from figure 6.21 (b), these nanoslabs have coalesced to form a fractal-like cauliflower morphology. The thickness is found to be uniform throughout the length of the CdS/ZnS nanoslabs.

Moreover, it can be seen from figure 6.23 (c) that the synthesized CdS/ZnS nanoslabs have the CdS nanorods embedded in them. These CdS nanorods have been synthesized in the first step of the solvothermal synthesis and have been used as one of the ingredients for the second step. ZnS might have deposited in the on these CdS nanorods and the crystallization finally took the shape of the nanoslabs

as shown in figure 6.23 (c). Such structures are the first of its kind to the best of our knowledge. The SAED patterns, as shown in figures 2.22(b) and 2.23(c) show the polycrystalline nature of the synthesized nanoforms.

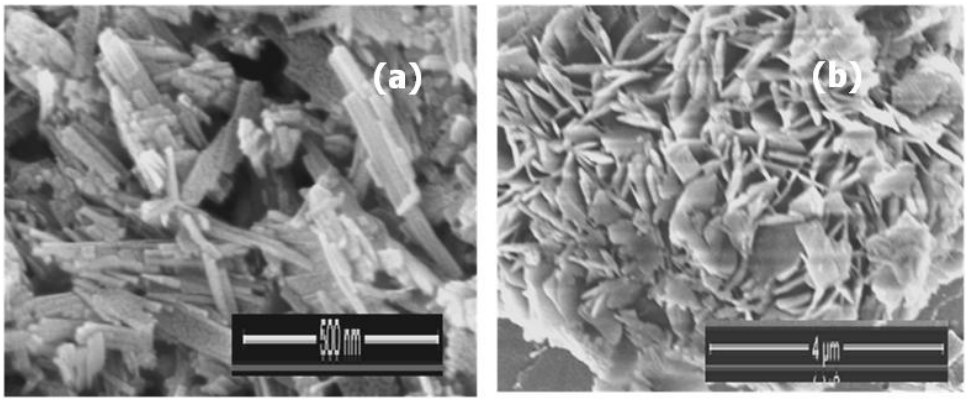

Figure 6.21: SEM images of (a) CdS nanorods (b) CdS/ZnS nanostructures

6.7 Fourier Transform Infra-red (FTIR) Studies

FTIR spectroscopy has been used to investigate the organic chemical components present in the synthesized samples. Powered samples have been used with FTIR Spectrum BX-II (Perkin Elmer) Spectrometer, without any further specimen preparation. Figure 6.24 shows the FTIR spectra of the CdS nanorods synthesized solvothermally, at 200 ^{o}C for 10 hour. The FTIR peak at 674 cm^{-1} indicates the presence of C-S linkage in the CdS nanorods, and the peak observed at 1222 cm^{-1} can be attributed to the presence of the unconjugated C-N linkage in primary, secondary, and tertiary amines. The N-H bending and stretching vibrations also show a

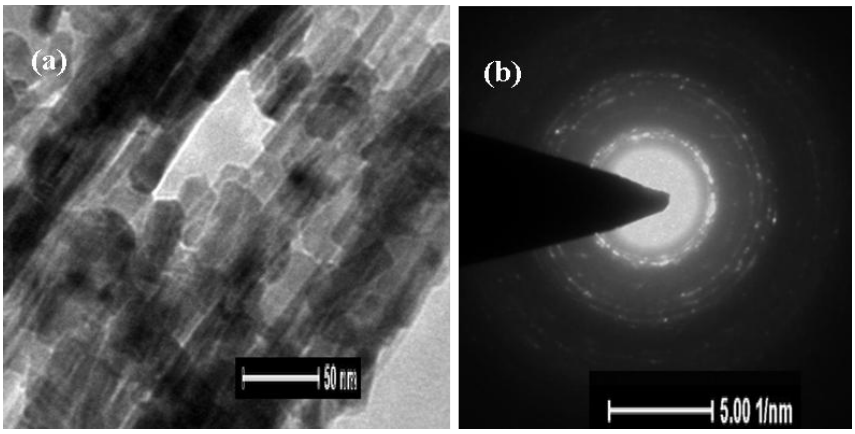

Figure 6.22: (a) TEM image, and (b) SAED pattern of the CdS nanorods

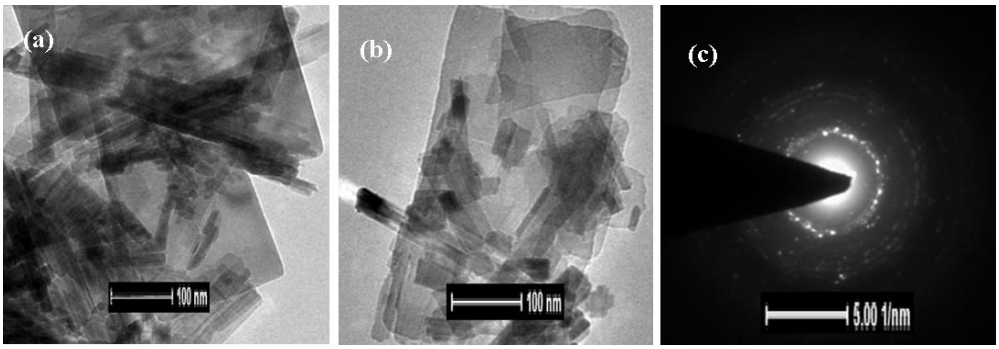

Figure 6.23: (a, b) TEM images, (c) SAED pattern of CdS/ZnS nanostructures

moderate to weak absorption at 1600 cm^{-1} as seen from figure 6.24. The weak peak positioned at 2054 cm^{-1} is due to C≡C triple bond. The broad band at 3259 cm^{-1} is a consequence of O-H, N-H stretching vibrations. These results support the presence of ethylenediamine complexes with Cd ions on the surface of the nanorods. As shown in figure 6.25, similar results have been obtained in the case of CdS nanorods doped with Tb, before and after annealing.

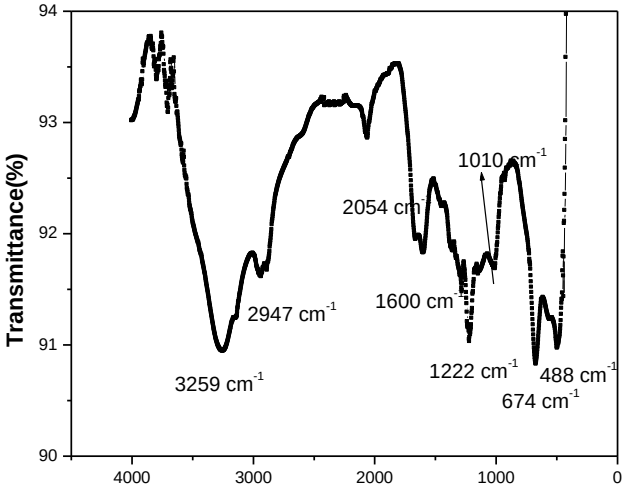

Figure 6.24: FTIR spectra of CdS nanorods

Figure 6.26 shows the FTIR spectra of CdS nanorods and the CdS/ZnS nanostructures (sample C7). Both the spectra overlap on each other with minor changes, like enhanced intensity of the peak at 1653 cm^{-1} and an additional peak at 487 cm^{-1}, in case of CdS/ZnS nanostructures. This weak peak at 487 cm^{-1} is due to the S-S stretching vibrations, which may occur due to the S-S interaction between CdS and ZnS, in case of CdS/ZnS nanostructures. Thus the formation of [CdS-En-ZnS] is

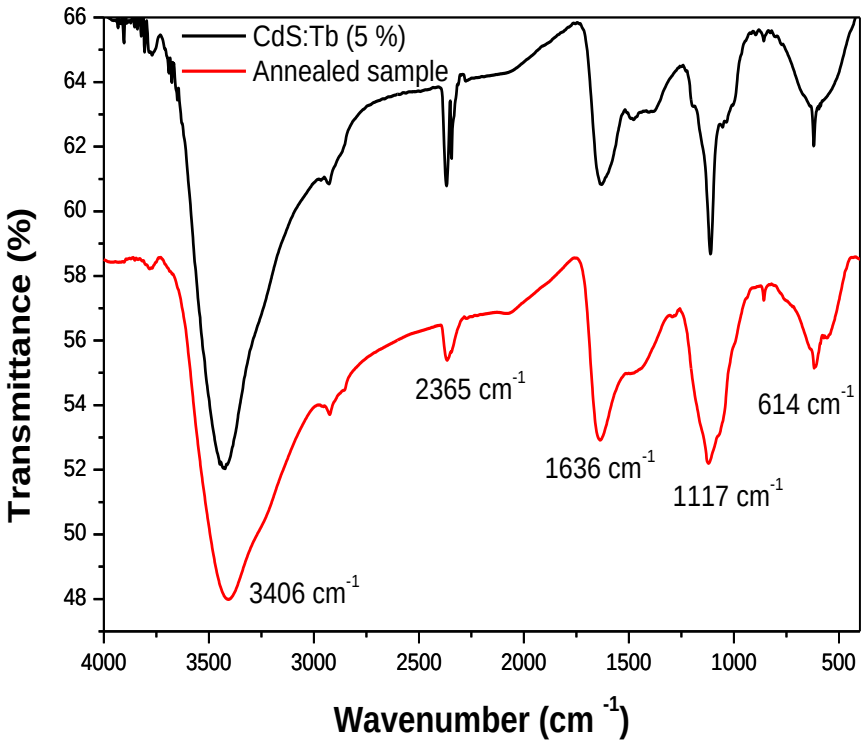

Figure 6.25: FTIR spectra of CdS:Tb (5 %) nanorods with and without annealing

confirmed as explained in equation 6.6.

The strong and broad peak centered around 3322 cm^{-1} is due to the asymmetric as well as symmetric N-H stretching vibrations. The weak peak at 1653 cm^{-1} is due to the stretching mode of C=C group present in En, whereas the doublet at 2968 and 2877 cm^{-1} is due to the aliphatic C-H stretch. The strong broad band at 615 cm^{-1} may be ascribed to the N-H wagging, and at 881 cm^{-1} to the $= CH_2$ wagging and C-H out of plane bending [65]. The strong doublet at 1090 and 1037 cm^{-1} is due to the in-plane C-H bending and the peak centered at 1377 cm^{-1} is due to the C-N stretching. This shows the presence of En group in the synthesized samples.

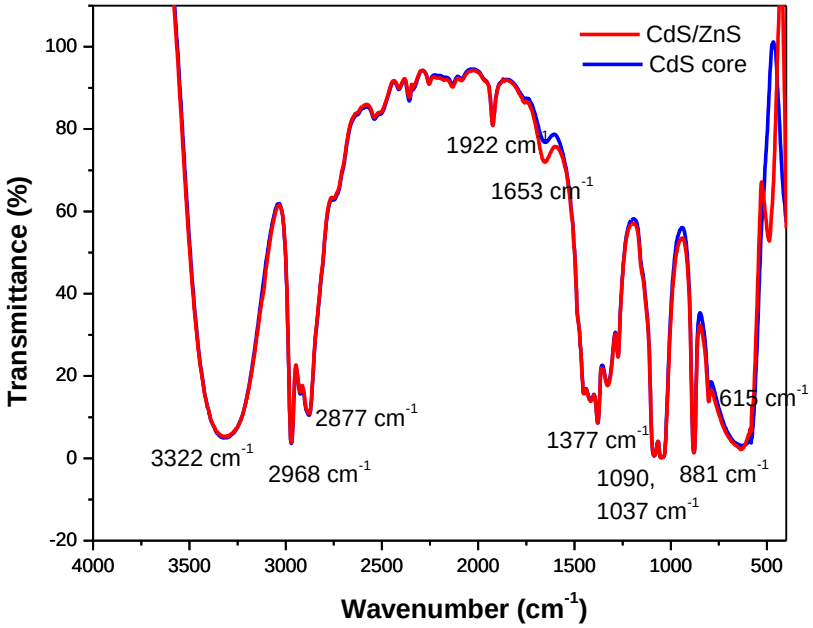

Figure 6.26: FTIR spectra of CdS nanorods and CdS/ZnS nanostructures (sample C7)

6.8 Optical Absorbance

Figure 6.27 shows the optical absorption spectra of the solvothermally synthesized undoped and Mn-doped CdS nanowires (sample C3). The maximum absorption peak positions of CdS and CdS:Mn nanoforms are at 460 and 469 nm respectively, as compared with that of bulk CdS (515 nm). The band gap energies were calculated with the help of the differential minima, which varied from 2.48 to 2.44 eV on doping with Mn (5 mmol). The observed diameters of the CdS nanowires are well above its Bohr's exciton radius ($\sim$ 2.8 nm). Therefore, this shift in the band gap energies may not be related with quantum confinement effect. The small change in the band gap values may be attributed to the direct energy transfer between the semiconductor excited states and the 3d levels of the Mn^{2+} ions, that are coupled by energy transfer processes [143].

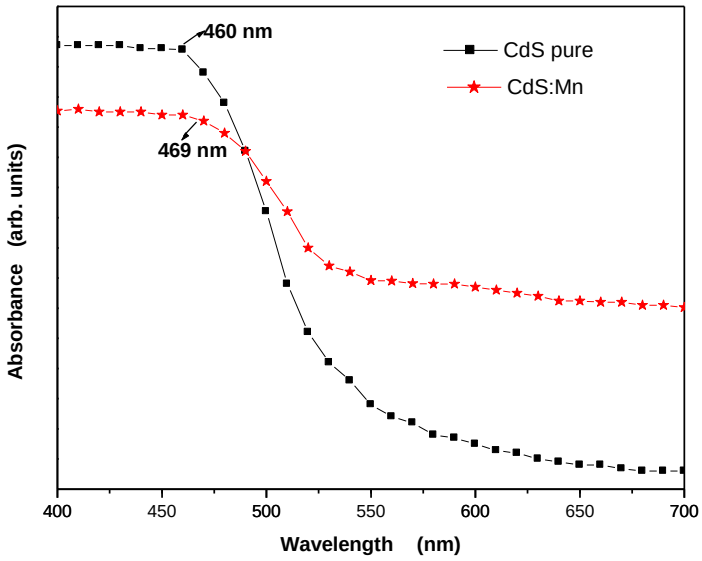

Figure 6.27: Optical absorbance of the CdS nanowires - undoped and doped with Mn (sample C3)

The UV-visible absorption spectra of undoped and Eu^{3+} doped CdS nanorods are shown in figure 6.28. The absorption spectra are broad and there is a slight blue shift in the absorption edge on the addition of Eu^{3+} dopant, which increased with the concentration of the dopant. The band gap energies of the fabricated CdS nanorods have been calculated using differential minima, which have been observed at 2.40 eV. It has been observed that there is no significant change in the band gap energies on doping CdS nanorods with Eu^{3+}. Only a slight shift in the absorption edge on the addition of Eu^{3+} has not altered the value of the band gap energy.

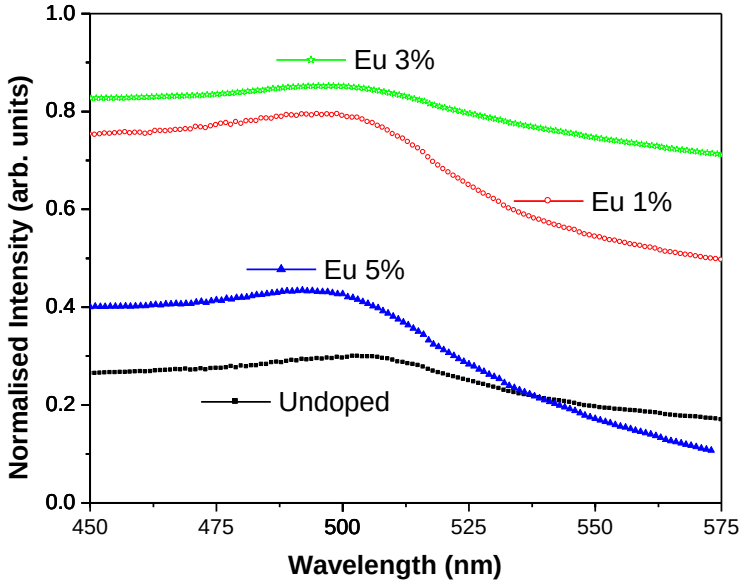

Figure 6.28: UV-visible absorption spectra of CdS:Eu (0, 1.0, 3.0, 5.0 %) nanorods (sample C5)

Undoped and Tb-doped CdS nanorods, finely dispersed in ethanol, have been used for the UV-visible absorption studies by using Specord 205 Spectrophotometer (Analytik Jena). As shown in figure 6.29, the absorption spectra of CdS nanorods doped with 1.0 % Tb shows a distinguished excitonic peak at around 491 nm, which has been red shifted by 10 nm, on heat treatment of the sample, at 200 ^{o}C for 2

hour, in nitrogen gas atmosphere. In general, the excitonic peak appears, if the defect density is considerably low. Therefore, from the optical absorption spectrum, it is evident that the CdS nanorods, so formed, are of high optical quality.

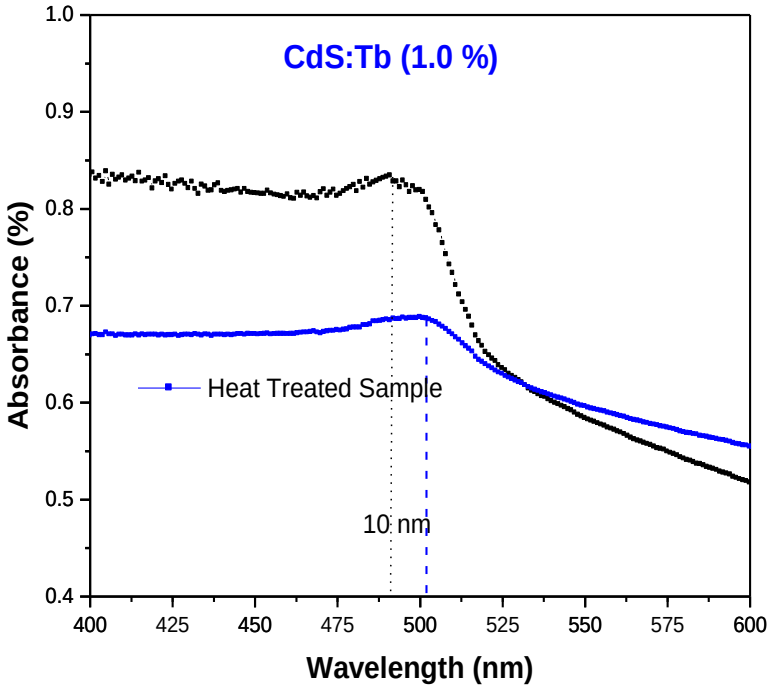

Figure 6.29: Absorption spectra of CdS doped with terbium (1 %), synthesized and heat treated (sample C6)

UV-visible absorption spectra of the CdS nanorods and the CdS/ZnS nanostructures have been shown in figure 6.30 (sample C7). The band gap values of both the samples have been calculated from the minima of the first derivative of the absorbance versus wavelength spectra, which gives the band gap value to be 507 nm (2.45 eV). There is no change in the calculated optical band gap values in both the samples, whereas the absorption peak has become broadened in case of CdS/ZnS nanostructures, and the band edge shows a slight blue-shift. However, according

to Datta et al., instead absorption peak becomes sharper and the absorption edge shows a slight red-shift when CdS nanorods are coated with ZnS [144]. The opposite results in the two works might be due to different thickness of ZnS coating layers on CdS nanorods.

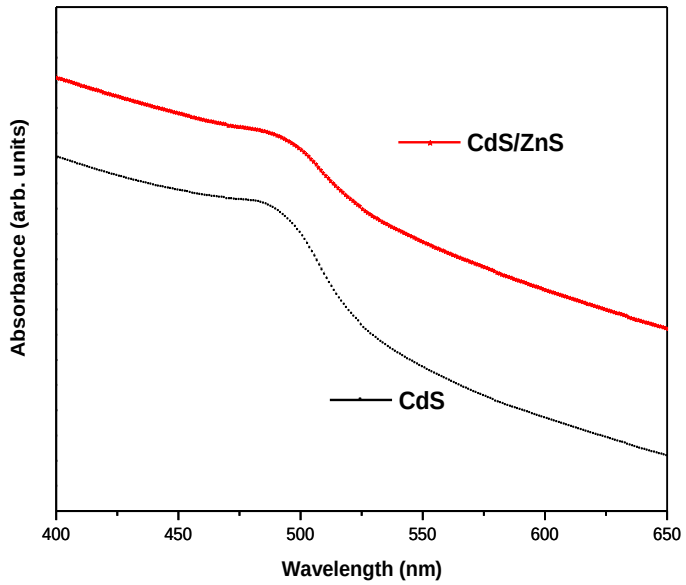

Figure 6.30: Optical absorption spectra of the CdS nanorods and CdS/ZnS nanostructures (sample C7)

Chapter 7

Photoluminescence properties of ZnS and CdS nanostructures

The optical properties of ZnS and CdS, and its wide variety of nanostructures are of immense scientific and industrial interest. Moreover, nanocrystals doped with optically active luminescence centres create new opportunities for luminescence research and also for the application of nanometer-scale structured material.

In this chapter, room temperature photoluminescence (PL), energy-resolved and time-resolved, properties of the synthesized ZnS and CdS nanostructures will be presented.

7.1 Room temperature PL properties of ZnS nanoparticles

7.1.1 Undoped and Mn-doped ZnS nanoparticles

Photoluminescence (PL) measurements were carried out at room temperature with a luminescence spectrometer (Hitachi, FL 2500) using 325 nm as the excitation wavelength. The specimen preparation has been carried out by finely dispersing the nanoparticles in spectroscopic grade ethanol, using an ultrasonicator.

As shown in figure 7.1, PL spectra for the undoped ZnS nanoparticles show two emission bands, one blue emission at 420 nm and another yellowish green band at 575 nm. The blue emission band is associated with the recombination of free charge carriers at defect sites, possibly at the surface of nanostructures [145, 146]. The yellowish green band at 575 nm is most likely due to the self - activated defect centres formed by the zinc vacancy inside the lattice [147, 148]. The orange emission around 582 nm can be attributed to the $4T^1$ - $6A^1$ transition of the Mn^{2+} impurity. The characteristics of the Mn^{2+} impurity are almost identical to the emission observed for Mn^{2+} in bulk ZnS [29]. The intensity of the orange emission (582 nm) first increased and then decreased with the increase of Mn concentration. Emission intensity is much higher for 5 % incorporation as compared to 10 % and 15 % doping. This effect might be due to concentration quenching, due to which the increased availability of the dopant ions increase the number of energy transfers between the initially absorbing impurity ions, to another identical ions instead of immediately resulting in radiation (luminescence). After a number of such processes,

a transfer to a quenching site (e.g. a defect) may become involved, thus further decreasing the radiative process. This explains that the increase in Mn impurity concentration above a certain value could lead to a reduction in PL intensity [168]. This is also clear from figure 7.2, which shows that as Mn concentration increases to 5 %, there is an increase in orange emission intensity as compared to the blue emission. But further increase in Mn concentration leads to gradual decrease in the orange emission intensity. The yellowish-green emission (575 nm) disappeared on addition of manganese to the ZnS nanoparticles; this indicates that its origin could be zinc-vacancy related defect states. The addition of the Mn^{2+} ion could have filled the Zn vacancy sites, resulting in the reduction of the intensity of this peak, due to quenching of self activated centres. It was also observed that PL peak position (582 nm) is independent of the manganese concentration.

7.1.2 Ni-doped ZnS nanoparticles

Figure 7.3 shows the room temperature PL spectra of $Zn_{0.999}Ni_{0.001}S$ nanoparticles using a xenon lamp at the excitation wavelength of 275 nm. The blue emission centered at 425 nm may be associated with the recombination of the charge carriers due to the transitions from the localized states. These localized states can be due to the interstitial Zn atoms or the vacancies due to Zn and S atoms, as explained by the schematic energy level diagram given by Denzler et al. [46]. The green emission centered at 547 nm may be attributed to the d-d optical transitions of Ni^{2+} luminescent centres [52].

Figure 7.4 shows the variation of the strong green emission, centered at 547 nm,

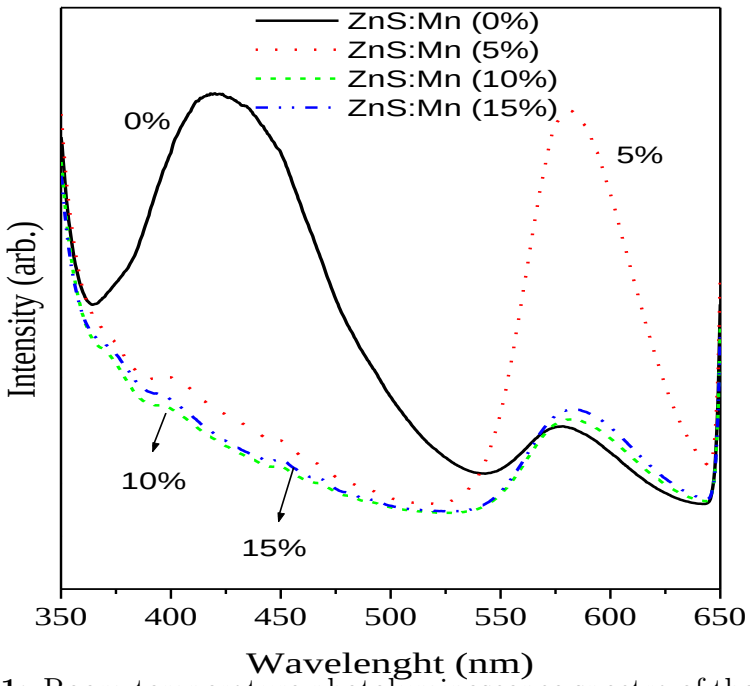

Figure 7.1: Room-temperature photoluminescence spectra of the ZnS: Mn nanoparticles

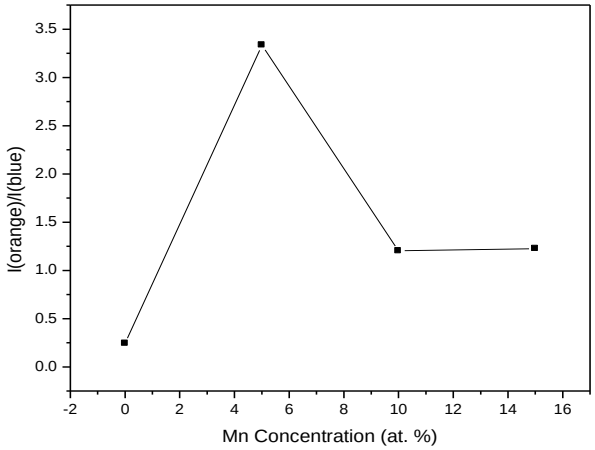

Figure 7.2: Actual intensity ratio of the orange to blue emissions versus atomic % of Mn

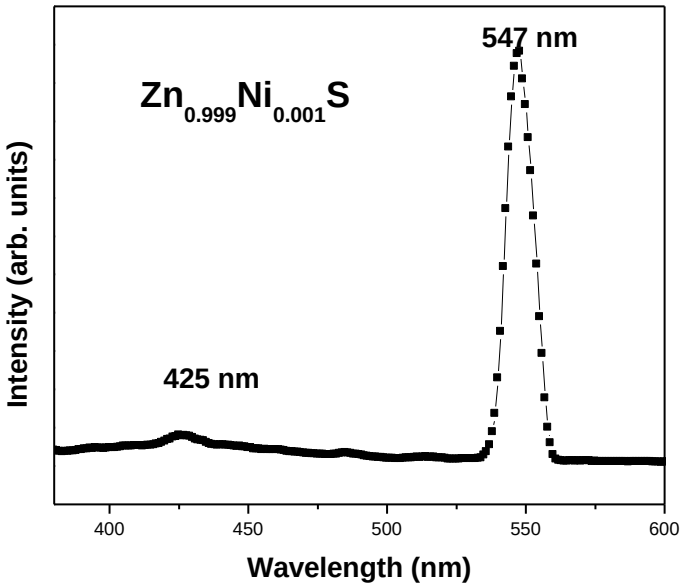

Figure 7.3: Room temperature PL spectra of $Zn_{0.999}Ni_{0.001}S$ nanoparticles using a xenon lamp at the excitation wavelength of 275 nm

in the Ni-doped ZnS nanoparticles, with the change in the concentration of the dopant. The luminescence intensity of the green emission has increased with the increase in Ni concentration upto 0.5 at. % of Ni dopant, and further increase in the concentration of Ni has decreased the luminescence intensity. However, the intensity ratio of the green to blue emission is found to increase continuously, on increasing the concentration of the dopant as shown in figure 7.6.

Figures 7.5 and 7.6 show the effect of prolonged UV-irradiation on the luminescence intensity of the Ni-doped ZnS nanoparticles. The UV-irradiation has enhanced the PL intensity of the strong green emission for all concentrations of Ni. Higher is the concentration of Ni in ZnS nanoparticles, greater is the enhancement. Due to the high surface to volume ratio of the nanoparticles, the number of electron or hole trapped surface levels are higher. These surface states play an important role

in the luminescent properties of the nanomaterials. In nanoparticles, most of the ions at the surface are non-saturated in coordination. Electrons and holes may be excited easily and escape from the ions. Many carriers trapped at the surface states or defect sites may be released by photo excitation [53]. Moreover, on UV radiating the samples with 255 nm (4.86 eV) wavelength radiations for prolonged duration, the divalent Ni d^8 ions may photo-ionize to Ni d^9 ions by removal of an electron from the top of the valence band [149].

The prolonged UV-irradiation may lead to this photo-excitation and photo-ionization effects, which may further be responsible for the enhanced luminescence efficiency of the Ni-doped ZnS nanoparticles as shown in figures 7.5 and 7.6. Similar effects of high quantum yield have also been shown by Tsay et. al, [150] in case of CdSe/ZnS core/shell nanostructures. They have attributed this enhancement to the photo-annealing of the defects in the shell (ZnS) on prolonged UV-irradiation with a 4W UV lamp with 366 nm radiation for 40 minute to several hour.

7.1.3 Cu-doped ZnS nanoparticles

Figure 7.7 shows the photoluminescence spectra of the ZnS:Cu nanoparticles upon 350 nm excitation. The spectra are broad and asymmetric; this shows the presence of more than one component. Gaussian curve fitting was applied to deconvolute the PL curves. The PL spectrum has been deconvoluted into three blue luminescence peaks centered at 403.5, 425, and 450 nm and a blue-green peak centered at 485 nm. The PL peaks at 403.5 nm and at 425 nm have been known due to the recom-

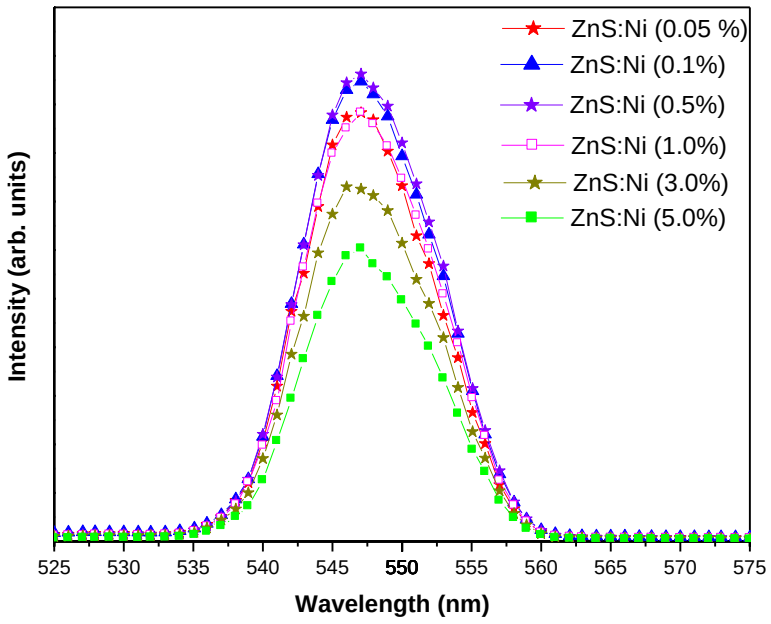

Figure 7.4: PL spectra of ZnS nanoparticles doped with Ni showing strong green emission centered at 547 nm

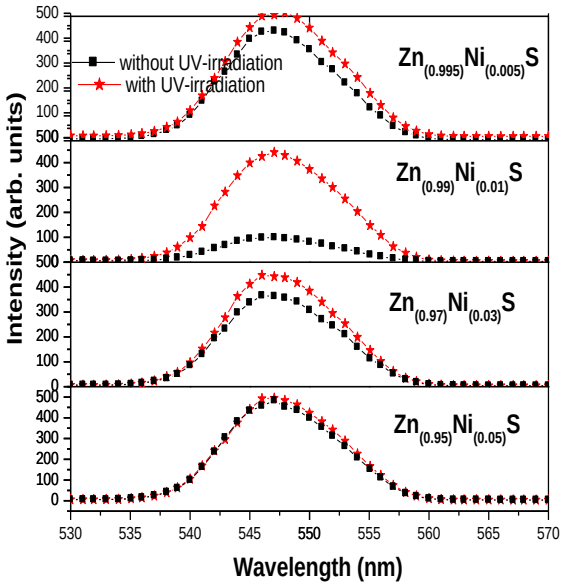

Figure 7.5: Plot of the comparison of luminescence intensity of green emission with and without UV-irradiation

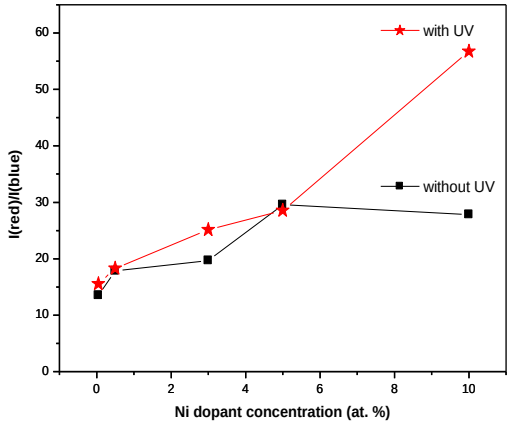

Figure 7.6: Plot of intensity ratio of green to blue emission with change in concentration of Ni

bination of the electrons between the sulfur-vacancy-related donor and the valence band [51,151]. As shown in figure 7.8, the peak positions of these blue luminescence peaks did not show a remarkable change as the Cu^{2+} ion concentration was varied, which indicates that the energy level of sulfur vacancy remains almost constant relative to the valence band. The blue-green luminescence centered around 485 nm may have originated from the recombination of an electron from the shallow delocalized donor level (sulfur vacancy) to the t_2 level of Cu^{2+} [152].

Remarkable enhancement of the luminescent intensity was observed on irradiating the ZnS:Cu nanoparticles with UV radiation of 255 nm for 24 hour at room temperature. As shown in figure 7.8, there is no shift in the peak position; therefore, the increase in luminescent intensity can be attributed to the increase in the radiative transition probabilities [153, 168] of the samples. Possibly, on UV irradiation, the photochemical reactions with oxygen might have occurred, leading to the formation of $ZnSO_4$ and/or $Zn(OH)_2$ layer around the ZnS:Cu nanoparticles [128].

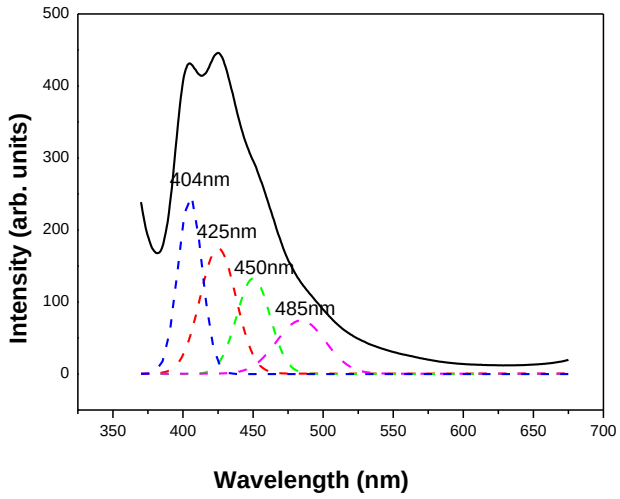

Figure 7.7: Room temperature photoluminescence spectra of the Cu-doped ZnS nanoparticles. The solid line represents the experimental data whereas the dotted lines are the individual components obtained by Gaussian fitting.

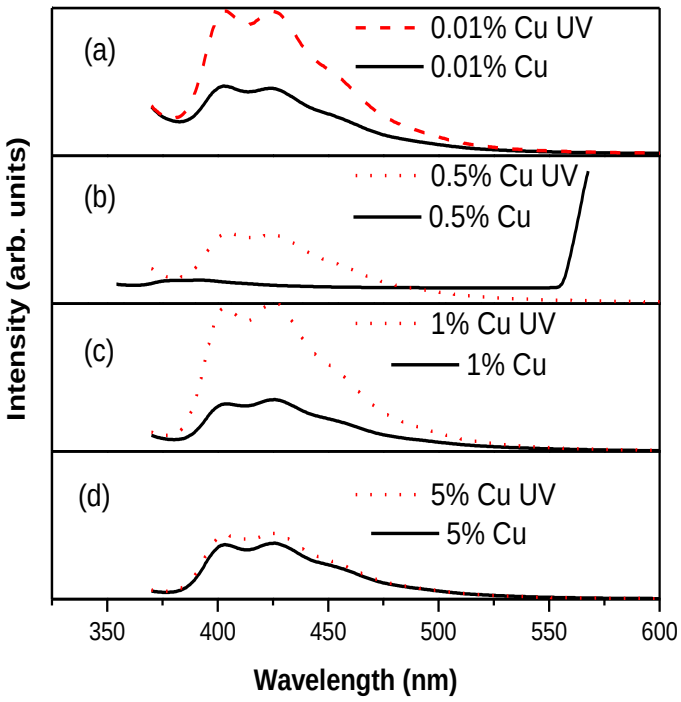

Figure 7.8: Room temperature photoluminescence spectra of the ZnS nanoparticles having different Cu^{2+} concentrations (a) 0.01 % (b) 0.5 % (c) 1 % (d) 5 %; showing the luminescence enhancement on UV-irradiation for each concentration of the dopant

This layer could have acted as an inorganic surfactant, leading to the decrease in the number of trap sites available for non-radiative transitions. It has also been observed that the increase in PL intensity is more when the concentration of the dopant Cu^{2+} ions is less as compared to the increased concentration. As shown in figures 7.8 and 7.9, this enhancement in the PL intensity on UV-irradiation is much more when the dopant concentration is 1 %; as compared to 3 % Cu^{2+} ion concentration. As discussed by Peng et. al. [51], the relative intensity of the overall photoluminescence spectra reaches the maximum at the doping concentration of 1 %, therefore, the decrease in PL intensity at higher concentrations of the dopant can be attributed to the formation of CuS, though the XRD measurement did not detect its existence. This can also be supported by the change of the color of ZnS:Cu nanoparticles from white to dark green as the concentration of the Cu^{2+} is increased. This CuS formation enhances the non-radiative transitions as well as reduces the number of Cu^{2+} ions, which act as optically active luminescent centers. Now, on UV irradiation, discoloration of the samples has also occurred, which further supports the decrease of non-radiative transitions on account of photo-oxidation reactions and hence the decrease of the non-radiative transition probability.

7.1.4 Eu-doped ZnS nanoparticles

Room temperature PL spectra of the finely dispersed ZnS:Eu nanoparticles have been measured using a xenon lamp source spectrophotometer (Cary Varian), at an excitation wavelength 320 nm.

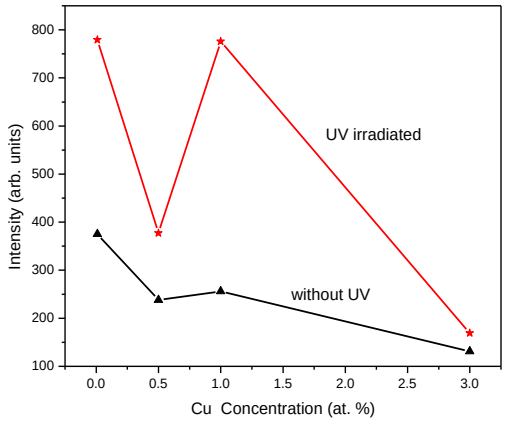

Figure 7.9: Plot of PL intensity versus the Cu^{2+} concentration (as added during synthesis) in the ZnS nanoparticles with and without UV-irradiation

Figure 7.10 shows the room temperature PL spectra of ZnS undoped and ZnS:Eu nanoparticles. The spectrum for undoped ZnS nanoparticles is broad and asymmetric, whereas on doping the nanoparticles with Eu ions, the spectra have become sharp. This shows that the Eu doping has removed the number of surface defects leading to radiative transitions. The emission at 360 nm (3.4 eV) may be due to the near band edge transitions, which can be supported by the absorption spectra showing the absorption maxima in this range. The emission at 425 and 434 nm has been known due to the recombination between the sulfur-vacancy-related donor and the valence band [154].

In the synthesis process, Eu^{3+} ions have been used. However, the possibility of Eu^{3+} ions to occupy the ZnS lattice is quite less. This may be due to the ionic radius of the Eu^{3+} ion (0.95) being larger than that of Zn^{2+} (0.75). For Eu^{3+} ion to replace a Zn^{2+} lattice site, the ZnS host lattice has to deform, which is energetically unfavorable. Besides, due to the large ionic radius, the Eu^{3+} ion prefers sites with high coordination numbers (six or higher). In ZnS, however, the coordination

number of the cation lattice site is only four, which is very unusual for Eu^{3+}. In addition, the 3+ charge of the Eu^{3+} ion has to be compensated for somewhere in the lattice. It is questionable if Eu can be incorporated in a sulfide in the trivalent state. The divalent state is expected to be more stable [63]. This has also been discussed in EDAX from other point of view.

Moreover, as reported by many researchers [155, 156], Eu^{3+} ions in ZnS give PL emission at 590, 612, and 695 nm due to ${}^5D_0 \rightarrow {}^7F_1$, ${}^5D_0 \rightarrow {}^7F_2$, and ${}^5D_0 \rightarrow {}^7F_4$, respectively. But no such emission has been found in our results as shown in figure 7.10.

This shows the possibility of the reduction of Eu ions as follows:

$$Eu^{3+} + e^- \rightarrow Eu^{2+} \tag{7.1}$$

Therefore, the blue emission centered at 485 nm and the green emission peak at 525 nm may be attributed to Eu^{2+} related emission, due to the ${}^4f_7 \rightarrow {}^4f_6\ {}^5d_1$ radiative transitions. This emission discussed here, is not consistent to the red emission in alkaline earth sulphides, because the 5d excited states of Eu^{2+} ion are host sensitive and, therefore, the ${}^4f_6\ {}^5d_1$ states split due to spin-orbit coupling and crystal field [103], resulting in blue and green emissions. As shown in figure 7.11, the emission intensity has decreased with heat treatment. Whereas no shift in the peak position has been observed.

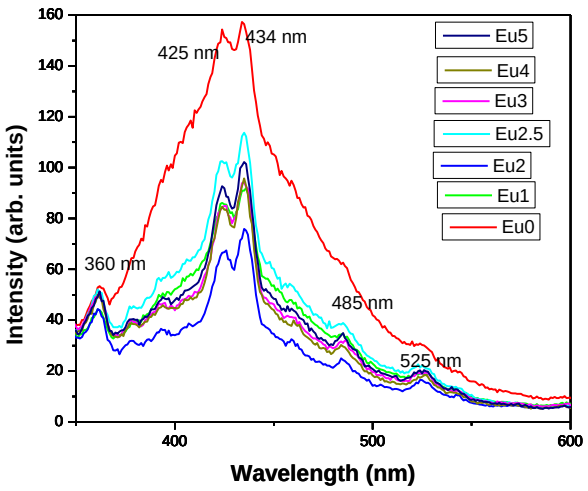

Figure 7.10: Room temperature PL spectra of ZnS:Eu (at different concentrations of Eu) nanoparticles using the excitation wavelength of 320 nm

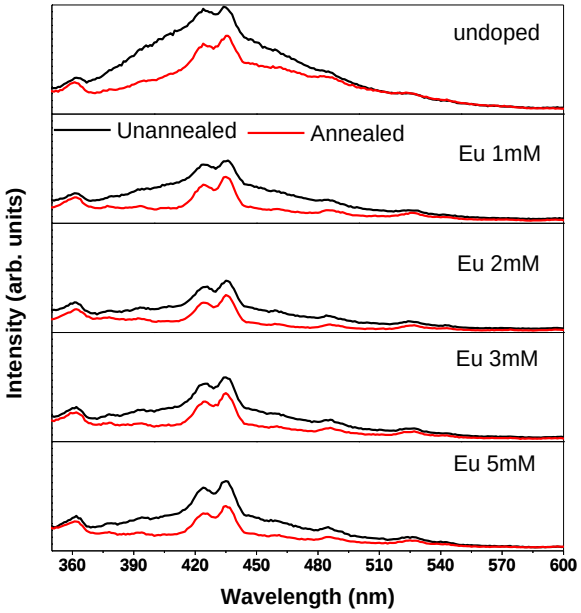

Figure 7.11: PL spectra of ZnS:Eu nanoparticles having varying concentrations of Eu, with and without annealing; excitation wavelength 320 nm

7.2 Time-resolved PL properties of ZnS:Mn nanoparticles

The luminescent time decay set-up consisted of a pulsed laser, a photosensor set-up and a digital oscilloscope interfaced with a computer. A high peak power (10 kW) N_2-Laser (337.1 nm)with pulse width $<$ 10 nm, was used as an excitation source. The angle between excitation and detection paths was 90^o and the optical filter was used to remove the scattered light. The resulting photoluminescence was detected using a photomultiplier tube (RCA 8053 PMT) and a digital storage oscilloscope (Tektronix TDS 1012) by monitoring the photoluminescence decay. The data was then stored in the computer for further analysis. Time resolved photoluminescence spectroscopy was carried out for lifetime , trap depth and decay constant measurements.

Time-resolved photoluminescence provides an effective nondestructive technique for studying the dynamics of impurities and lattice defects in semiconductors [27]. As already discussed in Chapter 3, the intensity of the luminescent radiation, at time t, is given as:

$$I = I_o e^{-pt} \tag{7.2}$$

where I_o is the intensity of radiation at cut-off position, the constant p $=1/\tau$ is the transition probability of the corresponding radiative transition and τ is the lifetime of the excited state.

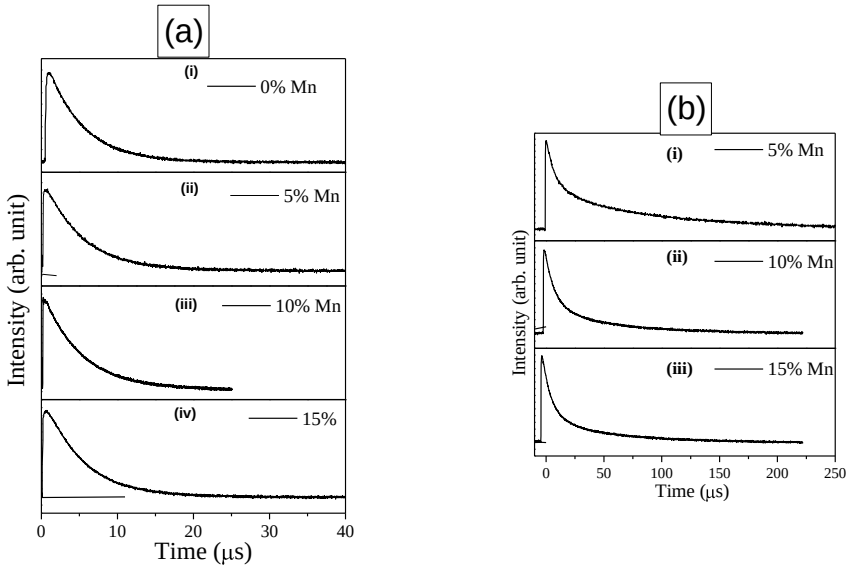

Figure 7.12: (a) Hyperbolic decay curves for ZnS: Mn nanoparticles at 420nm; (b) Hyperbolic decay curves for ZnS: Mn nanoparticles at 585nm

Figures 7.12 (a, b) show the intensity versus time graph recorded as per the time resolved photoluminescence spectra for ZnS: Mn. The decay curves can be peeled -off into three components by the peeling-off method of Bube. The results of decay curves can be expressed as:

$$I = I_{o1}exp(-p_1t) + I_{o2}exp(-p_2t) + I_{o3}exp(-p_3t) + ... \tag{7.3}$$

Where p_1, p_2 and p_3 are the transition probabilities. I_{o1}, I_{o2}, I_{o3}..... are the intensities at the cut-off position for three probability values. In the present investigation only three components have been taken because further components were having the life times of the order of a few seconds. The dopant has introduced multiple trapping levels at different depths below the conduction band in the host material in ZnS. Table 7.1 shows the excited state lifetime values for ZnS: Mn nanoparticles,

recorded at room temperature, for blue emission ($\sim$ 420nm) and for manganese related orange emission ($\sim$ 585nm).

Table 7.1: Excited state lifetime values for ZnS: Mn nanophosphors recorded at room temperature

S.No.	**Sample**	**Excited state lifetime values(μs) for blue emission (420nm)**			**Excited state lifetime values(μs) for orange emission (585 nm)**		
		τ_1	τ_2	τ_3	$\tau_1^{'}$	$\tau_2^{'}$	$\tau_3^{'}$
1.	ZnS: Mn (0%)	6.89	13.22	55.08	——	——-	——-
2.	ZnS: Mn (5%)	7.10	14.28	67.94	31.51	126.66	318.95
3.	ZnS: Mn (10%)	7.58	19.12	142.88	26.52	116.47	462.64
4.	ZnS: Mn (15%)	8.04	27.43	428.47	15.86	42.25	135.31

The levels, introduced by Mn in ZnS nanophosphors, are $^4T_1 - {}^6A_1$, which is a forbidden transition by spin selection rules and its probability is very low which gives long lifetimes, as observed for orange emission as compared to the blue emission in Table 7.1. As the concentration of manganese is increasing, the life times are reducing (Table 7.1) from 31.51 μs (for 5 at. %) to 15.86 μs (for 15 at. %). This is due to the smaller lifetimes of the excited state of interacting pairs as compared to a single Mn^{2+} centre. With the increase in the concentration of manganese impurity, the number of such interacting pairs have increased (leading to concentration quenching), causing the decrease in excited state lifetimes.

Table 7.2: Trap depth values and decay constant for ZnS: Mn nanophosphors recorded at room temperature

S.No.	Sample	Trap depth values (eV) for orange emission (585nm)			Decay constant
		E_1	E_2	E_3	
1.	ZnS: Mn (5%)	0.2683	0.3043	0.3282	1.0969
2.	ZnS: Mn (10%)	0.2638	0.3021	0.3379	1.4655
3.	ZnS: Mn (15%)	0.2505	0.2759	0.3060	1.9559

As mentioned in Table 7.2, the value of trap-depth E, has been calculated using the Boltzmann's equation [28]:

$$p = Se^{-E/kT} \tag{7.4}$$

where S is the escape frequency factor (10^9 s^{-1}), k, the Boltzmann's constant, and T, the absolute temperature. The distribution of traps in the energy band gap of the nanoparticles has been studied using the following equation:

$$I = I_o t^{-b} \tag{7.5}$$

where b is the decay constant. The value of decay constant explains the distribution of the trapping states introduced by the dopant within the band gap of the phosphor. If the value of decay constant is unity, the traps introduced by the impurity are uniformly distributed within the band gap of the nanoparticles. Otherwise,

there will be non-uniform distribution of the traps. The trap depth is maximum (0.2683 eV) for zinc sulphide doped with 5 % of Mn and minimum (0.2505 eV) for 15 % Mn doping. This shows that as the concentration of manganese has increased from 5 % to 15 %, the levels introduced by Mn impurity have become shallow. The decay constant values show that the distribution of the traps within the energy band gap of phosphors is nonuniform, and, this non uniformity has increased with the increase in the dopant concentration.

7.3 Room temperature PL properties of CdS nanostructures

7.3.1 CdS microstructures

Figure 7.13 shows the room temperature photoluminescence (PL) spectra of the CdS microstructures, using an excitation wavelength of 400 nm (3.11 eV), which is well above the band gap (2.42 eV) value of the bulk CdS. The PL spectrum shows a broad band centered at 508 nm (2.45 eV). This green colored, broad peak is attributed to the band-to-band emission [157, 158]. No deep-level defect emissions are observed. The absence of emission from trap states suggests the stoichiometric nature of CdS microstructures, without a surface excess of Cd^{2+} or S^{2-} vacancies [159].

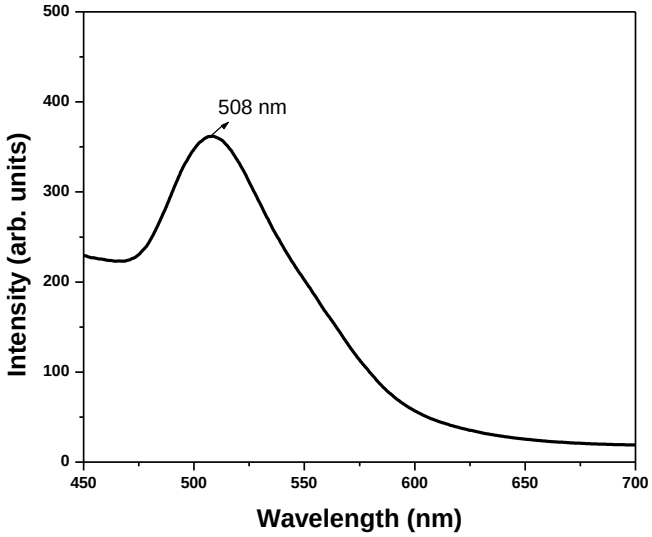

Figure 7.13: Room temperature photoluminescence spectra of CdS microstructures using an excitation wavelength of 400 nm

7.3.2 CdS nanostructures using 80 nm dia. pores

The room temperature PL spectra (excitation wavelength, λ_{exc}= 400 nm) of the 80 nm dia. CdS nanostructures has been shown in figure 7.14. In the past several decades, the luminescence mechanism of CdS have been studied. Usually, two emissions are observed from the semiconductor nanoparticles - excitonic and trapped luminescence [159]. The excitonic emission is sharp and located near the absorption edge of the particles, while the trapped emission is broad and stokes-shifted. CdS is a wide-band-gap (Eg = 2.4 to 2.53 eV) semiconductor and has typically two emission bands: green band (excitonic emission) around 518 nm and the red band (ascribed to trap of surface states) at about 732 nm [158]. But due to their 1-D geometrical characteristic, on the nanometer scale, CdS nanowires are expected to have different physical properties from their bulk counterparts. Moreover, it is also believed that

nanowires with high aspect ratio (length to diameter) have more surface and sub-surface defects such as grain boundaries, sulfur / cadmium related defects. These would definitely exert influence on the PL properties of the CdS nanowires. There are two green emission peaks centered around 531 nm and 545 nm in the PL spectra. These emissions can be ascribed to the surface donor-accepter pair recombination. The origin of the defects may be associated with sulfur/cadmium vacancies or interstitials, extrinsic defects or impurities [160]. However, no PL emission has been observed near the band gap value calculated from the absorption spectrum, 473 nm. Absence of emission from band-to-band transition has already been reported in the literature in case of CdS nanowires [160, 169] and nanoparticles [161].

The PL quantum yield of the CdS nanostructures synthesized by the template synthesis technique and the commercially available CdS bulk (analytic grade, Sd-fine Chemicals Ltd.) material has been calculated by using an optical set-up having a He-Cd laser, an Integrating Sphere and a Spectrometer (Ocean Optics). The CdS nanostructures and the commercially available CdS were irradiated by the laser beam for an integration time of 15000 ms and the number of photons per unit area, were counted. Whereas the laser beam was integrated, separately, for 1, 2 and 3 ms, etc.; thus a calibration curve was plotted for calculating the photon count for an integration time of 15000 ms.

The ratio of the number of photons emitted by the sample to the incident photons gives the quantum yield. The quantum yield of the commercially available CdS has been found to be 0.08 %, whereas it has increased to 0.28 % in case of the

synthesized CdS nanostructures. This shows that the quantum yield has increased by a factor of more than three in case of the nanostructures.

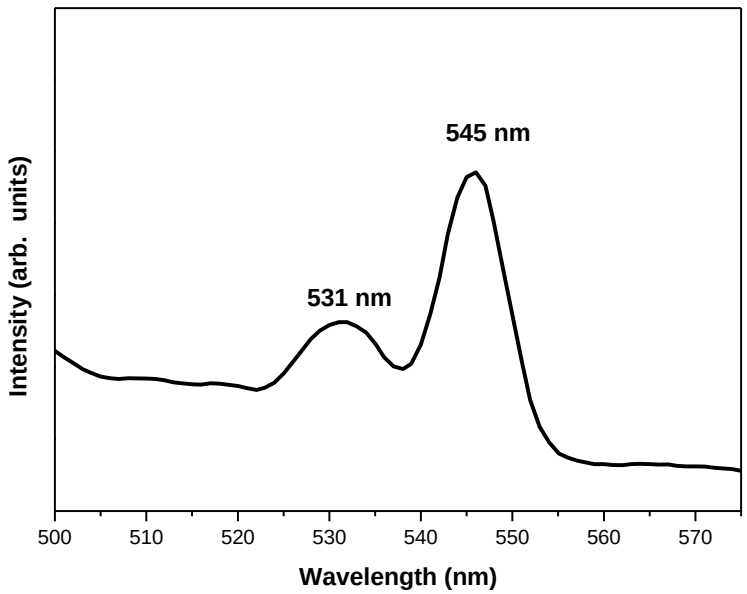

Figure 7.14: Room temperature PL spectra of CdS nanostructures deposited in the membranes having pore diameter 80 nm

7.3.3 CdS:Mn nanowires

The room temperature photoluminescence (PL) measurement results of the CdS nanowires (undoped and doped with Mn), synthesized using solvothermal technique, are shown in figure 7.15. The excited wavelength was 336 nm, and no filter was used.

Room temperature PL spectra of undoped CdS nanowires exhibit a weak and sharp emission at $\sim$ 481 nm and a broad green emission band centered at $\sim$ 517 nm.

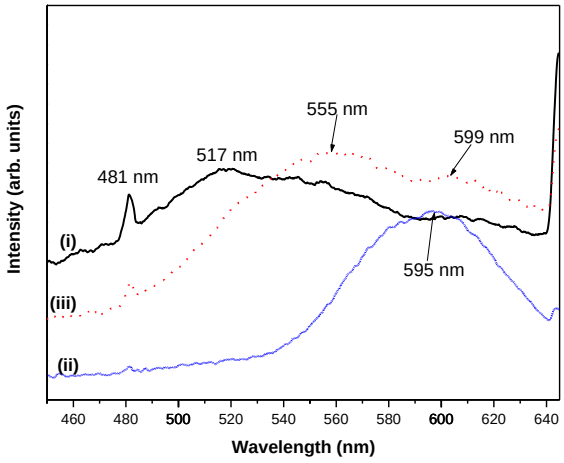

Figure 7.15: Room temperature PL spectra of (i) undoped CdS and (ii) 5 mmol (iii) 10 mmol Mn doped CdS nanowires ($\lambda_{ex} \sim 336$ nm)

The weak emission band at shorter wavelengths is attributed to the direct transition from the conduction to the valence band [162]. This indicates that the particle crystallinity is rather high. The main luminescence band is broad and is attributed to CdS trap emission. The electrons and holes, after excitation across the band edge, trickle down non-radiatively to the surface states lying in the bandgap region. Radiative de-excitation across the surface states in CdS nanowires gives rise to green fluorescence observed at around 517 nm. On addition of Mn (5 mmol) dopant, the intensity of the direct transition has been found to decrease, and, the broad band, red-shifted to 595 nm, which is similar to the Mn emission in bulk CdS:Mn due to an internal Mn^{2+} transition ($^4T_1 -^6 A_1$). On increase in the concentration of Mn (5 to 10 mmol), this broad band has red-shifted to $\sim$ 599 nm, indicating that the Mn^{2+} concentration is sufficient to influence the crystal-field splitting between $^4T_1$ and $^6A_1$ states [163]. Moreover, a broad band, centered around 555 nm, has evolved on the increase of Mn concentration, which may be attributed to the deep surface trap recombinations, unlike from defect related states [164].

7.3.4 CdS:Eu nanorods

The room temperature photoluminescence (PL) of the undoped and the Eu-doped CdS nanorods have been measured using xenon lamp as the light source at 450 nm (far above the $^5D_1$ level of Eu^{3+} ions) as the excitation wavelength and the results are shown in figures 7.16 and 7.17. The $^5D_0 -^7 F_J$ emissions are considered important for surveying the transition probabilities of sharp spectral features in rare earths.

The rare earth ions exhibit electron-electron and spin-orbit interactions within the 4f shell [179]. These f-f optical transitions are strictly forbidden, as electric-dipole transitions in case the rare earth ions occupy the inversion symmetry site in the crystal lattice. Whereas, low intensity lines in the spectra may appear if the inversion symmetry is disobeyed. However, some of these transitions like $^5D_1 -^7 F_0$, $^5D_1 -^7 F_2$ and $^5D_0 -^7 F_1$ may appear in the spectra as magnetic-dipole or as vibronic electric dipole transitions. It has also been reported by Klonkowski et al., that, the $^5D_0 -^7 F_0$ and $^5D_0 -^7 F_2$ transitions are hypersensitive to this effect [165]. The room temperature emission spectra, as shown in figure 7.17, exhibits luminescence bands at around 528 nm ($^5D_1 -^7 F_0$), 540 nm ($^5D_1 -^7 F_2$), 570 nm ($^5D_0 -^7 F_0$), 597 nm ($^5D_0 -^7 F_1$), and 613 nm ($^5D_0 -^7 F_2$).

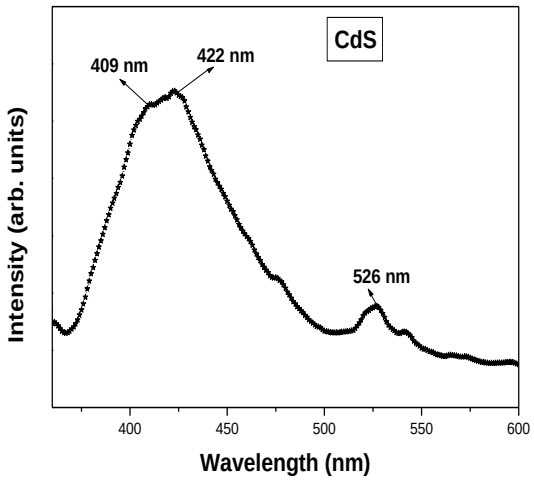

Figure 7.16: Room temperature PL spectra of undoped CdS nanorods at an excitation wavelength of 350 nm

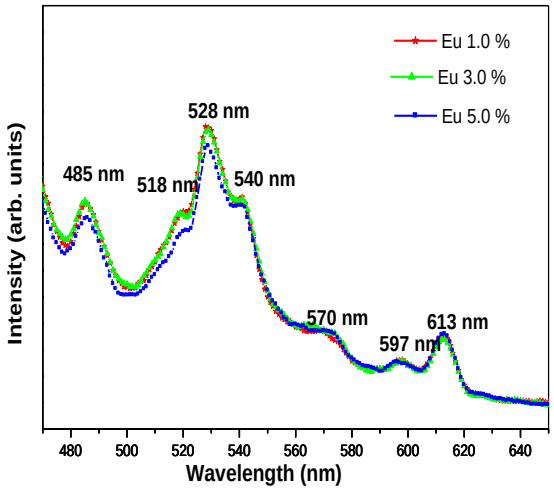

Figure 7.17: Room temperature PL spectra of CdS:Eu (1.0, 3.0 and 5.0 %) at excitation wavelength of 450 nm

7.3.5 CdS:Tb nanorods

Room temperature PL spectra of the finely dispersed CdS:Tb nanorods have been measured using a Xenon Lamp Source Spectrophotometer (Cary Varian), at an excitation wavelength of 325 nm. As shown in figure 7.18, the emission at 525 nm is due to the near band edge transition of CdS. This can also be correlated from the absorption spectra having the band gap value of nearly 518 nm. However, the emission at 543 and 573 nm can be attributed to the surface related/trap defects, due to the presence of sulfur or cadmium vacancy or interstitial. Blue colored high level transitions have been observed at 424 and 442 nm. The intensity of these emissions has increased with increase in Tb concentration as shown in figure 7.18. Moreover, a Tb ion related emission has been observed at 485 nm.

As shown in figure 7.19, an additional emission has been observed in heat treated CdS samples at 363 nm. This UV region emission has further broadened in case of Tb doping of 1.0 %, and the peak position has shifted to around 386 nm. This peak has been observed to broaden further and shift to 393 nm, on increase in Tb concentration, as shown in figures 7.20, 7.21 and 7.22. This may be due to some radiative high level transitions arising due to heat treatment. Further studies are required to probe into these changes in the emission spectra.

7.3.6 CdS/ZnS nanostructures

Room temperature PL spectra of the CdS nanorods and CdS/ZnS nanoslabs, finely dispersed in ethanol, have been shown in figure 7.23. The inset of figure 7.23, show-

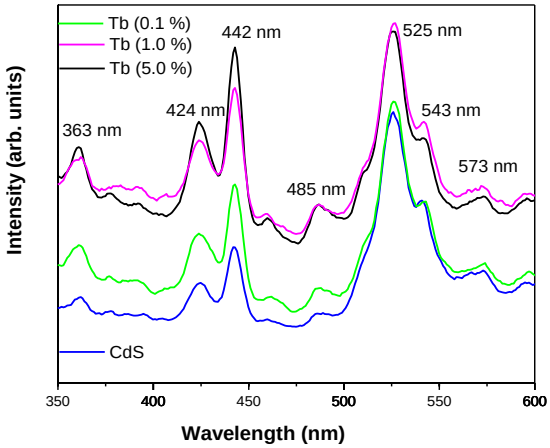

Figure 7.18: PL spectra of the undoped and Tb doped CdS nanorods at 325 nm excitation wavelength

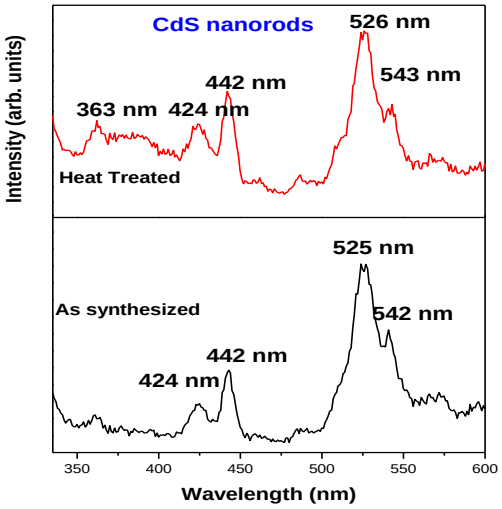

Figure 7.19: PL spectra of the undoped and Tb doped CdS nanorods at 325 nm excitation wavelength

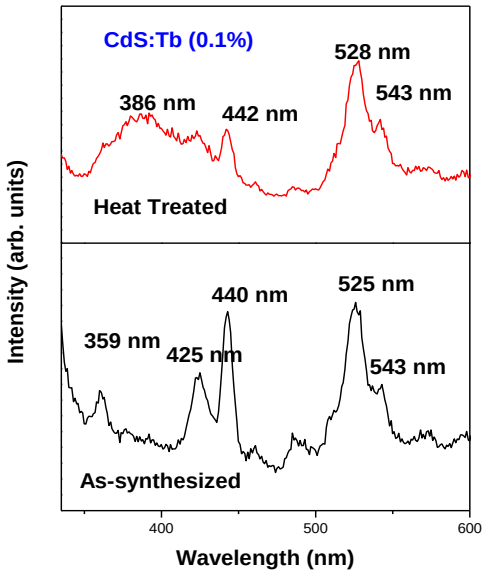

Figure 7.20: Room temperature PL spectra of CdS:Tb (0.1 %) nanorods with and without heat treatment using the excitation wavelength of 325 nm

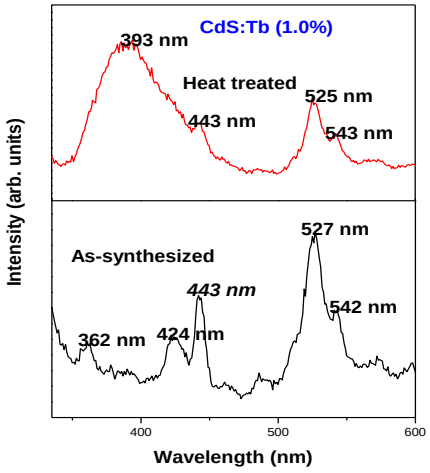

Figure 7.21: Room temperature PL spectra of CdS nanorods with and without heat treatment using the excitation wavelength of 325 nm

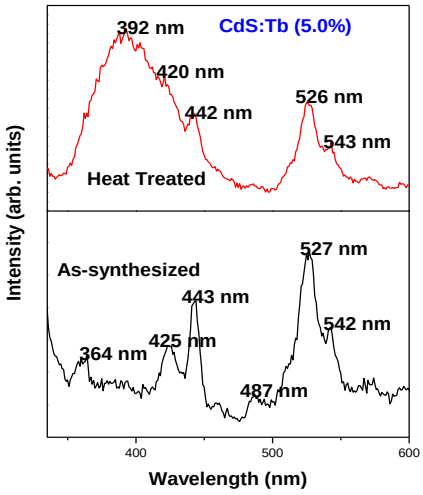

Figure 7.22: Room temperature PL spectra of CdS:Tb (5.0 %) nanorods with and without heat treatment using the excitation wavelength of 325 nm

ing the PL excitation (PLE) spectrum of CdS nanorods, shows a sharp peak centered at 403 nm. Therefore, the excitation wavelength has been chosen to be 400 nm for recording the PL spectra of CdS nanorods and CdS/ZnS nanoslabs. In case of the PL spectrum of CdS nanorods, the peak at 530 nm can be attributed to the near band edge transition, whereas the sharp peak at 544 nm may be attributed to the sulphur or cadmium related defects.

However, the PL spectra of the CdS/ZnS nanoslabs show that the luminescence intensity of CdS related peaks has increased appreciably, and the broad emission at 420 nm is due to the defect emission from the ZnS matrix rather than from an excitonic or band-to-band emission. This is because of the fact that the energy band gap of bulk ZnS at room temperature is 3.67 eV (337.9 nm), and the band gap value is known to further increase at nanoscale. These defects have been reported by many researchers as sulfur vacancies [151].The yellowish green band at $\sim$ 573 nm is most likely due to the self-activated defect centres formed by the zinc

vacancy inside the lattice [147, 176]. The wider band gap material, ZnS, confines the photogenerated electron hole pairs to the CdS core, leading to the passivation of non-radiative transitions, thus enhancing the luminescence intensity [166, 167] as shown in figure 7.23.

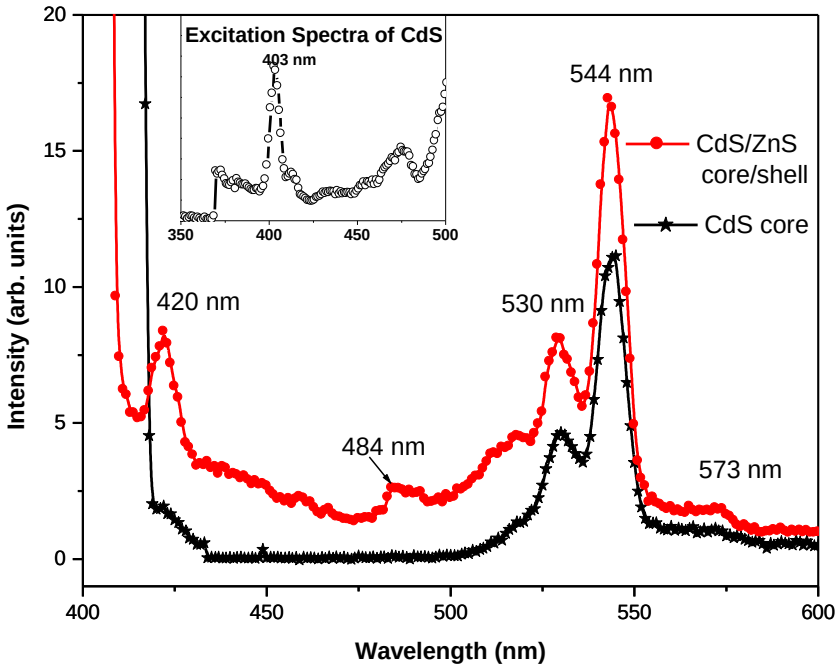

Figure 7.23: Room temperature PL spectra of CdS and CdS/ZnS nanostructures at an excitation wavelength of 400 nm; inset shows the excitation spectra of CdS nanorods

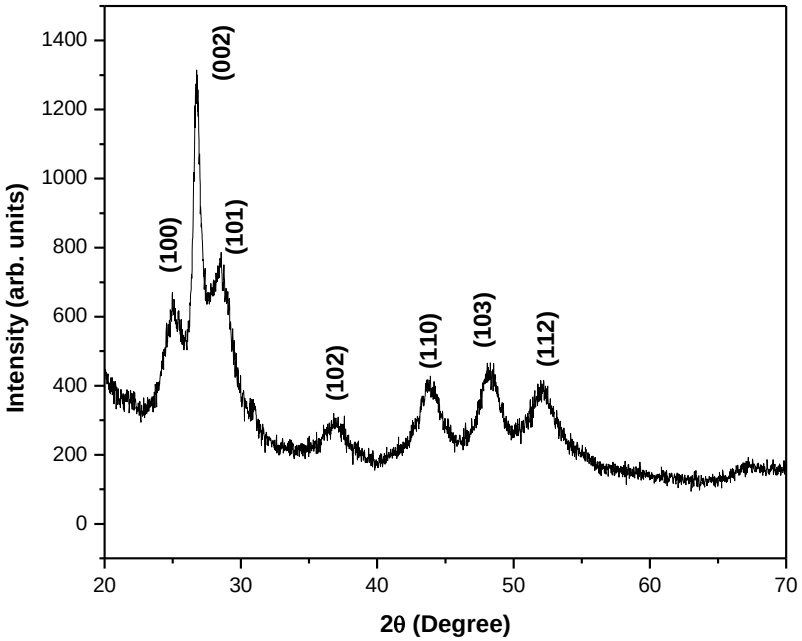

Figure 7.24: XRD pattern of CdS nanowires (sample C3) synthesized using solvothermal technique

Table 7.3: Comparative study of the PL response of various ZnS and CdS nanomaterials synthesized using different techniques

Material	**Dopant**	**Structure**	**Synthesis Technique**	**PL peak positions**
ZnS	—	Quantum dots	Chemical precipitation	420, 575 nm
ZnS	Mn	Quantum dots	Chemical precipitation	420, 582 nm
ZnS	Ni	Quantum dots	Chemical precipitation	425, 547 nm
ZnS	Cu	Quantum dots	Chemical precipitation	403.5, 425, 450, 485 nm
ZnS	Eu	Quantum dots	Chemical precipitation	425, 434, 485, 525 nm
CdS	—	Microstructures	Electrochemical template	508 nm
CdS	—	Nanorods	Electrochemical template	531, 545 nm
CdS	—	Nanowires	Solvothermal	481, 517 nm
CdS	Mn	Nanowires	Solvothermal	595 nm
CdS	—	Nanorods	Solvothermal	409, 422, 526 nm
CdS	Eu	Nanorods	Solvothermal	485, 518, 528, 540, 570, 597, 613 nm
CdS	Tb	Nanorods	Solvothermal	424, 442, 485, 525, 543, 573 nm
CdS	—	Nanorods	Solvothermal	530, 544 nm
CdS/ZnS	—	Nanoslabs	Solvothermal	420, 484, 530, 544, 573 nm

Chapter 8

Conclusions

In the entire thesis work, syntheses of undoped and doped ZnS, and CdS nanostructures have been discussed. 0-D and 1-D nanostructures have been synthesized successfully using chemical precipitation technique, electrochemical template synthesis and solvothermal technique. All these techniques of nanostructure syntheses have given reproducible results and homogeneous products. It has been observed that chemical precipitation and solvothermal techniques give much more yield as compared to the electrochemical template synthesis technique. All these three techniques are simple, cost-effective and require low temperature (room temperature to 200 ^oC).

Undoped and doped ZnS nanoparticles, synthesized by chemical precipitation technique, are in the 3-5 nm diameter range and exhibit cubic (zinc blende) crystal structure as well as are polycrystalline in nature. The doping has been carried out with the transition metal impurities, like: Mn, Cu, Co, Ni, and with rare earth impurities, like: Eu. The concept of inbuilt surfactant has been developed due to

the presence of acetate ions, in addition to the use of capping agents to control the particle size. The most stable form of zinc sulfide is the cubic structure, and, in the bulk, it transforms to wurtzite structure at 1020 ^{o}C. The bulk zinc sulfide melts at a temperature of 1650 ^{o}C. However, in case of the nanoparticles, it has been found that the transition from the cubic to hexagonal phase has occurred at 200 ^{o}C.

In order to investigate the quantum confinement effect, the band gap calculation has been carried out. The undoped ZnS nanoparticles, have the band gap value of 3.88 eV, which indicates a blue-shift as compared to the band gap of bulk ZnS (3.66 eV), indicating the quantum confinement in the ZnS nanocrystallites. The band gap values of Mn-doped ZnS nanoparticles have reduced from 3.88 eV for undoped nanoparticles to 3.71 eV for 5 % Mn doping, and to 3.34 eV for 15 % Mn doping, which is due to the Mn related levels introduced in the host lattice. The band gap energies, calculated from the differential minima of the absorbance spectra, come out to be respectively, 4.01 and 4.10 eV for $Zn_{0.995}Ni_{0.005}S$ and $Zn_{0.97}Ni_{0.03}S$ nanoparticles. On further exposing the samples to prolonged UV radiation, these band gap energies, reduce to respectively, 3.90 eV and 4.02 eV, thereby showing a red-shift. Similar quantum confinement effects have been observed in Cu-doped, Co-doped and Eu-doped ZnS nanoparticles.

CdS 1-D nanostructures have been successfully synthesized using the electrochemical template synthesis technique, with Nuclepore polycarbonate membranes having pore sizes of 800-80 nm, pore density of 10^8 cm^{-2} and thickness 11 μm, as templates. The optimized reaction parameters include: pH $\sim$ 1.77, tempera-

ture inside the electrochemical cell varying between 35^o - 45^oC, voltage applied 1.2 V, reaction time of 30 minute and continuous stirring. Various types of CdS micro/nanostructures, like: rods, tubules, cauliflower-like structures, flowers, cactus, fan-shaped structures have been synthesized. All these structures have cubic crystal phase of CdS, with little or no change in the band gap values from that of the bulk CdS (2.42 eV).

Apart from this, the syntheses of undoped and doped CdS nanostructures have been carried out by solvothermal route using ethylenediamine as the solvent and the chelating ligand. The objective was to develop a simple and low-cost synthesis route to prepare highly oriented one-dimensional (1-D) CdS nanostructures with good control over their size, shape, orientation and optical properties. On varying various reaction parameters, nanodiscs, cauliflowers and lamelle, nanowires, nanorods (free ensemble as well as standing crop on Cd foil) and nanoslabs of CdS, undoped and doped with Mn, Eu and Tb, have been synthesized. Also CdS/ZnS nanoslabs have been synthesized with CdS nanorods embedded in ZnS slabs using two step solvothermal processes. Solvothermal technique has led to the wurtzite hexagonal phase of CdS with high texturing coefficient for (002) plane. The effect of doping on the crystal structure, textural analysis, morphology and optical properties have been studied in this work. FTIR analysis has supported the presence of ethylenediamine complexes with Cd ions on the surface of the nanostructures. Band gap energies were calculated with the help of the differential minima, which varied from 2.48 eV for undoped CdS nanowires, to 2.44 eV on doping with Mn (5 mmol). For CdS, undoped and Eu-doped nanorods, the band gap values have been found to be

2.40 eV with no effect of doping.

The photoluminescent properties of the synthesized ZnS and CdS nanoforms have been studied as these are of immense scientific and industrial interests. PL spectra for the undoped ZnS nanoparticles showed two emission bands, one blue emission at 420 nm and another yellowish green band at 575 nm. The orange emission around 582 nm, attributed to the $4T^1 - 6A^1$ transition of the Mn^{2+} impurity has been found to increase in intensity with the Mn concentration upto 5 % and thereof a decrease has been observed. In case of Ni-doped ZnS nanoparticles, green emission centered at 547 nm, attributed to the d-d optical transitions of Ni^{2+} luminescent centres have been observed. The luminescence intensity of the green emission has increased with the increase in Ni concentration upto 0.5 at. % of Ni dopant, and further increase in the concentration of Ni, has decreased the luminescence intensity. However, the intensity ratio of the green to blue emission is found to increase continuously, on increasing the concentration of the dopant. Moreover, the prolonged UV-irradiation has enhanced the PL intensity of the strong green emission for all concentrations of Ni. The blue-green luminescence centered around 485 nm may have originated from the recombination of an electron from the shallow delocalized donor level (sulfur vacancy) to the t_2 level of Cu^{2+}, in ZnS:Cu nanoparticles. Remarkable enhancement of the luminescent intensity was observed on irradiating the ZnS:Cu nanoparticles with UV radiation of 255 nm for 24 hour at room temperature. In ZnS:Eu nanoparticles, emission centered at 485 nm and the green emission peak at 525 nm, attributed to Eu^{2+} related emission, due to the $4f^7 \rightarrow 4f^6 5d^1$ radiative transitions has been observed. The emission intensity has decreased with heat treatment, whereas no

shift in the peak position has been observed.

The time-resolved photoluminescence studies have been carried out for ZnS:Mn nanoparticles. With the increasing concentration of manganese, the life time reduced from 31.51 μs (for 5 at. %) to 15.86 μs (for 15 at. %). This is due to the smaller lifetimes, of the excited states of interacting pairs as compared to a single Mn^{2+} centre. With the increase in the concentration of manganese impurity, the number of such interacting pairs have increased (leading to concentration quenching), causing the decrease in excited state lifetimes. Decay constant, which explains the distribution of the trapping states introduced by the dopant within the band gap of the phosphor, has also been calculated. The trap depth has been found to be maximum (0.2683 eV) for zinc sulphide doped with 5 % of Mn, and, minimum (0.2505 eV) for 15 % Mn doping. This shows that as the concentration of manganese has increased from 5 % to 15 %, the levels introduced by Mn impurity have become shallow. The decay constant values show that the distribution of the traps within the energy band gap of phosphors is nonuniform, and, this nonuniformity has increased with the increase in the dopant concentration.

The PL spectrum of the synthesized CdS nanostructures shows a broad band centered at 508 nm (2.45 eV), attributed to the band-to-band emission. In some of the nanoforms, two green emission peaks centered around 531 nm and 545 nm have been observed. These emissions can be ascribed to the surface donor-accepter pair recombination. The origin of the defects may be associated with sulfur/cadmium vacancies or interstitials, extrinsic defects or impurities. Moreover, on doping the

dopant related emissions have also been observed, as in the case of ZnS nanoparticles.

The ratio of the number of photons emitted by the sample to the incident photons gives the quantum yield. The quantum yield of the commercially available CdS has been found to be 0.08 %, whereas it has increased to 0.28 % in case of the synthesized CdS nanostructures. This shows that the quantum yield has increased by a factor of more than three in case of the nanostructures.

Bibliography

[1] G. Cao, Nanostructures and Nanomaterials, Imperial College Press, London, 2004.

[2] http://www.nanoscience.com/education/overview.html, visited on September 2, 2009.

[3] http://www.ringsurf.com/online/2003-structures.html, visited on September 2, 2009.

[4] M. Jain, II-VI semiconductor compounds, World Scientific Publishing Co. Pvt. Ltd, 1993.

[5] http://www.ilpi.com/inorganic/structures/zincblende/index.html, visited on September 12, 2009.

[6] C. Kittel, Introduction to Solid State Physics, Wiley-India ISBN 1081-265-1045-5, 7th Edt., 1995.

[7] L. Ward, Handbook of Optical Constants of Solids II, Academic Press,1991.

[8] A. F. Wells, Structural Inorganic Chemistry, Oxford Science Publications, 5th Edt.,1984.

[9] D. R. Vij, Handbook of electroluminescent materials, Institute of Physics(Great Britain).

[10] D. R. Vij and N. Singh, Luminescence and related II-VI semiconductors, Nova Science Publishers Inc., 1998.

[11] http://www.semiconductors.co.uk/propiivi5410.htm, visited on September 20, 2009.

[12] L. Azaroff, Elements of X-ray Crystallography, McGraw-Hill Book Company,1968, Chap. 13.

[13] A. Guinier, X-ray Diffraction, Freeman, San Francisco, CA, 1963.

[14] R. E. Smallman and R. J. Bishop, Metals and Materials: Science, Processes, applications, Butterworth-Heinemann Ltd, 1995, p.146-149.

[15] G.B. Harris, Phil. Mag., **43**, 113(1952).

[16] G. Riveros, H. Gomez, A. Cortes, R. E. Marotti and E. A. Dalchiele, Appl. Phys., A **81**, 17(2005).

[17] G. Cao, Nanostructures and Nanomaterials, Imperial College Press, London, 2004, p.338-340.

[18] D. Williams and C. Carter, Transmission Electron Microscopy, Plenum Press, New York, 1996.

[19] $http://en.wikipedia.org/wiki/Energy-dispersive_X-ray_spectroscopy$, visited on August 18, 2009.

[20] R. M. Silverstein and F. X. Webster, Spectrometric identification of Organic Compunds 6th edition, John Wiley and Sons, Inc. New York, 2002.

[21] *http* : *//mmrc.caltech.edu/FTIR/FTIRintro.pdf*, visited August 18, 2009.

[22] J. I. Pankove, Optical Processes in Semiconductors, Prentice Hall, New Jersey, 1971.

[23] S. Ameen, G. B. V. S. Lakshmi and M. Husain, J. Phys. D: Appl. Phys., **42**, 105105(2009).

[24] D. Bhattacharyya, S. Chaudhari and A. K. Pal, Vacuum, **43**, 313(1992).

[25] J. R. Lakowicz, Principles of Fluoroescence Spectroscopy, 3rd edition, Springer Science + Business Media, USA, 2006, p.22-100.

[26] E. L. Ivchenko, Optical Spectroscopy of Semiconductor Nanostructures, Alpha Science International Ltd, U. K. 2004, p.203-204.

[27] H. C. Zhang, Acta Phys. Sin., **49**, 1171(2000).

[28] R. H. Bube, Phys. Rev., **80**, 655(1950).

[29] H. S. Bhatti, R. Sharma and N. K. Verma, Parmana J. Phys., **65**, 541(2005).

[30] H.Weller and A. Eychmuller, Semiconductor Nanocluters, Elesveir Science B. V. Amsterdam, **103**, 1996, p.5.

[31] http://www.britannica.com/EBchecked/topic/108784/chemical-precipitation, visited on June 17, 2009.

[32] Y. Zhao, Y. Zhang, H. Zhu, G. C. Hadjipanayis and J. Q. Xiao, J. Am. Chem. Soc., **126**, 6874(2004).

[33] S. W. Lu, B. I. Lee, Z. L. Wang, W. Tong, B. K. Wagner, W. Park and C. J. Summers, J. Lumin., **92**, 73(2001).

[34] J. T. Hu, L. S. Li, W. D. Yang, L. Manna, L. W. Wang and A. P. Alivisatos, Science, **292**, 2060(2001).

[35] A. B. Cruz, Q. Shen and T. Toyoda, Jpn. J. Appl. Phys., **44**, 4354(2005).

[36] R. N. Bhargava, J. Lumin., **72-74**, 46(1997).

[37] R. N. Bhargava, J. Lumin., **70**, 85(1996).

[38] J. Sandino, G. Gordillo and H. Lichte, EMC 2008 14th European Microscopy Congress 1-5 September 2008, Aachen, Germany Springer Berlin Heidelberg, p.363.

[39] P. Du , X. Q. Zhang, X. B. Sun, Z. G. Yao and Y. S. Wang, Chinese Phys., **15**, 1370(2006).

[40] S. H. Kang, C. K. Kumar, Z. Lee, K. H. Kim, C. Huh and E. T. Kim, Appl. Phys. Lett., **93**, 191116(2008).

[41] Y. Y. Lin, J. Wang, G. Liu, H. Wu, C. M. Wai and Y. Lin, Biosensors and Bioelectronics, **23**, 1659(2008).

[42] T. Kubo, T. Isobe, M. Sena, J. Lumin., **99**, 39(2002).

[43] F. Lacomi, Surf. Sci., **32**, 816(2003).

[44] H. Yuan, S. Xie, D. Liu, X. Yan, Z. Zhou and L. Ci, J. Cryst. Growth, **258**, 225(2003).

[45] D. Kim, K. Min, J. Lee, J. H. Park and J. H. Chun, Mater. Sci. Eng. B, **131**, 13(2006).

[46] D. Denzler, M. Olschewski and K. Sattler, J. Appl. Phys., **84**, 2841(1998).

[47] W. Chen, R. Sammynaiken, Y. Huang, J. O. Malm, R. Wallenberg, J.O. Bovin, V. Zwiller and N. A. Kotov, J. Appl. Phys., **89**, 1120(2001).

[48] M.L. Singla, M. Shafeeq M and M. Kumar, J. Lumin., **129**, 434(2009).

[49] Z. Jindal and N. K. Verma, J Mater. Sci., **43**, 6539(2008).

[50] P. Yang, M. Lu, D. Xu, D. Yuan, C. Song and G. Zhou, J. Phys. Chem. Sol., **62**, 1181(2001).

[51] W. Q. Peng, G. W. Cong, S. C. Qu and Z. G. Wang, Opt. Mater., **29**, 313(2006).

[52] P. Yang, M. Lu, D. Xu, D. Yuan, J. Chang, G. Zhou and M. Pan, Appl. Phys. A, **74**, 257(2002).

[53] P. Yang, M. Lu, D. Xu, D. Yuan, C. Song, S. Liu and X. Cheng, Opt. Mater., **24**, 497(2003).

[54] S. Sambasivam, D. P. Joseph, D. R. Reddy, B. K. Reddy and C. K. Jayasankar, Mat. Sci. Eng. B, **150**, 125(2008).

[55] V. Gavryushin, R. Baltramiejunas, G. Raciukaitis and A. Kazlauskas, Lith. J Phy., **37**, 57(1997).

[56] S. B. Qadri, E. F. Skelton, D. Hsu, A. D. Dinsmore, J. Yang, H. F. Gray and B. R. Ratna, Phys. Rev. B, **60**, 9191(1999).

[57] M. Haase, K. Riwotzki, H. Meyssamy and A. Kornowski, J. Alloys Compd., **303**, 191(2000).

[58] M. D. Barnes, A. Mehta, T. Thundat, R. N. Bhargava, V. Chhabra and B. Kulkkarni, J. Phys. Chem. B, **104**, 6099(2000).

[59] J. H. Yao, K. R. Elder, H. Guo and M. Grant, Phys. Rev. B, **47**, 14110(1993).

[60] H. C. Warad, S. C. Gosh, B. Hemtanon, C. Thanochayonont and J. Dutta, Sci. Technol. Adv. Mater., **6**, 296(2005).

[61] G. C. Trigunyat and G. K. Chadha, Phys. Status Solidi A, **4**, 9(1971).

[62] B. D. Cullity, Element of X-ray Diffraction, Addison-Wesley, New York, 1956, 2nd edn., p 99.

[63] G. Blasse and B. C. Grabmaier, Luminescent Materials, Springer- Verlag, Berlin, 1994.

[64] X. Zou, E. Ying and S. Dong, Nanotechnology, **17**, 4758(2006).

[65] R. M. Silverstein, G. Clayton Bassler and T. C. Morrill, Spectrometric Identification of Organic Compounds, John Wiley & Sons, INC., USA, 1991, 5th edn. pp. 91-164.

[66] S. K. Panda and S. Chaudhuri, Synthesis and Reactivity in Inorganic, Metal-Organic, and Nano-Metal Chemistry, **37**, 397(2007).

[67] G. Ghosh, M. K. Naskar, A. Patra, M. Chatterjee, Opt. Mater., **28**, 1047(2006).

[68] A. Dev, S. Chakarbarti, S. Kar and S. Chaudhari, J. Nanoparticle Res., **7**, 195(2005).

[69] A. Datta, S. Kar and S. Chaudhuri, J. Nanosci. Nanotechno., **8**, 2049(2008).

[70] Z.L. Wang, Adv. Mater., **12**, 1295(2000).

[71] J. Hu, T.W. Odom. and C.M. Lieber, Acc.Chem.Res., **32**, 435(1999).

[72] B. Yang, P. Feng, A. Kumar, R. S. Katiyar and M. Achermann, J. Phys. D: Appl. Phys., **42**, 195402(2009).

[73] J. C. Hulteen and C. R. Martin, J Mater. Chem, **7**, 1075(1997).

[74] A. Jagminas, J. Kuzmarskyte, L. Malferrari and M. Cuffiani, Mater. Lett., **61**, 2896(2007).

[75] C. R. Martin, Sci., **266**, 1961(1991).

[76] C. Shen, X. Zhang and H Li, Mat. Sci. Eng. A, **303**, 19(2001).

[77] G. X. Wang, M. S. Park, H. K. Liu, D. Wexler and J. Chen, Appl. Phys. Lett., **88**, 193115(2006).

[78] Y. Cui, Q. Q. Wei, H. K. Park and C. M. Lieber, Science, **293**, 1289(2001).

[79] D. M. Wang, J. Song, Y. Mu and C. M. Lieber, Nano Lett., **3**, 1255(2003).

[80] S. P. Mondal, K. Das, A. Dhar and S. K. Ray, Nanotechnology, **18**, 095606(2007).

[81] T. Peng, H. Yang, K. Dai, X. Pu and K. Hirao, Chem. Phys. Lett., **379**, 432(2003).

[82] W. Shenton, T. Douglas, M. Young, G. Stubbs and S. Mann, Adv. Mater., **11**, 253(1999).

[83] Y. Ono, Y. Kanekiyo, K. Inoue, J. Hojo, M. Nango and S. Shinkai, Chem. Lett., **28**, 475(1999).

[84] M. Harada and M. Adachi, Adv. Mater., **12**, 839(2000).

[85] B.C. Satishkumar, A. Govindaraj, E.M. Vogl, L. Basumallick and C.N.B. Rao, J. Mater. Res., **12**, 604(1997).

[86] C.R. Martin, Chem. Mater., **8**, 1739(1998).

[87] C.J. Brumlik and C.R. Martin, J. Am. Chem. Soc., **113**, 3174(1991).

[88] J. Bao, C. Tie, Z. Xu, Q. Zhou, D. Shen and Q. Ma, Adv. Mater., **13**, 1631(2001).

[89] M. Zhang, Y. Bando and K. Wada, J. Mater. Sci. Lett., **20**, 167(2001).

[90] L.T. Chadderton and Y. Chen, J. Cryst. Growth, **240**, 164(2002).

[91] D. Routkevich, T. Bigioni, M. Moskovits and J. Ming Xu, J. Phys. Chem., **100**, 14037(1996).

[92] D. Xu, Y. Xu, D. Chen, G. Guo, L. Gui and Y. Tang, Chem. Phys. Lett., **325**, 340(2000).

[93] D. Xu, Y. Xu, D. Chen, G. Guo, L. Gui and Y. Tang, Adv. Mater., **12**, (2000) 520.

[94] Y. Li, D. Xu, Q. Zhang, D. Chen, F. Huang, Y. Xu, G. Duo and Z. Gu, Chem. Mater., **11**, 3433(1999).

[95] H. Zhang, X. Ma, J. Xu, J. Niu, J. Sha and D. Yang, J. Cryst. Growth, **246**, 108(2002).

[96] K. Mazeika, J. Reklaitis, A. Jagminas and D. Baltrunas, Hyperfine. Interact., **189**, 137(2009).

[97] R. Spohr, Ion Tracks and Microtechnology, Vieweg, Braunschweig, 1990.

[98] J. Vetter and R. Spohr, Nucl. Instrum. Methods in Physics Research B-Beam Interactions with Materials and Atoms, **79**, 691(1993).

[99] T.M. Whitney, J.S. Jiang, P.C. Searson and C.L. Chien, Science, **261**, 1316(1993).

[100] S. K. Chakarvarti, V. Kumar and S. Kumar, J. Mater. Sci. Lett., **40**, 503(2005).

[101] R. Kaur, N. K. Verma and S. Kumar, J. Mater. Sci., **41**, 3723(2006).

[102] W. S. Sheldrick and M.Wachhold, Angew. Chem. Int. Ed. Engl., **36**, 206(1997).

[103] S. M. Liu, H. Q. Guo, Z. H. Zhang, F. Q. Liu and Z. G. Wang, Chin. Phys. Lett., **17**, 609(2000).

[104] S. H. Yu, J. Yang, Z. H. Han, Y. Zhou, R. Y. Yang, Y. Xie, Y. T. Qian and Y. H. Zhang, J. Mater. Chem., **9**, 1283(1999).

[105] Perkin-Elmer Corporation. PHI 5300 Instrument Manual, Perkin-Elmer, 1979.

[106] D. Xu, D. Chen, Y. Xu, X. Shi, G. Guo, L. Gui and Y. Tang, Pure Appl. Chem., **72**, 127(2000).

[107] M. H. Huang, A. Choudrey and P. D. Yang, Chem. Commun., 1063(2000).

[108] S. Bhattacharrya, S. K. Saha and D. Chakravorty, Appl. Phys. Lett., **77**, 3770(2000).

[109] T. Seeger, P. Kohler-redlich and M. Ruhle, Adv. Mater., **12**, 279(2000).

[110] Y. Sun, B. Gates, B. Mayers and Y. Xia, Nano Lett., **2**, 165(2002).

[111] A. Rabeneau, Angew. Chem., Int. Ed. Engl., **24**, 1026(1985).

[112] R. I. Walton, Chem. Soc. Rev., **31**, 230(2002).

[113] S. H. Yu, Y. S. Wu, J. Yang, Z. H. Han, Y. Xie, Y. T. Qian and X. M. Liu, Chem. Mater., **10**, 2309(1998).

[114] K. Byrappa and M. Yoshimura, Handbook of Hydrothermal Technology, Noyes Publishers, Park Ridge, NJ, 2001.

[115] L. Manna, D. J. Milliron, A. Meisel, E. C. Scher and A. P. Alivisatos, Nature Mater., **2**, 382(2003).

[116] W. T. Yao, S. H. Yu, S. J. Liu, J. P. Chen, X. M. Liu and F. Q. Li, J. Phys. Chem. B, **110**, 11704(2006).

[117] B. Cheng and Z. Wang, Adv. Funct. Mater., **15**, 1883(2005).

[118] R. Reisfeld, M. Gaft, T. Saridarov, G. Panczer and M. Zelner, Mater. Lett., **45**, 154(2000).

[119] B. Julian, J. Planelles, E. Cordoncillo, P. Escribano, P. Aschehoug, C. Sanchez, B. Vianab and F. Pelleb ,J. Mater. Chem., **16**, 4612(2006).

[120] T. Hayakawa, S. T. Selvan and M. Nogami, J. Sol-Gel Sci.Technol., **19**, 779(2000).

[121] T. Hayakawa, S. T. Selvan and M. Nogami, J. Lumin., **87-89**, 532(2000).

[122] A. Datta, S. K. Panda and S. Chaudhari, J. Phys. Chem. C, **111**, 17260(2007).

[123] S. Santra, H. Yang, P. H. Holloway, J. T. Stanley and R. A. Mericle, J. Am. Chem. Soc., **127**, 1656(2005).

[124] J. Y. Kim and F. E. Osterloh, J. Am. Chem. Soc., **127**, 10152(2005).

[125] B. I. Ipe and C. M. Niemeyer, Angew. Chem., **45**, 504(2006).

[126] Y. Yang, O. Chen, A. Angerhofer and Y. C. Cao, J. Am. Chem. Soc., **128**, 12428(2006).

[127] L. Ouyang, K. N. Maher, C. L. Yu, J. McCarty and H. Park, J. Am. Chem. Soc., **129**, 133(2007).

[128] H. Yang and P. H. Holloway, Adv. Funct. Mater., **14**, 152(2004).

[129] R. A. Caruso and M. Antonietti, Chem. Mater., **13**, 3272(2001).

[130] K. Palaniappan, C. Xue, G. Arumugam, S. A. Hackney and J. Liu, Chem. Mater., **18**, 1275(2006).

[131] R. Davies, G. A. Schurr, P. Meenan, R. D. Nelson, H. E. Bergna, C. A. S. Brevett and R. H. Goldbaum, Adv. Mater., **10**, 1264(1998).

[132] L. M. Liz-Marzan, M. Giersig and P. Mulvaney, Langmuir, **12**, 4329(1996).

[133] S. Kar, S. Santra and H. Heinrich, J. Phys. Chem. C, **112**, 4036(2008).

[134] A. Datta, S. Kar, J. Ghatak and S. Chaudhari, J. Nanosci. Nanotechnol., **7**, 677(2007).

[135] J. S. Jang, S. H. Choi, H. Park, W. Choi and J. S. Lee, J. Nanosci. Nanotechnol., **6**, 3642(2006).

[136] Z. X. Deng, L. Li and Y. D. Li, Inorg Chem, **42**, 2331(2003).

[137] Y. Liu, H. Y. Qiu, Y. Xu, D. Wu, M. J. Li, J. X. Jiang and G. Q. Lai, J. Nanopart. Res., **9**, 745(2007).

[138] H. B. Liu, Y. L. Lia, H. Y. Luo, H. J. Fang, H. M. Li, S. Q. Xiao, Z. Q. Shi, S. X. Xiao and D. B. Zhu, Eur. Phys. J. D, **24**, 405(2003).

[139] J. Yang, J. H. Zeng, S. H. Yu, L. Yang, G. Zhou and Y. Qian, Chem. Mater., **12**, 3259(2000).

[140] P. V. Radovanovic, K. G. Stamplecoskie and B. G. Pautler, J. Am. Chem. Soc., **129**, 10980(2007).

[141] D.J. Milliron, S. M. Hughes, Y. Cui, L. Manna, J. Li, L. -W. Wang and A. P. Alivisatos, Nature, **430**, 190(2004).

[142] A. Datta, S. Kar and S. Chaudhuri, J. Nanosci. Nanotechno., **8**, 2049(2008).

[143] B. Tripathi, F. Singh, D. K. Avasthi, D. Das, Y. K. Vijay, Physica B, **400**, 70(2007).

[144] A. Datta, S. K. Panda and S. Chaudhari, J. Phys. Chem. C, **111**, 17260(2007).

[145] A. A. Bol and A. Meijerink, Phys. Rev. B, **58**, R15997(1998).

[146] S. Kar and S. Chaudhari, J. Phys. Chem. B, **109**, 3298(2005).

[147] C. Falcony, M. Garcia, A. Ortiz, J. C. Zlonso, J Appl. Phys., **72**. 1525(1992).

[148] H. Samelson, A. Lempicki, Phys. Rev., **125**, 901(1962).

[149] J. M. Noras and J. W. Allen, J. Phys. C: Solid St. Phys., **13**, 351(1980).

[150] J. M. Tsay, S. Doose, F. Pinaud and S. Weiss, J. Phys. Chem. B, **109**, 1669(2005).

[151] J. W. Lee, K. Cho, H. Kim, J. H. Kim, B. Park, T. Noh, S. H. Kim and S. Kim, Jap. J. Appl. Phys., **44**, 7694(2005).

[152] A. A. Bol, J. Ferwerda, J. A. Bergwerf and A. Meijerink, J. Lumin., **99**, 325(2002).

[153] A. B. Cruz, Q. Shen and T. Toyoda, Thin Solid Films, **499**, 104(2006).

[154] S. Lee, D. Song, D. Kim, J. Lee, S. Kim, I. Y. Park and Y. D. Choi, Mater. Lett., **58**, 342(2004).

[155] D. D. Papakonstantinou, J. Huang and P. Lianos, J. Mater. Sci. Lett., **17**, 1571(1998).

[156] W. Chen, J. O. Malm, V. Zwiller, Y. Huang, S. Liu, R. Wallenberg, J. O. Bovin and L. Samuelson, Phys. Rev. B, **61**, 11021(2000).

[157] B. Ullrich, D. M. Bagnall, H. Sakai and Y. Segawa, Solid State Commin., **109**, 757(1999).

[158] R. L. Morales, O. Z. Angel and G. T. Delgado, Appl. Sur. Sci., **562**, 175(2001).

[159] Y. Wang, G. Meng, L. Zhang, C. Liang and J. Zhang, Chem. Mater., **14**, 1773(2002).

[160] R. Maity and K. K. Chatopadhyay, J. Nanopart. Res., **8**, 125(2006).

[161] Y. Wang and N. Herron, J. Phys. Chem., **92**, 4988(1988).

[162] L. Levy, N. Feltin, D. Ingert, and M. P. Pileni, J. Phys. Chem. B, **101**, 9153(1997).

[163] D. S. Kim, Y. J. Cho, J. P. J. Yoon, Y. Jo and M.-H. Jung, J. Phys. Chem. C, **111**, 10861(2007).

[164] S. Sapra , A. Prakash , A. Ghanghrekar, N. Perasamy and D. D. Sarma, J. Phys. Chem. B, **109**, 1663(2005).

[165] A. M. Klonkowski, I. Szalkowska, Mater. Sci.-Poland, **23**, 253(2005).

[166] R. G. Xie, U. Kolb, J. X. Li, T. Basche and A. Mews, J. Am. Chem. Soc., **127**, 7480(2005).

[167] B. O. Dabbousi, J. Rodriguez-Viejo, F. V. Mikulec, J. R. Heine, H. Mattoussi, R. Ober, K. F. Jensen and M. G. Bawendi, J. Phys. Chem. B, **101**, 9463(1997).

[168] A. B. Cruz, Q. Shen and T. Toyoda, Mater. Sci. Eng. C, **25**, 761(2005).

[169] S. P. Mondal, A. Dhar and S. K. Ray, Mater. Sci. Semiconduct. Process., **10**, 185(2007).

[170] D. Xu, Y. Xu, D. Chen, G. Guo, L. Gui and Y. Tang, Chem. Phys. Lett., **325**, 340(2000).

[171] D. Xu, Y. Xu, D. Chen, G. Guo, L. Gui and Y. Tang, Adv. Mater., **12**, 520(2000).

[172] R. Kaur, N. K. Verma and S. K. Chakarvarti, J Mater. Sci., **42**, 3588(2007).

[173] R. Kaur, N. K. Verma and S. K. Chakarvarti, J Mater. Sci., **42**, 5629(2007).

[174] Wenbin Yang, Zhi Wu, Zhongyuan Lu, Xuping Yang, Lixian Song, Microelect. Eng., **83**, 1971(2006).

[175] Z. Jindal and N. K. Verma, J Optoelectron. Adv. Mater., **10**, 3283(2008).

[176] Z. Jindal, N. K. Verma, J. Mater. Sci., **43**, 6539(2008).

[177] Y. Zhang, N. Wang, S. Gao, R. He, S. Miao, J. Liu, J. Zhu and X. Zhang, Chem. Mater., **14**, 3564(2002).

[178] T. Gao, G. W. Meng and T. H. Wang, Chin. Phys. Lett., **21**, 959(2004).

[179] R. Reisfeld, M. Gaft, T. Saridarov, G. Panczer and M. Zelner, Mater. Lett., **45**, 154(2000).

Index